UNIVERSITY COLLEGE LONDON

Intrinsic Josephson Microwave Phase Shifter

by

Timothy A. Wootton

A thesis submitted for the
degree of Doctor of Philosophy

in the
UCL Faculty of Engineering Sciences
Department of Electronic and Electrical Engineering

March 2019

Declaration of Authorship

I, Timothy Arthur Wootton, confirm that the work presented in this thesis is my own. Where information has been derived from other sources, I confirm that this has been indicated in the thesis.

Signed: ____________________________________

Date: ____________________________________

UNIVERSITY COLLEGE LONDON

Abstract

UCL Faculty of Engineering Sciences
Department of Electronic and Electrical Engineering

Doctor of Philosophy

by Timothy A. Wootton

Phase shifters are a vital part of communication systems, and research into superconducting electronic devices has highlighted the possible application of Josephson junctions in this field of research. Intrinsic Josephson junctions (IJJs) are created by the high-density atomic-scale superconducting/insulator layering found within high temperature superconductors, such as $Tl_2Ba_2CaCu_2O_8$. This means a large number of series junctions are able to be created in relatively small dimensions in comparison to extrinsic devices limited in size by fabrication techniques. By designing IJJ tracks with large numbers of junctions in series, the phase shift from each individual junction sums to produce significant measurable phase tunability.

I have studied the characteristics of IJJ tracks fabricated in $Tl_2Ba_2CaCu_2O_8$ to investigate the their use as microwave phase shifters. This involved determining the optimum track dimensions to ensure true Josephson behaviour of the IJJs by measuring the current-voltage characteristics at 4.2K. I have derived the equations governing the phase bias relationship, used these to simulate the expected junction characteristics based on the track parameters. These were then compared with the measured results and discussed in the context of other research in the field.

Based on the phase tunability measured in the $Tl_2Ba_2CaCu_2O_8$ tracks, I then proceed to investigate the possible use of the coplanar IJJ transmission line as a parametric amplifier. The results presented highlight a small region of gain coupled to a geometric resonance, however this is not due to any parametric effect. Further research in this area is required to excite parametric amplification from these devices.

Acknowledgements

My greatest thanks goes to my supervisor, Professor Paul Warburton at the London Centre for Nanotechnology (LCN). His support, assistance and patience throughout my time at UCL has been invaluable and generous. Without his guidance, experience and direction, I would not have managed to progress as far with my work.

I extend my sincere gratitude to Dr Susannah Speller at the University of Oxford, who provided the fundamental material needed for my research. I also thank Dr Sajid Saleem, who provided the initial advice and training when I started my research as part of the Nanoelectronics group at the LCN.

I would also like to thank all those at the LCN who have supported and assisted me in my time there during my research; Dr Maddison Coke, Dr Nicolas Constantino, Dr Chris Nash, Dr Ivan Isakov, Dr Arnaud Blois, Dr Jon Burnett, Dr Marion Sourribes, Mr. Oscar Kennedy, Dr James Sagar, Dr Jon Fenton, Mr. Steve Etienne, Ms. Vijay Krishnan and Dr Ed Romans. Thank you for your assistance and patience with me through our time together at the LCN, and for making the labs a fun place to work.

Special thanks goes to Ms. Leah Bramwell for her generosity, kindness and encouragement during my writeup.

I would finally like to thank my parents, Deborah and Colin, my grandparents, Elizabeth and Arthur, and my partner, Olivia, for always being there to help revel in my triumphs and pick me up when things went awry. I will always remember your continued love, support and faith in me throughout my time at UCL during my studies.

Contents

List of Figures

Abbreviations

BSCCO	**B**ismuth **S**trontium **C**alcium **C**opper **O**xide
CMOS	**C**omplementary **M**etal **O**xide **S**emiconductor
CMPS	**C**oupled **M**icrostrip **P**hase **S**hifter
CPW	**C**o**P**lanar **W**aveguide
DAC	**D**igital to **A**nalogue **C**onverter
FET	**F**ield **E**ffect **T**ransistor
FIB	**F**ocussed **I**on **B**eam
FWM	**F**our **W**ave **M**ixing
HDP	**H**elium **D**ip **P**robe
HTS	**H**igh **T**emperature **S**uperconductor
IJJ	**I**ntrinsic **J**osephson **J**unction
LAO	**L**anthanum **A**luminium **O**xide
LTS	**L**ow **T**emperature **S**uperconductor
MESFET	**ME**tal-**S**emiconductor **F**ield **E**ffect **T**ransistor
MMIC	**M**onolithic **M**icrowave **I**ntegrated **C**ircuit
SCS	**S**uperconductor **C**onductor **S**uperconductor
SEM	**S**canning **E**lectron **M**icroscopy
SIS	**S**uperconductor **I**nsulator **S**uperconductor
SNS	**S**uperconductor **N**ormal **S**uperconductor
SQUID	**S**uperconducting **QU**antum **I**nterference **D**evice
STO	**S**trontium **T**itanium **O**xide

TBCCO	**T**hallium **B**arium **C**alcium **C**opper **O**xide
TWPA	**T**ravelling **W**ave **P**arametric **A**mplifier
VNA	**V**ector **N**etwork **A**nalyser
YBCO	**Y**ttrium **B**arium **C**opper **O**xide

Physical Constants

k_B = Boltzmann's Constant = $1.38 \times 10^{-23}\mathrm{J.K}^{-1}$

Φ_0 = Magnetic Flux Quantum = $h/2e = 2.068 \times 10^{-15}\mathrm{Wb}$

h = Planck Constant = $6.626 \times 10^{-34}\mathrm{J.s}$

$\hbar$ = Reduced Planck Constant = $h/2\pi = 1.055 \times 10^{-34} m^2.kg/s$

e = Electronic Charge = $1.602 \times 10^{-19} C$

Symbols

T_c = Critical Temperature

ξ = Coherence Length

$\Delta(T)$ = Temperature Dependent Energy Gap

H_c = Critical Field Strength

J_c = Critical Current Density

λ = Penetration Depth

κ = Ginzberg Landau Parameter

Ψ = Superconducting Wavefunction

I_c = Critical Current

I_{sw} = Switching Current

θ = Supeconducting Phase

t = Time

ϕ = Signal Phase Shift

f_J = Josephson Frequency

I = Direct Current

V = DC Voltage

L_J = Josephson Inductance

C = Capacitance

R = Resistance

τ = Dimensionless Time Variable

ω_P = Plasma Frequency

Q = Quality Factor

β_C = Stewart McCumber Parameter

m = Mass

F = Force

E_J = Josephson Energy

ΔV = Potential Barrier

I_r = Retrapping Current

V_g = Energy Gap Voltage

Q = Charge

R_N = Normal Resistance

υ_p = Phase Velocity

$\Delta\phi$ = Wavenumber/Phase Change per Unit Length

$\Delta\phi_J$ = Phase Change per Junction

f = Frequency

N = Number of Units/Cells/Junctions

l = Track Length (Page 20)

b = Thin Film Thickness (Page 20)

s = Insulating Layer Thickness (Page 20)

t = Superconducting Layer Thickness (Page 20)

G_S = Signal Gain

$\Delta\theta$ = Pump Signal Phase Shift

Chapter 1

Introduction

Since the discovery of superconductivity in 1911, research in the field has greatly expanded, spanning a vast array of fields and applications. Recent focus on the use of superconductors in communications has driven research on developing components for microwave systems to control and manipulate signals with very low dissipation and transmission losses. Phased array antennas are an example of a communications device that relies heavily on phase shifters to control the direction of transmission, and amplification of incoming signals from multiple antennas.

Two superconductors connected by a weak link, also known as a Josephson junction, were predicted by Brian Josephson in 1962 [1], and have since been heavily researched and widely used in superconducting devices from voltage standards [2] to superconducting quantum interference devices (SQUIDs) [3]. Josephson junctions can behave similarly to inductors, and have the ability to act as bias tunable phase shifters. Intrinsic Josephson junctions, discovered in 1992 by Kleiner *et al.* [4], formed by the high density atomic layering within high-temperature superconductors have the potential to produce large amounts of phase shift by coupling large numbers of junctions together in a superconducting Josephson transmission line. More recently, research has been directed at developing Josephson parametric amplifiers which can be used for sensitive quantum computational systems. These devices are based on the non-linear kinetic inductance of the superconductor and the phase shift that it produces.

My research has investigated the use of the high-temperature superconductor thallium barium calcium copper oxide (TBCCO) as a superconducting phase shifter. The following chapters outline the background theory underpinning the work presented, an introduction into the existing research in the field of phase shifting devices, a description of the techniques used for fabrication and low temperature measurement of superconducting Josephson phase shifters, and finally discussion of the measurements and results. The tunability of the signal phase with current has been simulated and measured. The use of such a phase shifter as a parametric amplifier was explored, however further work is required to realise such a device.

Chapter 2

Background Theory

This section will provide the foundation of knowledge on which the work presented in this thesis is based. The general field of superconductivity will be briefly introduced, followed by a more in depth discussion of Josephson junctions and intrinsic Josephson junctions. For further reading on the subjects presented in this chapter, refer to Tinkham [5], Poole [6], Waldram [7] and Sheahen [8].

2.1 Superconductivity

There are two main properties that separate superconductors from other normal conductors; they exhibit zero resistance below a critical temperature, and they expel a magnetic field from within the superconductor below a critical field strength.

Above a critical temperature, T_c, a superconductor displays an ohmic resistance in what is deemed the 'normal state'. As the temperature of the superconducting material is reduced, a transition occurs at the critical temperature and the resistance falls to zero; the material becomes superconducting (Figure 2.1). This phenomenon was first observed by Heike Kamerlingh Onnes in 1911 using mercury immersed in liquid helium [9], for which he received the 1913 Nobel Prize in Physics.

The first materials that were discovered to superconduct were mercury, lead and tin. Since then, there have been a number of other materials, mostly metallic elements, that have been found to superconduct with critical temperatures below 25 Kelvin, and these materials are grouped together under the title of Low Temperature Superconductors (LTS).

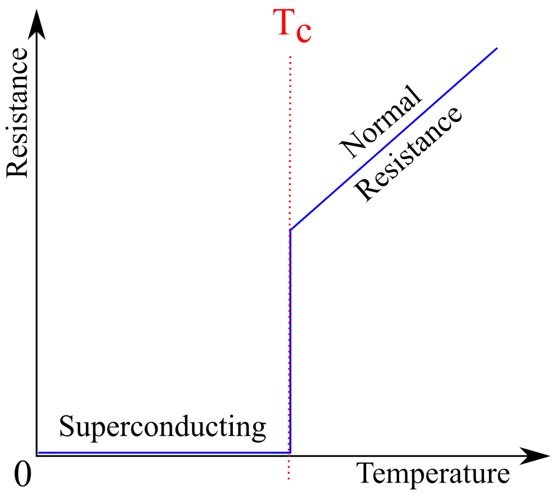

FIGURE 2.1: Ideal superconductive transition from normal ohmic behaviour above T_c to superconducting behaviour with zero resistance below

Low temperature superconductivity occurs due to the electron-lattice interactions within the material. By reducing the temperature, thermal lattice vibrations can be reduced to such a low level that electron transport through a material causes a localised potential, indirectly coupling them to other electrons with equal and opposite spin in the vicinity of the potential. This coupling results in electron pairs called Cooper Pairs, named after Leon Cooper who won the Nobel Prize for Physics in 1972, along with John Bardeen and John Schrieffer for developing the Bardeen, Cooper, Schrieffer (BCS) theory of superconductivity in 1957 [10]. These Cooper pairs all occupy the same ground state due to their net zero momentum and bosonic behaviour, and can be described by a single superconducting wavefunction.

In 1953, Brian Pippard postulated that the superconducting wavefunction has a characteristic length scale, the coherence length ξ [11]. A change in the wavefunction of one carrier within the superconductor would affect another within the distance ξ. This coherence length is analogous to the mean free path in normal metals, and is related to the critical temperature of the superconductor, as shown in Equation 2.1 below.

$$\xi = \frac{a\hbar\upsilon_f}{k_B T_c} \tag{2.1}$$

where a is a fitting constant = 0.18 [12], k_B is Boltzmann's constant = 1.38 x 10^{-23} J.K^{-1}, and υ_f is the Fermi velocity, where the kinetic energy of the cooper pairs is equal to the Fermi energy. Cooper later built on this idea and stated that the interaction distance between the electrons forming Cooper pairs within the material was also of the order of the coherence length [13].

The BCS theory [12] states that there is an energy gap between the ground state of the superconductor and the excited states. This energy gap, Δ(T) is related to the density of states at the fermi level, N(0), multiplied by the interaction potential, V, as shown by Equation 2.2. For most superconductors, N(0)V $<$ 0.3, in what is described as the weak-coupling approximation where N(0)V « 1 [5]. By comparing Equations 2.2 and 2.3 [12] at T=0, the relationship between the gap and T_c is given by Equation 2.4 [12].

$$\Delta \approx 2\hbar\omega_c e^{-1/N(0)V} \tag{2.2}$$

$$k_B T_c = 1.14\hbar\omega_c e^{-1/N(0)V} \tag{2.3}$$

$$2\Delta(0)/k_B T_c = 3.50 \tag{2.4}$$

As the temperature of the superconductor is increased from 0 K, Cooper pairs are broken and the electrons are excited across the energy gap, forming quasiparticle excitations (electron and hole-like particles). As the temperature increases towards T_c, the gap reduces to zero, and the number of Cooper pairs also reduces, reaching zero at T $= T_c$, whereby the superconductivity is lost and the material returns to the resistive normal state.

The expulsion of a magnetic field from within a superconductor is the defining difference from a perfect conductor. Perfect conductors display zero resistance, but superconductors also act as a perfect diamagnet; they oppose and expel any external field in which they are placed, up to a critical field strength, H_c. The exponential decay of the magnetic field within the superconductor occurs within the penetration depth from the surface, λ. This response was observed by Walther Meissner and Robert Ochsenfeld in 1933, and is named the Meissner effect [14].

Superconductors can react in two different ways once H_c is reached. The way they behave above the critical field determines whether they are a Type 1 or a Type 2 superconductor based on the Ginzburg-Landau parameter, κ.

$$\kappa = \frac{\lambda}{\xi} \tag{2.5}$$

The coherence length ξ is larger than the penetration depth λ for Type 1 superconductors; $\kappa < 1$. The coherence length ξ is less than the penetration depth λ for Type 2 superconductors; $\kappa > 1$.

Once the external field exceeds H_c, Type 1 superconductors experience an immediate breakdown of superconductivity, returning to the normal state. Type 2 superconductors however see a gradual loss of superconductivity between the lower critical field H_{c1} and the upper critical field H_{c2}. Once the field is higher than H_{c1}, flux vortices penetrate the material, each vortex containing a single flux quantum $\Phi_0 = h/2e =$ 2.068 x 10^{-15}Wb. This continues up to H_{c2}, where the vortices fill the material, and superconductivity is destroyed.

Along with the critical temperature T_c and critical field strength H_c, biasing with a dc current exceeding the critical current density, J_c, breaks the bonds between the Cooper pairs, causing the material to return to the normal state.

High temperature superconductors (HTS) have been discovered more recently, and unlike LTS, have values of T_c up to as high as 133 Kelvin [15]. There is not yet a widely agreed upon theory of the mechanism behind high temperature superconductivity, but it appears to be related to the symmetry of the pairing wave function and order parameter [16]. The largest collection of HTS materials fall under the family of cuprates, such as yttrium barium copper oxide (YBCO), bismuth strontium calcium copper oxide (BSCCO) and thallium barium calcium copper oxide (TBCCO). These materials consist of naturally formed alternating layers of insulator and superconducting CuO_2.

2.2 Josephson effect

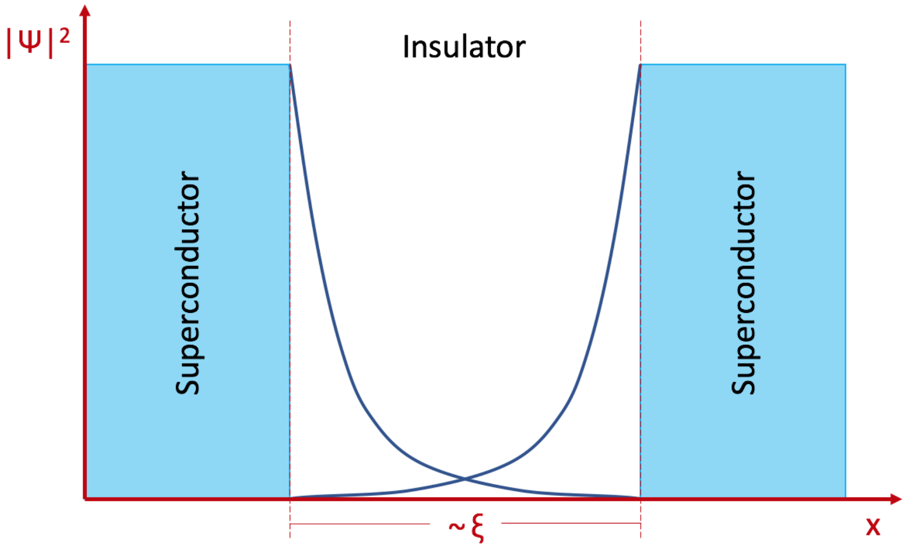

FIGURE 2.2: Diagram illustrating the Josephson effect. $|\Psi|^2$ represents the amplitude of the superconducting wavefunction, and ξ is the coherence length of the superconducting material.

In 1962, Brian Josephson calculated that Cooper pairs were able to cross an insulating barrier from one superconductor to another due to quantum tunnelling [1]. This effect was then experimentally confirmed the following year by two scientists at Bell Labs, Philip Anderson and John Rowell [17].

When two superconductors are separated by a distance greater than the coherence length ξ, their macroscopic superconducting wavefunctions remain independent of each other, and there is no tunnelling of Cooper pairs from one to the other. Once the two superconductors are brought within a coherence length of each other, there is superposition of the two wavefunctions and a weak link is formed (Figure 2.2). This superposition of the wavefunctions corresponds to the tunnelling of Cooper pairs across the barrier, whether insulator, air or normal metal. This is known as the DC Josephson effect, and the current in the system is given by Equation 2.6

$$I = I_c sin(\theta) \tag{2.6}$$

where I_c is the critical current of the junction and θ is the difference in phase of the wavefunction of superconductor 1 and the wavefunction of superconductor 2. The critical current of a junction is the largest current the superconductor can transport without energy being dissipated. If the current through the junction remains below I_c, there is a stable solution to Equation 2.6, the phase difference across the junction remains constant and the system remains superconducting. However, if I exceeds I_c, a voltage drop appears across the junction, and the phase difference across the junction begins to change at a rate governed by Equation 2.7.

$$V = \frac{\hbar}{2e}\frac{d\theta}{dt} \tag{2.7}$$

where e is the electrical charge on an electron, and $\hbar$ is the reduced Planck's constant. This changing phase results in an alternating current with amplitude I_c, oscillating at the Josephson frequency, f_J. This is known as the AC Josephson effect.

$$f_J = \frac{2eV}{\hbar} \tag{2.8}$$

From this equation, we can see that f_J is directly proportional to V, meaning the Josephson junction is able to act as a perfect voltage to frequency converter. The constant of proportionality, $2e/\hbar$, equals 483.6 GHz/mV.

If we differentiate Equation 2.6 with respect to the superconducting phase difference θ, and combine with Equation 2.7, we obtain Equation 2.9. By comparing this equation to the general equation for an inductor, we are able to extract a definition for the Josephson inductance, shown in Equation 2.10.

$$V = \frac{\Phi_0}{2\pi I_c cos(\theta)} \frac{dI}{dt} \tag{2.9}$$

$$L_J = \frac{\Phi_0}{2\pi I_c cos(\theta)} \tag{2.10}$$

where Φ_0 is the Magnetic Flux Quantum $= 2.068 \times 10^{-15}$Wb.

2.2.1 Models for Josephson Junctions

In order to better understand the characteristics and dynamics of the Josephson junction beyond the ideal case shown previously in Equations 2.6 and 2.7, it is necessary to look at an electrical and mechanical model, known as the RCSJ and tilted washboard models respectively. These models allow us to predict the behaviour of Josephson junctions and their DC behaviour.

2.2.1.1 RCSJ model

The resistively and capactively shunted junction (RCSJ) model allows us to predict the electrical characteristics of the junction by analysing the current paths through the separate representative components of the junction.

The ideal junction with the current given by Equation 2.6, is placed in parallel with a resistor, representing the quasiparticle current across the junction when operating above T = 0 K, and a capacitor, representing the geometric parallel plate capacitance of the two superconducting electrodes of the junction. This model is shown graphically in Figure 2.3.

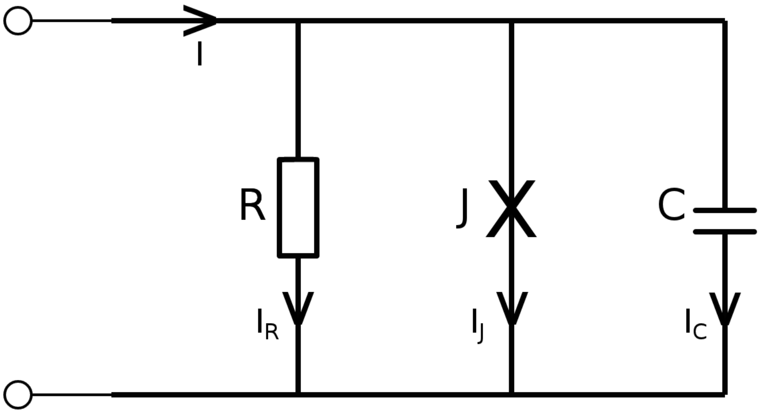

FIGURE 2.3: RCSJ model. The R, J and C elements correspond to the quasiparticle current, the supercurrent and the parasitic displacement current respectively.

The total current in the circuit is the combination of the current through each individual component; a supercurrent, quasiparticle current and a displacement current, shown in Equation 2.11.

$$\begin{aligned} I &= I_{junction} + I_{capacitor} + I_{resistor} \\ &= I_c sin(\theta) + C\frac{dV}{dt} + \frac{V}{R} \end{aligned} \tag{2.11}$$

Combining this with the AC Josephson effect, Equation 2.7, gives

$$I = I_c sin(\theta) + \frac{C\hbar}{2e}\frac{d^2\theta}{dt^2} + \frac{\hbar}{2eR}\frac{d\theta}{dt} \tag{2.12}$$

This is a second order differential equation, with the sin term making it non-linear. This can be rewritten as

$$I/I_c = sin(\theta) + Q^{-1}\frac{d\theta}{d\tau} + \frac{d^2\theta}{d\tau^2} \tag{2.13}$$

where the dimensionless time variable $\tau = \omega_p$t and ω_p is the plasma frequency.

$$\omega_p = \sqrt{\frac{2eI_c}{\hbar C}} \tag{2.14}$$

The quality factor Q related to the plasma frequency is

$$Q = \omega_p RC \tag{2.15}$$

The Stewart-McCumber parameter β_c, is a measure of damping, and is associated with the quality factor of the junction.

$$\beta_c = Q^2 = \frac{2\pi I_c R^2 C}{\Phi_0} \tag{2.16}$$

where Φ_0 is the magnetic flux quantum, $\Phi_0 = h/2e$. The junction damping affects the hysteresis observed in the current-voltage characteristics. From Equation 2.16 we can see the damping is strongly affected by the resistance of the junction.

2.2.1.2 Tilted washboard model

Another way to model the junction is by looking at the analogy of a particle on a washboard. This allows us to better understand certain junction phenomena, rather than looking at purely the numerical solutions.

The model involves a particle on a washboard in a viscous medium. The particle has a mass which corresponds to the capacitance of the junction, and the viscous drag of medium that the particle is in models the resistance of the junction. The mass of the particle and viscous drag force are given by Equation 2.17 and 2.18 respectively,

$$m = \left(\frac{\hbar}{2e}\right)^2 C \tag{2.17}$$

$$F_{drag} = \left(\frac{\hbar}{2e}\right)^2 \left(\frac{1}{R}\right) \frac{d\theta}{dt} \tag{2.18}$$

The position of the particle along the washboard equates to the phase of the junction. The tilt of the washboard is analogous to the bias current of the system, and the height of the wells in the washboard represents the energy required for the junction to enter the normal state. The particle moves along a potential profile with the following equation,

$$U(\theta) = -E_J cos\theta - \left(\frac{\hbar I}{2e}\right)\theta \tag{2.19}$$

where the Josephson energy E_J is given by,

$$E_J = \frac{\hbar I_c}{2e} \tag{2.20}$$

The potential barrier ΔU, or the height of the well, is proportional to the critical current of the device, as shown in Equation 2.21,

$$\Delta U = E_J(\sqrt{1-x^2} - xcos^{-1}x) \qquad (2.21)$$

where $x = I/I_c$.

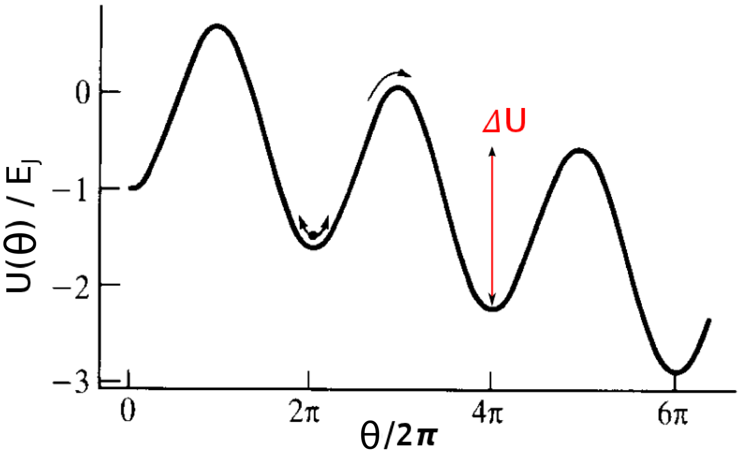

FIGURE 2.4: Tilted washboard model. ΔU is the normal state potential barrier related to the bias across the junction, and θ is the superconducting phase across the junction. Image taken from Tinkham [5]

From Equation 2.21, in the case where T = 0 and the bias current $I = 0$, we see that ΔU = $2E_J$. As the bias current is increased, shown graphically in Figure 2.4, ΔU decreases and the tilt of the washboard increases. Once I = I_c, the barrier is reduced to zero, and the particle enters the running state and travels down the washboard, corresponding to the junction having a changing phase. Recalling Equation 2.7, we can see that $\frac{d\theta}{dt} \neq 0$, and consequently a voltage appears across the junction.

In the case where T > 0 K, the particle will undergo thermal fluctuations whilst within the well, and the particle oscillates within the well at the plasma frequency, ω_p. If the well height $2E_J$ is significantly larger than the thermal energy of the particle, these thermal fluctuations remain insignificant, time average to zero, and the junction remains superconducting. As T increases towards T_c, k_BT becomes more significant and thermal activation of the particle, causing it to leave the well and entering the voltage state, becomes more likely. As I tends towards I_c and T > 0, there is a probability that the particle will thermally activate over the barrier ΔU and enter the running state at a value of I $< I_c$. This thermal activation of the particle into the running state is a statistical process, and as such will occur at a different value of I each time the experiment is run. When at T $>$ 0K, I_{sw} is the switching current at which the junction switches to the voltage state, equivalent to I_c at T $=$ 0.

When in the running the state, the particle develops inertia, dependent on the viscous drag force acting on the particle. As the bias current is reduced, ΔU increases, and the particle is then eventually retrapped in a well. The viscosity force acting on the particle determines how it retraps into a well, analogous to the damping in the system causing the junction to retrap and return to the superconducting state.

In the situation with no damping at T $=$ 0, the particle remains in a well and escapes when I $= I_c$. The particle will remain in the running state and only retrap when I $=$ 0. As the bias current required for the particle to escape the well is greater than zero, we see hysteresis in the current voltage characteristics, as shown in Figure 2.5.

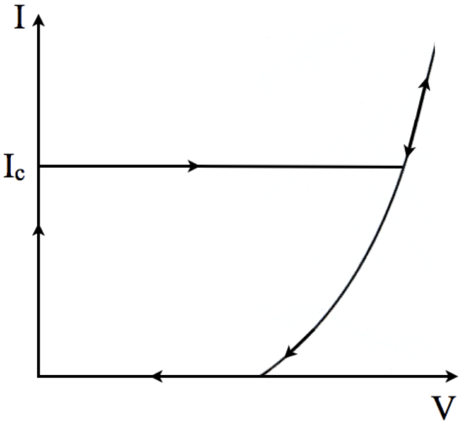

FIGURE 2.5: Josephson junction current-voltage hysteresis with no damping. Image taken from Saleem [18]

When the system is underdamped, where $\beta_c >> 1$, and the current is increased, the junction will switch at I_c to the voltage state, where V $\approx V_g = 2\Delta(T)/e$. As the current is then reduced, due to the damping in the system, the particle will retrap into a well at a bias current greater than zero, called the retrapping current, $I_{r0} \approx 4I_c/\pi Q$, as shown in Figure 2.6. I_{r0} refers to the situation at T $=$ 0, but due to the retrapping of the junction being a thermally controlled statistical process when T > 0, I_r is used in the usual case when T > 0.

When $\beta_c \lesssim 1$ and the system is overdamped, once the particle escapes the well, the viscous medium causes it to immediately retrap into the next well. After a period of time, the particle will escape again, the process continuing from one well to the next, and is called phase diffusion. In the overdamped case, suppression of the hysteresis is observed in the current voltage characteristics, as shown in Figure 2.7.

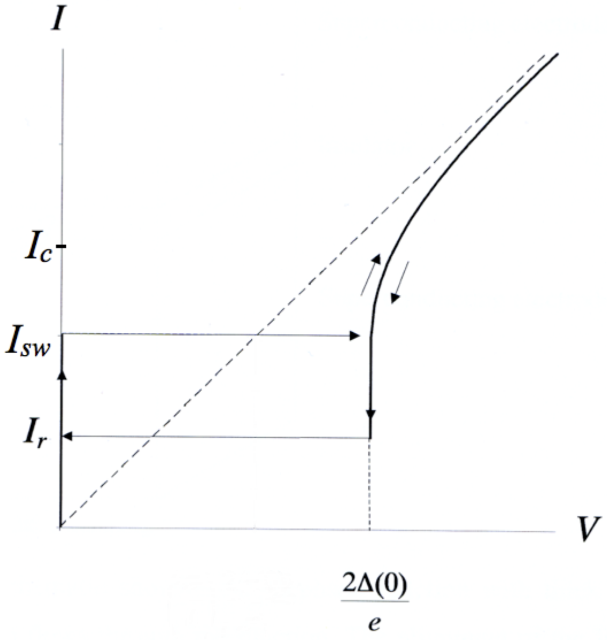

FIGURE 2.6: Underdamped Josephson junction current-voltage hysteresis at T>0. Image taken from Chana [19]

As I tends towards I_c in the overdamped situation and ΔU is reduced, phase diffusion events occur more often. As the timescale of these statistically random events is very short, they manifest in current voltage measurements as an averaged DC voltage on the supercurrent branch, smoothing out the transition from superconducting to resistive state.

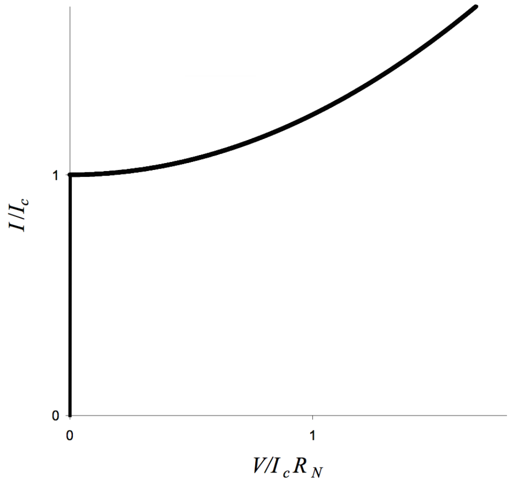

FIGURE 2.7: Overdamped Josephson junction current-voltage hysteresis. Image taken from Chana [19]

2.2.1.3 Transmission line model

The transmission line model describes a conducting wire made up of an infinite number of uniform unit cells along the length that illustrates how the behaviour of a travelling wave will change as it propagates along the line. Each unit cell consists of components representing the different electrical characteristics of the transmission line: the inductance, capacitance and resistance. In order to better understand the behaviour of a signal travelling through a series of superconducting Josephson junctions, we can model each junction as a unit cell of a transmission line using distributed components: the Josephson inductance with a capacitance to ground, as shown in Figure 2.8. Although each junction has an associated capacitance and resistance, as discussed in the RCSJ model, the capacitance is modelled as an rf short circuit when dealing with high-frequency microwave signals, and the quasiparticle resistance is assumed to be zero as the junction is superconducting, allowing the rf behaviour of the superconducting junction to be modelled solely by the inductive element.

The velocity of a signal travelling through a general LC transmission line is given by Equation 2.22.

$$v_p = \frac{1}{\sqrt{LC}} \tag{2.22}$$

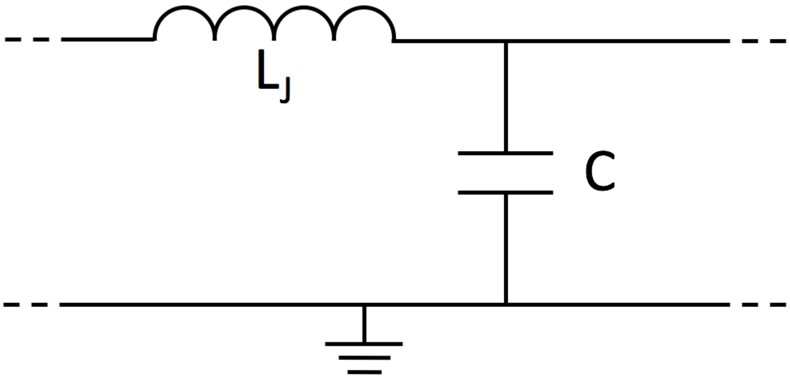

Figure 2.8: LC superconducting transmission line model showing the Josephson inductance L_J and capacitance C to ground per unit cell.

where L and C are the inductance and capacitance to ground per unit length.

The velocity is also related to the wavenumber of the signal, as shown in Equation 2.23, where $\Delta\phi$ is the wavenumber or amount of phase change of the signal per unit length of the transmission line.

$$\Delta\phi = \frac{2\pi f}{v_p} \tag{2.23}$$

By combining Equations 2.22, 2.23 and 2.9 for the Josephson inductance, and using a rearranged version of Equation 2.6 for $cos(\theta)$ (Equation 2.24), we are able to derive the relationship between the signal phase change per junction in relation to the DC bias through the Josephson inductance (Equation 2.25).

$$cos(\theta) = \left(1 - \left(\frac{I}{I_c}\right)^2\right)^{\frac{1}{2}} \tag{2.24}$$

$$\Delta\phi_J = 2\pi f\sqrt{L_J C} = 2\pi f\sqrt{C}\sqrt{\frac{\Phi_0}{2\pi I_c}\left(1 - \left(\frac{I}{I_c}\right)^2\right)^{-\frac{1}{2}}} \tag{2.25}$$

These equations will become relevant when we later look at utilising a stack of IJJs as a current bias controllable phase shifter.

2.3 Intrinsic Josephson Junctions

Since the discovery of the Josephson effect in 1962, many different materials, fabrication methods and designs have been utilised to construct Josephson junctions using both LTS and HTS, using what are known as SNS, SCS and SIS junctions (S, N, I and C denoting superconductor, normal metal, insulator and constriction). Thin film layering, step-edge fabrication, grain boundary and constriction designs are examples of methods used to fabricate extrinsic junctions [20–23].

In 1992, Kleiner *et al*. first discovered intrinsic Josephson junctions (IJJs) within the naturally formed layering in $Bi_2Sr_2CaCu_2O_8$ (BSCCO) single crystals [4]. BSCCO belongs to the cuprate family of HTS; the cuprate superconductors form in layers, alternating between superconducting CuO_2 and insulating layers made up of other elements. It is this natural superconductor/insulator layering in the c-direction within the lattice that forms the IJJs. Other commonly used cuprate HTS are yttrium barium copper oxide (YBCO) and thallium barium calcium copper oxide (TBCCO). For example, in $Tl_2Ba_2CaCu_2O_8$ (Tl-2212), the superconducting CuO_2 layers are 3Å thick and these alternate with insulating layers of 12Å thick. The crystal structure is shown graphically in Figure 2.9.

In contrast to LTS materials, the intrinsic layering in cuprate HTSs gives rise to electromagnetic anisotropy that is not seen in the isotropic metallic LTSs. This anisotropy refers to the contrasting behaviour of the superconductor in the ab-planes and c-direction of the crystal lattice. The anisotropy factor can vary dramatically depending on the material and stoichiometry, ranging from 10 for YBCO to 10^5 for BSCCO [7]. It is this anisotropy in the atomic scale layering that is exploited for the design and fabrication of IJJ stacks.

Table 2.1 shows material properties for TBCCO and YBCO for comparison. The unit cell for YBCO in the c direction is significantly less than TBCCO, resulting in stronger coupling between the superconducting layers and a much lower anisotropy factor. The strong

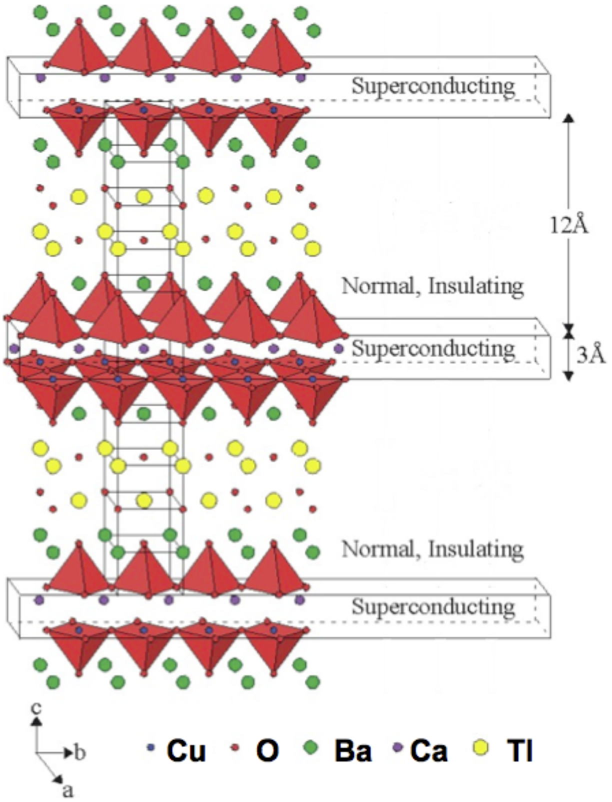

FIGURE 2.9: $Tl_2Ba_2CaCu_2O_8$ crystal structure showing the supeconducing cuprate layers separated by the ceramic insulating layers creating the weak link necessary for intrinsic Josephson effects. Image taken from Saleem[18]

coupling between the superconducting cuprate layers eliminates any intrinsic Josephson effects within YBCO, however it is possible to produce extrinsic Josephson junctions using step-edge, grain boundary junctions or microbridge junctions [24–26].

	T_c/K	Lattice Parameter/Å		Coherence Length/nm		J_c/Acm^{-2}	
		a	c	ab	c	ab	c
TBCCO	107 [27]	3.85 [28]	29.3 [28]	2 [29]	0.2 [19]	10^4 [30]	10^6 [31]
YBCO	92 [32]	3.82 [33]	11.7 [33]	2 [34]	0.2 [34]	10^7 [35]	10^5 [35]

TABLE 2.1: Comparison table of superconducting properties of TBCCO (Tl-2212 phase) and YBCO (Y-123 phase)

The behaviour of an individual junction has been explained in Section 2.2, but by fabricating a stack of series junctions in a HTS such as TBCCO, the current-voltage characteristics consist of a superposition of multiple branches at increasing voltages. Figure 2.10 shows example data for a stack of underdamped IJJs. Each of the branches in the

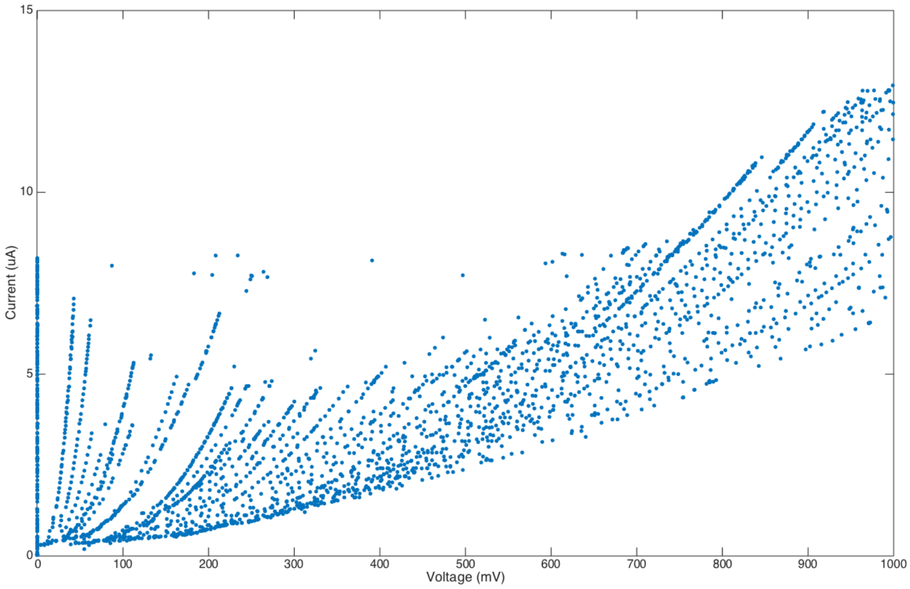

FIGURE 2.10: Current voltage characteristics for a stack of IJJs fabricated in TBCCO. Each branch corresponds to an individual junction within the stack switching to the normal/resistive state

current voltage characteristics corresponds to an individual junction within the stack being in the normal state. As the bias current is gradually increased, switching from one branch to the next is indicative of additional branches going from the superconducting to resistive state. As the current is then swept back down, retrapping events happen until the junction stack returns to being superconducting.

Research exploiting Josephson effects in TBCCO has been done by multiple groups ([36–39]), but it has not been investigated as extensively as BSCCO. The work presented in this thesis is done with 20^o vicinally cut Tl-2212. Using vicinal films provides the advantage of easier fabrication methods due to the inherent tilt of the crystal structure layering, and simpler design layouts over single-crystal mesa structures commonly fabricated using BSCCO.

When using single-crystal HTS, such as BSCCO, mesa devices are most commonly fabricated to realise a stack of IJJs. When using TBCCO thin films, alternative methods

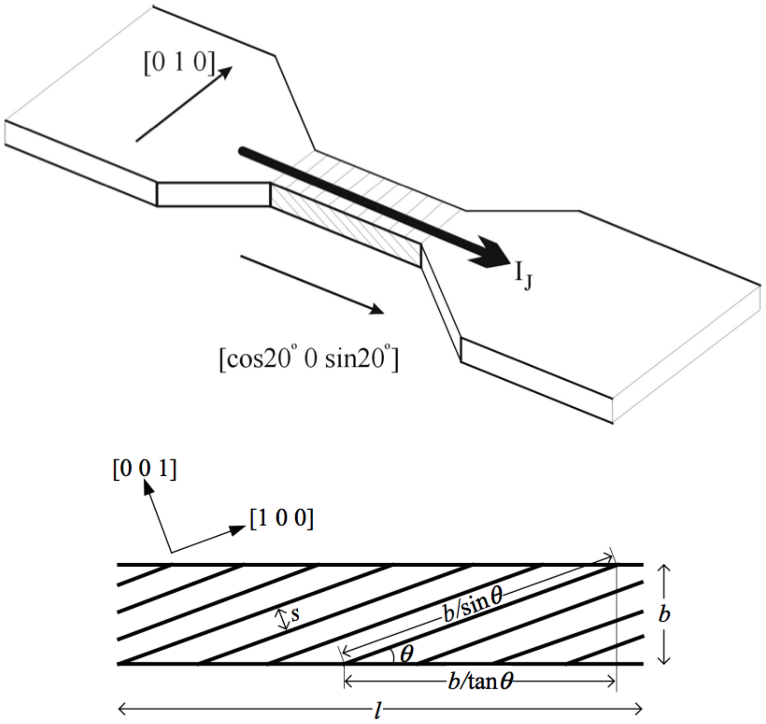

FIGURE 2.11: Misaligned vicinal microbridge with $\theta = 20^o$.
Image taken from Chana [19]

for fabricating a stack of IJJs are used, however all devices are designed to allow for biasing in the c-direction across the cuprate layers. Fabrication techniques will be further explained in Section 4.1. It is also possible to create Josephson junctions using HTS that are not intrinsic but extrinsic devices. A review of these methods can be found by Gross et al. [40], but are not relevant to this work.

When designing devices using vicinal HTS films, it is necessary to be able to calculate the number of junctions in a device, N. Equation 2.26 is used to calculate the number of junctions N in a stack, taking into account the in-plane short circuit that arises from the misalignment angle θ of the c-axis [19].

$$N = \frac{lsin(\theta) - bcos(\theta)}{s + t} \tag{2.26}$$

where l is the length of the junction stack, b is the thin film thickness, s is the insulating layer thickness in the crystal lattice $= 12$Å, and t is the superconducting CuO layer thickness = 3Å, as shown in Figure 2.11. For example, a 20^o vicinal 300nm thick and 1mm long track contains approximately 227,000 intrinsic Josephson junctions; a junction density not achievable through extrinsic junction fabrication methods.

2.3.1 Phase locking

When multiple junctions are connected together, it is expected that they will act independently of each other; parameter changes of one junction will have no effect on the behaviour of a nearby junction [41, 42]. It is however possible to couple the junctions, locking the phases together, thereby synchronising the behaviour and opposing perturbations to the system.

Phase locking is the general term used to describe the synchronisation of an oscillator to the phase of another signal. In the context of Josephson junctions, phase locking has been widely investigated for Josephson oscillators used for millimeter wave emitters [43–47], and for voltage standard devices [42, 48, 49] utilising the AC Josephson effect shown in Equation 2.8.

In these applications, multiple junctions are phase locked to synchronise their behaviour and amplify the desired effect. In voltage standard experiments, using arrays of coupled junctions produce higher voltages which simplify the calibration, reduce the uncertainty in the measurement and the effect of thermal drift [50]. In emission applications, phase locking of junctions can result in an N^2 increase in power emission, where N is the number of coupled junctions [43, 51]. This phase locking can be achieved though various methods, but strongest emission appears to arise from geometric resonance coupling between intrinsic junctions in an array [52, 53], where the geometric resonance of the track is designed to match the frequency of the Josephson oscillations of the junctions to amplify the emission.

There are a variety of coupling mechanisms that have been exploited for phase locking of Josephson junction arrays including high-frequency electromagnetic coupling [54], geometric resonance coupling [52, 53] and travelling electromagnetic waves [43]. A review of these coupling mechanisms has been presented by Jain et al. [55].

Galin et al. [43] show that because of asymmetry in the emission pattern from their linear junction array, the synchronisation of the junctions cannot be solely due to geometric standing waves. They attribute the coupling to a travelling-wave effect along the array, supported by recent work by Kurin et al. simulating Josephson travelling wave antennae [56]. It is thought that this may be a coupling mechanism present in the IJJ transmission lines presented later in this work.

2.3.2 Intrinsic Josephson Junction Transmission Line

As discussed in section 2.2.1.3, a Josephson junction can be modelled as a unit cell of an infinite length track of junctions using the inductive and capacitive lumped elements connected by perfect conductors. If we apply this model to the high density intrinsic Josephson junctions found in HTS, we can begin to simulate the behaviour of a large number of junctions in series in a IJJ track. By assuming junction uniformity along the length of a vicinal IJJ transmission line through one of the phase locking mechanisms outlined previously, we can apply the equations derived in section 2.2.1.3 to the intrinsic junctions found in the layering within HTS such as TBCCO. It is thought that by transmitting an rf signal along the IJJ transmission line, there will be superconducting low-frequency coupling between neighbouring junctions as shown by Jain et al. [57].

In a standard transmission line model, the inductance and capacitance values are per unit length, however in an IJJ transmission line, it is more relevant to use an individual junction as the unit cell length. This allows us to replace the inductance and capacitance per unit length of the line with the Josephson inductance, shown in Equation 2.10, and the capacitance to ground per junction, giving us the $\Delta\phi_J$ per junction, shown in Equation 2.25. As already stated, if we assume approximate junction uniformity along the track and phase locking across the junctions, we are able to sum the phase shift per junction along the line, and by introducing an N term to Equation 2.25, this gives us the total phase shift for the IJJ transmission line, $\Delta\phi_{total}$.

$$\Delta\phi_{total} = 2\pi f N\sqrt{L_J C} = 2\pi f N\sqrt{C}\sqrt{\frac{\Phi_0}{2\pi I_c}\left(1-\left(\frac{I}{I_c}\right)^2\right)^{-\frac{1}{2}}} \tag{2.27}$$

Chapter 3

Existing Research

3.1 Previous research into Phase Shifters

Phase shifters are an important component in computing and communication systems, such as array antennas and phased arrays. Phased array antennas are solid state devices that can eliminate the need for a rotation mechanism of regular antenna systems for beam steering. This principle can also be very useful for directing an antenna to compensate for changes whilst the antenna base is moving, for example on a vehicle or satellite in space, where mechanical motion is especially hard to actuate. They also find use in radar and weather monitoring for future airspace monitoring systems [58]. Phased array antennas have also recently been demonstrated in use for the first prototype 5G Verizon antenna system created by Ball Aerospace and Anokiwave[1], where they highlighted the increased range, data rate, power efficiency and reduced interference of the system aimed at the next generation of telecommunications products and networks.

Phased array antennas rely heavily on phase shifters for their operation; it is possible to control the direction of a signal from multiple transmitters by altering the phase of different emitters to ensure constructive interference of the emitted signal at the correct

---

[1] http://www.microwavejournal.com/articles/28100-ghz-active-array-antenna-enables-rapid-5g-prototyping

angle. When used for recieving signals, array antennas pick up a signal frequency at different phases for each reciever, and then phase shift each path to combine and intensify the desired signal and attenuate the undesired frequencies. To meet the needs of such systems, the optimum phase shifter should have a wide phase range, low insertion loss, low transmission loss variation with phase change, and low power consumption. A review of the theory behind microwave phased-array antennas can be found written by Stark [59].

Digital phase shifters allow direct integration into existing monolithic microwave integrated circuits (MMIC) using established CMOS fabrication techniques. This benefit comes with the compromise on cost, insertion loss and chip size as the number of bits increases. Recent work from Sun *et al.*[60], Hiyashi *et al.*[61], Wang *et al.*[62] and Zheng *et al.*[63] shows digital transistor based phase shifters working in a range of frequency bands with up to 6 bits. However, they suffer from high insertion losses in excess of 10dB, require a relatively large circuit area and can need complex bias DAC and control circuitry. The discrete nature of the digital phase shifters require high phase accuracy and very low variation to ensure the exact subsequent wave interactions are as required, which can be difficult to implement. These devices aren't discussed in depth here as digital circuitry is not relevant to this work. A basic review of the different digital approaches can be found written by Poon and Taghivand [64].

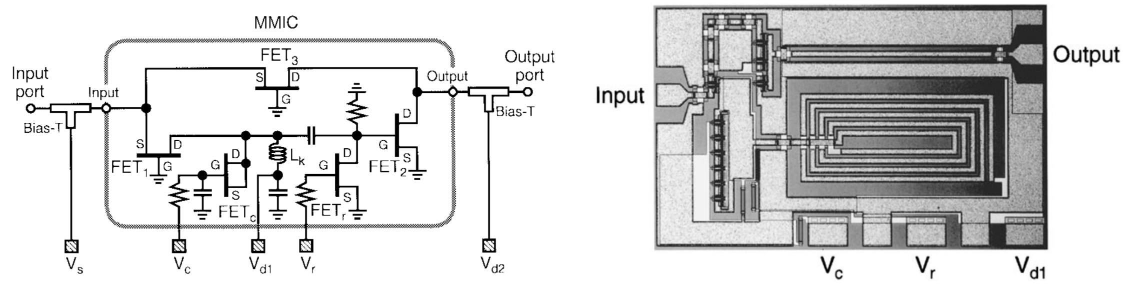

(a) MMIC phase shifter circuit diagram illustrating the design complexity.

(b) Photograph of MMIC phase shifter chip.

Figure 3.1: MMIC phase shifter designed by Hiyashi *et al.* [61]

Analog phase shifters have been fabricated utilising variable reactance components, such as varactor diodes, to control reflection and delay characteristics in transmission lines. Hiyashi *et al.* [61] designed a gallium arsenide (GaAs) metal-semiconductor field-effect transistor (MESFET) active integrated circuit (IC) coupled with a variable resonance circuit to achieve a large analogue phase variation using a varactor and active FET based variable inductance (Figure 3.1). They reported 360^o of phase shift with insertion gain of 2dB between 2.42 and 2.46GHz from a 2.3mm^2 device, with the gain in the system being provided by the multiple FETs involved in the shifter. As such, their device has a high system complexity for the FET control and requires multiple input and control biases.

Nagra *et al.* [65] used a GaAs high impedance transmission line, periodically loaded with varactor diodes to change the phase shift by controlling the bias voltage across the diodes. They were able to achieve 360^o of phase shift at 20GHz with a 4dB insertion loss. Ellinger *et al.* [66] similarly developed a lumped element varactor loaded transmission line and achieved 360^o voltage-controlled phase-tunability with 4dB insertion loss over a 2GHz range from 4.5GHz. Both devices are contained in a small area of approximately 1mm^2 and require less control electronics and biasing than their digital counterparts, however still rely on complex multi stage fabrication techniques requiring implant doping processes and multi-layer fabrication for capacitance and diode construction, as seen in Figure 3.2 below.

Reflective-type phase shifters use variable capacitances in a branch-line configuration, and can be size limited as they require the branches to be separated by $\lambda/4$. This can restrict the bandwidth of these devices, alongside their relatively high loss and large chip size. Upshur *et al.* [67] and Henoch *et al.* [68] both use varactors as variable capacitances, however these designs are large in size, limited in their frequency range and suffer from large variation in transmission with shifting phase. Ellinger *et al.* uses MESFETs as an alternative to varactor diodes in a branch-line circuit, which do not have the same

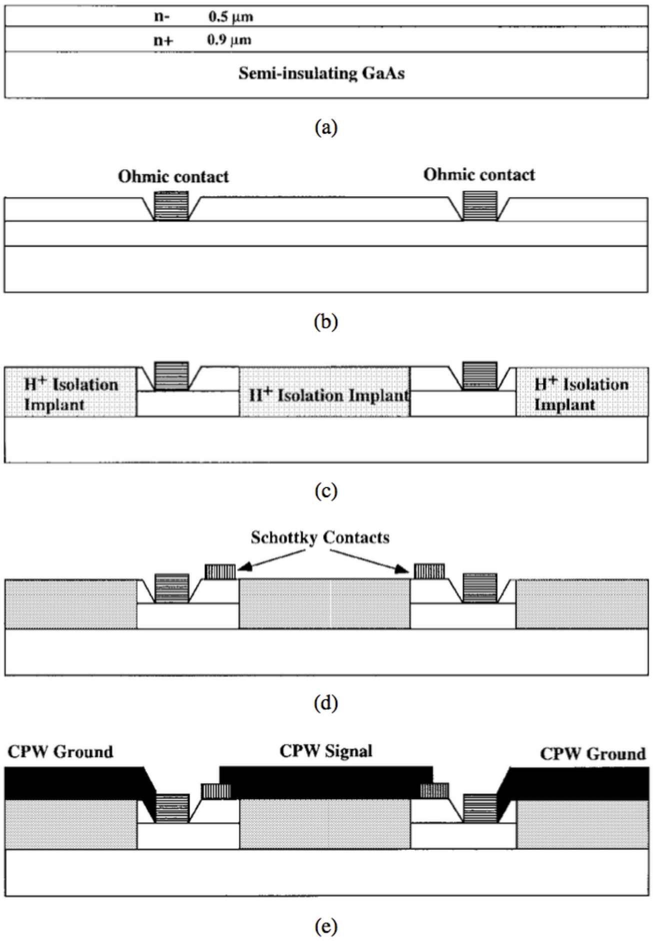

FIGURE 3.2: Multi-stage fabrication technique used by Nagra *et al.* [65] to create GaAs transmission line with periodic veractor loading.

capacitance range. However, they use reflective termination circuits to increase the phase change to over 360^o and significantly reduce the chip dimensions, but still suffer from high insertion losses, variation loss and limited frequency range [69]. Figure 3.3(a) from Ellinger *et al.* shows the design for the application of reflective-type phase shifters in an array antenna system, using the phase shifters to compensate for phase shifts between the antenna signals before mixing and filtering the signal. Figure 3.3(b) shows their schematic of the branch-line coupler using lumped elements leading into reflective loads, in which the MESFETS are used to control the reflection characteristics and tune the phase shift.

Vector modulators provide an alternative method of signal phase shifting in conjunction

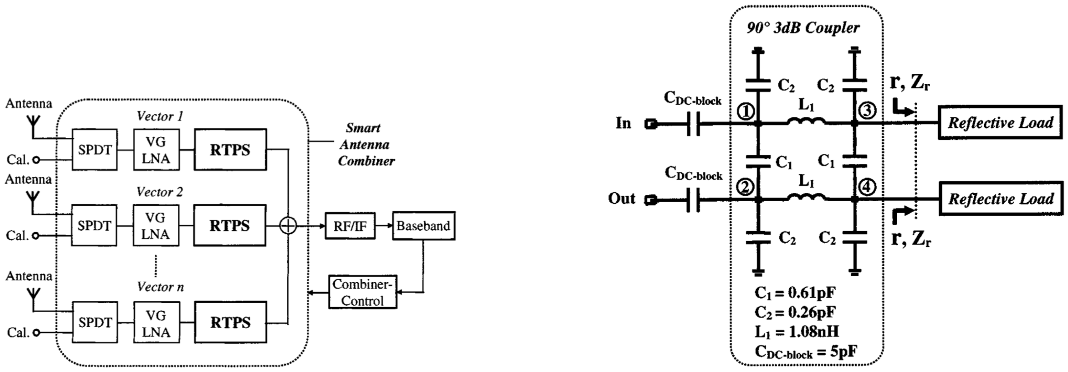

(a) MMIC phased antenna array receiver system schematic illustrating the application of reflective-type phase shifters (RTPS).

(b) Circuit layout of the reflective-type phase shifter, which uses the reflection factor r to control the phase shift.

FIGURE 3.3: Images taken from Ellinger *et al.* [69] illustrating the application of the reflective-type phase shifters in an MMIC system and the circuit layout of the phase shifter.

with amplitude modulation. Vector modulators split an incoming signal into an in-phase and quadrature signal, or 3 phase 120^o shifted signals, which are then combined in different proportions to control the amplitude and phase modulation; 2 examples of such systems can be found published by Grajal *et al.* [70] and Ellinger *et al.* [71]. Figure 3.4 shows the vector modulation chip fabricated by the Ellinger group, which benefits from low power consumption, small chip dimensions and low insertion loss of less than 2dB. However, to achieve full 360^o phase variation, controlled weighting of 2 out of 3 separate control voltages are required with substantial control circuitry, as seen in the diagram.

3.2 Superconducting Phase Shifters

For further development and advancement of microwave circuits, superconducting phase shifters have been the subject of research to allow for reduction of conduction losses and incorporation into existing superconducting systems. Low temperature phase shifters have been fabricated from LTS such as niobium [72–74], however since their discovery in 1986, HTS have been more extensively investigated as a more feasible device solution

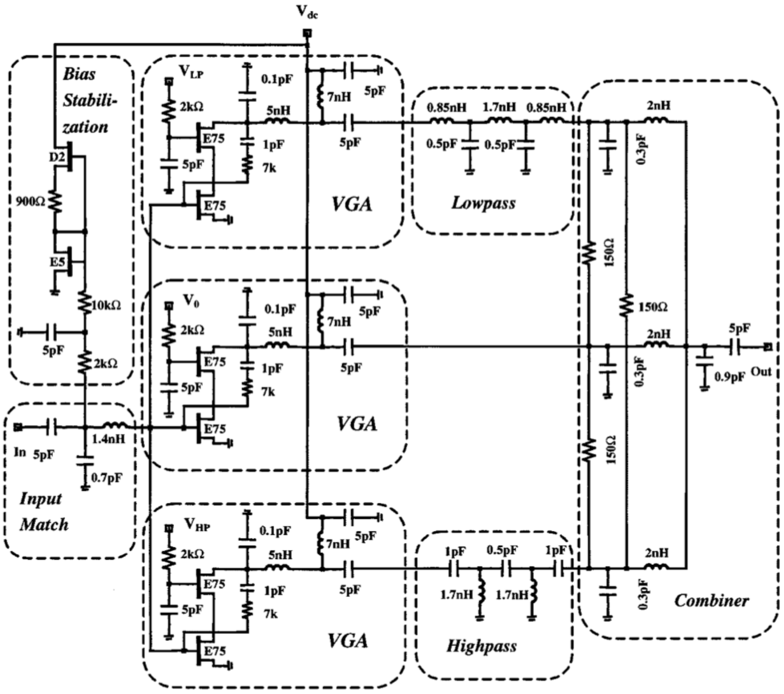

FIGURE 3.4: Vector modulator circuit developed by Ellinger *et al.* [71], highlighting the circuit complexity required to achieve phase shift using MMIC designs with FET biasing circuitry.

due to reduced cryogenic costs. The two main implementations of HTS are in ferrite coupled waveguides and lumped-element transmission line microstrip structures.

Ferrite waveguide structures rely on applied magnetic and electric fields to change the permittivity of the ferrite substrate, consequently resulting in a change in phase of the transmitted signal along the coupled conductor. However, these structures are bulky, and in order to reduce size, a sacrifice must be made with greater insertion and conduction losses. By using a superconductor, the conduction losses can be eliminated, however due to the Meissner effect, this can prove problematic having to incorporate magnetic isolation of the ferrite biasing from the superconductor.

Dionne *et al.* [72] fabricated a low-Tc niobium superconducting meander transmission line coupled with a ferrite toroid to achieve magnetic flux isolation, and were able to achieve in excess of 1000 deg per dB of loss at 9GHz, the frequency corresponding to the quarter wavelength of the meander. Below 8GHz, they state that their device suffers from increased loss as the microwave signal interacts with ferrite resonance effects. Yeo and

Lancaster implemented a toroidal magnetic structure similar to Dionne with a YBCO meandering superconducting transmission line [75], which achieved 55 degrees of phase shift for a low insertion loss of 1.5dB at approximately 7GHz. However, they do state that greater phase shifts are achievable, but requires greater magnetisation currents, larger than 1A used for the experiment, to saturate the ferrite material. As with the results from Dionne, they also state that higher loss and less phase shift is produced at lower frequencies below 4.5GHz due to the microwave signal coupling to resonances in the partially magnetised ferrite substrate. More recently, Kwak *et al*. [76] reported results from a YBCO and ferromagnetic barium strontium titanate (BST) multilayer coplanar waveguide (CPW) electrically excited device that yielded a phase change of 162 degrees with 2.97dB of loss (54 deg/dB) at 10GHz with a 40V bias. Kuels *et al*. [77] used a YBCO and ferrite strontium titanate (STO) coupled microstrip line phase shifter (CMPS) device to achieve high frequency phase shift of 390 degrees at 16GHz, with approximately 30 deg/dB loss. The device design and fabrication methods used appear simpler than that found in other reports due to the lack of induction coil, however they still require trilayer thin film deposition and fabrication.

Transmission line phase shifters rely on a variable inductance or capacitance in a periodic filter structure to produce phase shift, and has not been investigated as deeply as the ferrite structures. Cai and Chen fabricated a microwave phase shifter using a simple YBCO microstrip geometry on a cubic zirconia substrate [78], and observed 5 degrees of phase shift at 1GHz for 0.3dB of signal attenuation at 95mA current bias. Due to the microstrip design, there is very low insertion loss from the device, however due to the low level of dc bias variation in the film inductance, there is also very low phase variation.

In 1992, Jackson *et al*. [79] designed a distributed Josephson inductance YBCO tranmission line, incorporating more than 1000 weakly coupled SQUIDs. The coupled SQUIDs allow the inductance, and consequently the wave velocity and phase shift, to be tuned by an external magnetic field or a control current. They were able to produce only small phase variations of 20 degrees and 0.5 degrees, with external field and dc bais respectively, but with low insertion loss of 2dB. They attributed the low phase change to fabrication difficulties and concluded that more work was necessary to further develop the idea. Similar results were also presented by Takemoto-Kobayashi *et al.*[80], Durand *et al.* [81] and simulations into the coupling dependance were performed by Perold [82]. More recently, Kokkoniemi *et al.* [83] investigated a 3 SQUID coupled transmission line phase shifter for use alongside microwave photon Qubit systems. They achieved 67.5 degrees of phase variation at 6.3GHz through magnetic tuning, and speculated that by expanding the number of SQUIDs would increase the phase change and expand the frequency range of operation.

Eom *et al.* exploit the non-linearity of the kinetic inductance of superconductors for use in a transmission line travelling wave parametric amplifier (TWPA), able to operate near the quantum noise limit due to the low dissipation of the superconductor, and not limited to the small frequency operating range and slow response time normally found with superconducting parametric amplifiers [84]. Applying the assumption of the superconducting transmission line being dispersionless, they show that the signal gain in a parametric situation with a co-travelling pump tone is given by the following equation,

$$G_s = 1 + (\Delta\theta^2) \tag{3.1}$$

where $\Delta\theta$ is the phase shift of the pump tone. With an engineered dispersion relationship between the signal and the pump, the gain of the signal travelling through the transmission line becomes exponential;

$$G_s = exp(2\Delta\theta)/4 \tag{3.2}$$

They fabricated a 0.8m spiral transmission line using niobium titanium nitride (NbTiN). Their NbTiN films had a T_c of approximately 14K, with values as high as 15.5K reported elsewhere from other groups [85]. Eom et al. state that as NbTiN is a material with a high normal state resistivity, this results in greater kinetic non-linearity due to the relationship between the resisitivity and the phase velocity in the material [84]. This length of LTS transmission line resulted in a phase change of $\approx$ 470 degrees when biased at 1.4mA, equating to approximately 590 degrees/metre. The gain results published from the device also show a broadband gain of 10 dB from 8GHz to 14GHz, and they conclude that further development and design improvements could see the gain exceed 20 dB over a broader range. The fabrication of such a device using only lithographically patterned metal on substrate illustrates the potential for simpler fabrication techniques to be able to achieve high levels of phase difference for new applications in parametric amplifiers. Although their experiments were performed with a LTS at liquid helium temperature of 4.2K, they hoped their results will stimulate further research in the field of superconducting delay lines.

When assessing the current state of devices in this field, consistently there appears to be a correlation between complexity of the device with the control circuitry, and the degree of phase variation achieved. The simpler HTS designs fabricated using YBCO, such as the microstrip geometry used by Cai and Chen, produce significantly less phase shift than the SQUID coupled, or ferrite waveguide devices due to the reduced tunability of the superconducting inductance. All the work with YBCO has been performed using c-axis grown thin films with in-plane biasing. By DC biasing across the intrinsic Josephson junctions found in the high density layering within the HTS cuprate crystal structure, a misaligned vicinal film may present the opportunity for higher levels of phase tunability in smaller devices, and remove the need for magnetic field tuning and complex ferrite coupled structures.

Chapter 4

Experimental Details

This chapter contains details regarding the preparation, equipment and techniques used in sample fabrication and experimental procedure. This includes film growth, photolithography, focused ion beams and cryogenic measurement system setup. The fabrication is based upon techniques initially devised by Dr. Sajid Saleem.

4.1 Sample fabrication

4.1.1 Film growth

The material used for these experiments was $Tl_2Ba_2CaCu_2O_8$ (Tl2212), which was grown on $LaAlO_3$ (LAO) substrates. The substrates were ordered from Crystal GmbH[1] and the $Tl_2Ba_2CaCu_2O_8$ films were grown and characterised by Dr Susannah Speller at the Department of Materials, University of Oxford[2]. $LaAlO_3$ is used as the substrate for this growth due to the very good lattice matching with Tl2212; 3.972Å for LAO compared to 3.855Å for Tl2212 [86]. LAO can have issues with dielectric constant inaccuracies of 2% from the base $\epsilon_r = 24$ brought about from the phase tranisition at 500^oC during the HTS

---

[1] http://www.crystal-gmbh.com/

[2] http://www.materials.ox.ac.uk/peoplepages/speller.html

growth temperature variation [86]. Although this inaccuracy makes LAO not the ideal substrate material for microwave applications, it is still the most compatible material choice for Tl2212 growth over other materials such as MgO and $SrTiO_3$. The work was done using 10mm x 10mm x 0.5mm vicinal LAO substrates, misaligned by 20^o from the c-axis (normal to the substrate surface) and polished on one side. The misalignment is achieved by a vicinal cut of the substrate, which transfers the misalignment to the thin film during the epitaxial growth.

The films were grown using physical vapour deposition in a two-step process. Firstly, amorphous copper-deficient Ba-Ca-Cu-O was deposited onto the polished side of the $LaAlO_3$ substrate by a RF magnetron sputterer. Control of deposition time is the main factor determining the film thickness. Following this, the sample was placed into a sealed glove-box to allow for the manipulation of the thallium source powder and sample preparation. The sputtered precursor sample is then placed in a sealed aluminium crucible in the furnace with the $Tl_2Ba_2CaCu_2O_8$ source powder. The crucible is sealed with thin foil to prevent loss of Tl_2O vapour and to maintain a uniform vapour pressure across the sample. The furnace was then heated to between 800 and 860°C for 15 hours. Following the thalliation, the sample cooled slowly overnight before being removed from the crucible. The overnight cooling is necessary to ensure the sample cools without cracking due to the thermal expansion mismatch between the thin film and the substrate. Once the sample had been removed from the glove-box, it was washed in water and stored ahead of patterning. The sample T_c is confirmed before patterning using SQUID magnetometry. The samples used in this work had Tl2212 film thicknesses of 300 and 600nm.

4.1.2 Photolithography and Mask Design

Following the film growth, sample patterning is performed using photolithography in conjunction with argon ion milling.

Photolithography uses a UV masking technique to determine the regions of material that will be subsequently removed. The masks for this work were designed using Inkscape software[3], and then chrome printed onto a 3" "Super High Res" glass mask plate by JD Photo Tools[4].

Initial 2 point microwave measurements were made on a 200μm wide microstrip design that was created through a copper laser cut shadow mask and argon ion milling. Following this, two different photolithography masks were used for the work presented in this thesis; one to allow for fabrication and 4 point current-voltage measurements of stacks of 'short' junctions (less than 10μm in length), and one for 2 point microwave transmission measurements of tracks of 3.5mm in length. Both masks designs are shown below in Figure 4.1. The 4 point measurement mask was designed to fit on a 1cm^2 sample, and the 2 point RF measurement mask was designed for 5mm^2 samples. The dimensions of these samples was determined by the size of the respective sample holders.

When designing the mask layout, there were multiple considerations that had to be incorporated to ensure accurate measurements were being made without introducing innaccuracies into the experiment. The mask design for the 4 point DC measurements shown in Figure 4.1(a) was determined by different factors governed by the material properties. The contact line lengths were designed to be at least 2 orders of magnitude larger than the width of the track to be measured to ensure the superconducting track lines remain below the critical current density, J$_c$, whilst the properties of the much thinner device tracks were being investigated. The pad size was designed to be 300μm^2 to allow enough space to make contact with the Au wire Wedge bonder. The mask design for the 2 point coplanar waveguide transmission line tracks was governed by the spacing between the coplanar tracks required for sufficient rf isolation. Looking at Figure 4.1(b), the large dark areas between the tracks are the ground planes, connected to the system ground through Au wire bonds bonded to the thermally evaporated gold

---

[3] https://inkscape.org

[4] http://www.jdphoto.co.uk/

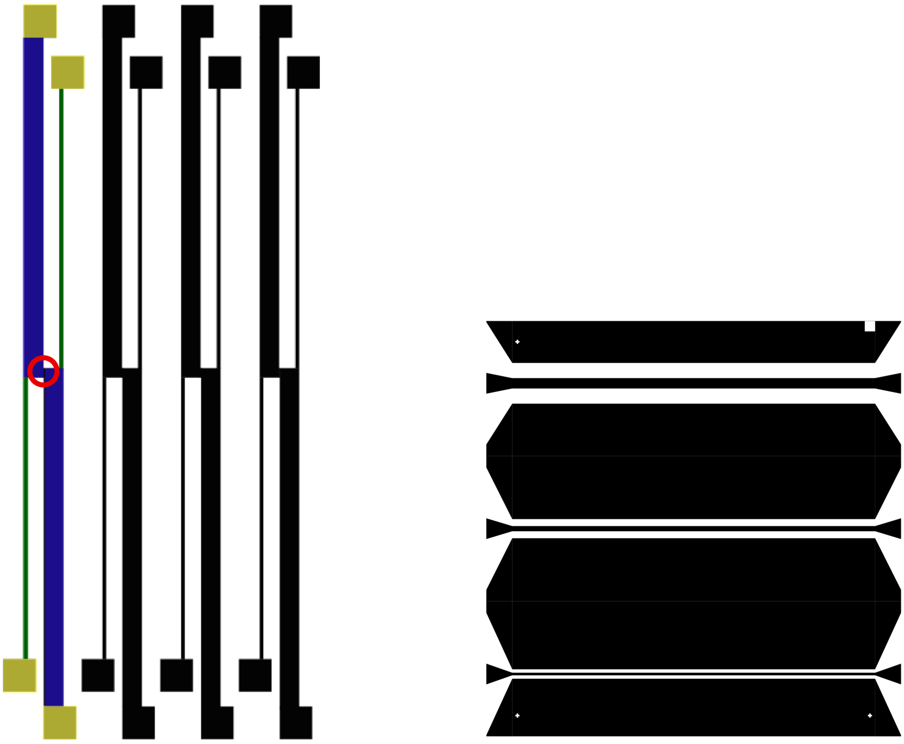

(a) 4 point measurement mask design with 6 to 10μm track length. The IJJ track region is shown circled in red, the gold coated contact pads shown in yellow, the current contact leads highlighted in blue and the voltage contact tracks shown in green.

(b) 2 point coplanar track mask design with designed tracks of multiple widths from 100μm to 10μm. Asymmetry crosses were placed in the corners of the sample to assist in mask alignment.

(c) Image showing mask of a single IJJ transmission line. The gold coated contact pads are highlighted in red and the central line is highlighted in blue. The black regions either side of central line are ground contact pads and are connected to ground through gold bonds made to the gold coated region of the ground contact (shown in yellow).

FIGURE 4.1: Mask designs created using Inkscape drawing software and printed by JD Photo Tools. The black regions show where Tl2212 is left on the substrate following argon milling.

deposited on the ground planes to aid contact to the superconducting vicinal TBCCO surface (Figure 4.1(c)). It was not necessary for the gold to be evaporated to the edge of the superconducting ground plane, and so was designed to leave space surrounding the track to avoid shorting the device. The gaps between the tracks and the ground planes were calculated to be 50Ω, consistent with the rf design of the measurement setup. At the end of the tracks were Au coated contact pads with a tapered designed to reduce rf discontinuities that may produce reflective rf elements, but also gradually increase the size of each track up to 300μm to produce a reasonable sized pad to be targeted with the Au wire wedge bonder. It should be noted that as the width of the main track is reduced, the likelihood of shorting between the central track and ground planes increases. Due to the large aspect ratio with the track length of 3.5mm and widths as small as 10μm, photolithography techniques become increasingly sensitive to error due to the long length; the gap width for the 10μm wide central track is 19μm to achieve 50Ω line impedance to ground.

The following describes the process of photolithography used for the samples in this work, based on techniques developed by Dr Saleem. The sample is first pre-baked at 110^0C for 1 minute, following which S1818 positive photoresist is immediately spin coated onto the sample surface using a Specialty Coating Systems G3P Spinner, at 4000 rpm for 30 seconds with a 500 rpm ramp up for 2 seconds. The coated sample is again baked at 110^0C for 1 minute, then exposed to UV light using a Karl Suss MJB 3 mask aligner and the desired chrome mask. First, an edge bead removal exposure is done, removing the edge bead formed by the square sample shape and corners during the spinning process. This ensures better contact between the mask and the sample and creates a more accurate transfer of the design to the photoresist for future stages. The edge bead exposure was then exposed for 20 seconds, developed in Microposit MF-26A for 60 seconds, soaked in DI water for 30 seconds and dried using pressurised nitrogen gas. After the edge bead removal, the selected pattern was aligned and the photoresist exposed for 3 seconds (Image 1 in Figure 4.2). The sample was then placed in Microposit MF-26A for 15 seconds, and then rinsed for 30 seconds in DI water and dried with nitrogen gas (Image 2 in Figure 4.2). Once developed, the sample was hard baked on a hot plate for 1 minute at 110^0C to improve the resilience of the photoresist prior to the milling stage of the process.

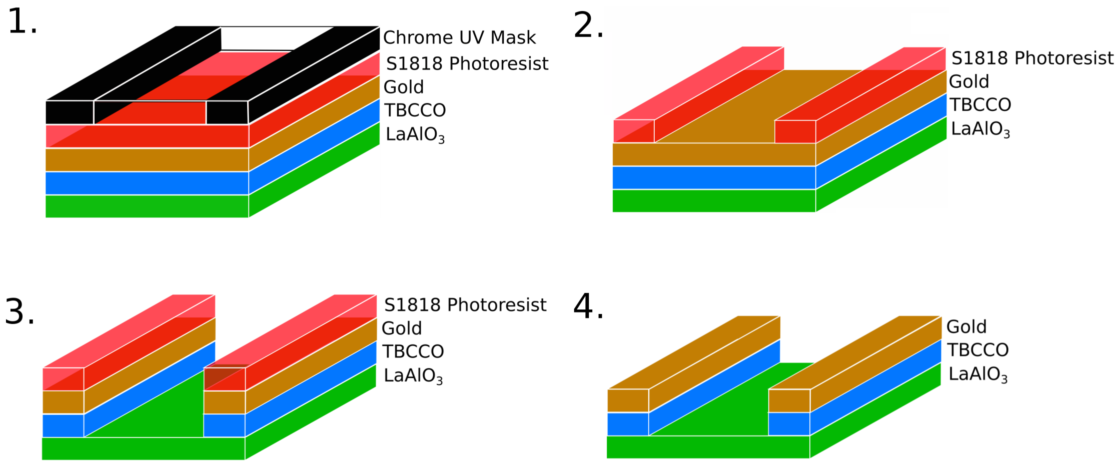

FIGURE 4.2: Stages of Photolithography. 1. S1818 positive photoresist is spun onto the sample. The sample is aligned and exposed to UV light 2. The exposed areas are then developed leaving the mask pattern in photoresist 3. Argon ions are then used to mill away the excess material surrounding the pattern, with the photoresist shielding the pattern from the incoming ions 4. Photoresist is removed leaving the pattern in the TBCCO

Following the milling stage, a further photolithography stage is needed for the contact pads pattern to be transferred. Unlike with regular c-axis samples, the thin film surface could not be coated in gold prior to patterning as this would provide a short circuit pathway across the superconducting planes within the material due to the misalignment of the intrinsic layering. In order to use the same positive photoresist, an inverted photomask was used to produce the contact pads. Once the mask was aligned, this left the desired pad regions uncovered, and the rest of the Tl2212 pattern protected by the S1818 photoresist. The sample was then placed in an Edwards E306 Belljar thermal evaporator, and a 300nm gold layer was evaporated onto the sample. The photoresist was then removed following the previously outlined procedure, leaving the gold contact pads on the patterned Tl2212. Gold thicknesses of less than 300nm were attempted on multiple samples, however due to the surface roughness of the vicinal film, poor adhesion of these thinner layers of gold meant that it wasn't possible to make contact to the pads.

4.1.3 Argon milling

Following photolithography and the transfer of the mask design to the S1818 layer atop the Tl2212 thin film, argon ions were used to mill away the undesired regions of superconductor. A Scientific Vacuum Systems SVS6000 argon ion miller was used to excite and accelerate a beam of ion atoms towards the sample, milling the unprotected superconductor, leaving the desired pattern shielded by the photoresist on top of the substrate (Image 3 in Figure 4.2).

The beam parameters for the argon mill were as follows: a beam current of 20mA, beam voltage of 500V, acceleration voltage of 260V, gas flow of 5 SCCM and base chamber vacuum of approximately 1x10^{-6} mBar. The sample is rotated during the mill at 20 rpm to maintain a uniform mill rate across the sample. Control of the milling stage is primarily visual, as different mill times are required for each sample due to variation in the film thicknesses and the quality of the filament used in the system. The times for milling varied between 45 and 80 minutes. Once milled, the substrate becomes transparent with the Tl2212 pattern on the surface. Some samples, upon visual inspection appeared transparent as if milled sufficiently, however under microscope inspection, the milling was incomplete. It was necessary to leave the samples in longer than required in order to ensure the superconductor is completely milled through to avoid any short circuiting and/or having to perform the argon milling in multiple stages. One method that was adopted to assist in monitoring whether the milling was completed was putting a mark with a permanent pen on the back of the substrate that becomes visible once the Tl2212 has been milled through.

Once the milling is completed, the sample is soaked in acetone for 30 minutes to remove the remaining photoresist from the top of the pattern, and then rinsed in isopropanol, leaving only the desired pattern of superconductor on substrate, ready for measurement or further device fabrication using the FIB (Image 4 in Figure 4.2). Figure 4.3 shows a top down SEM image of a completed 10μm wide coplanar Josephson transmission line with the central line in the middle of the image, and the two coplanar ground planes either side separated by air and darker substrate below. The topological surface of the vicinal material is very rough in comparison with c-axis films. We can see the plate-like surface in the direction of the misalignment where the layering of the material forms a step-edge structure, as shown in the insert in Figure 4.3. It is also possible to see some material defects and cross plane shorts in the SEM image, in some cases defects of up to 5μm in length that could affect the number of IJJs in a finished device.

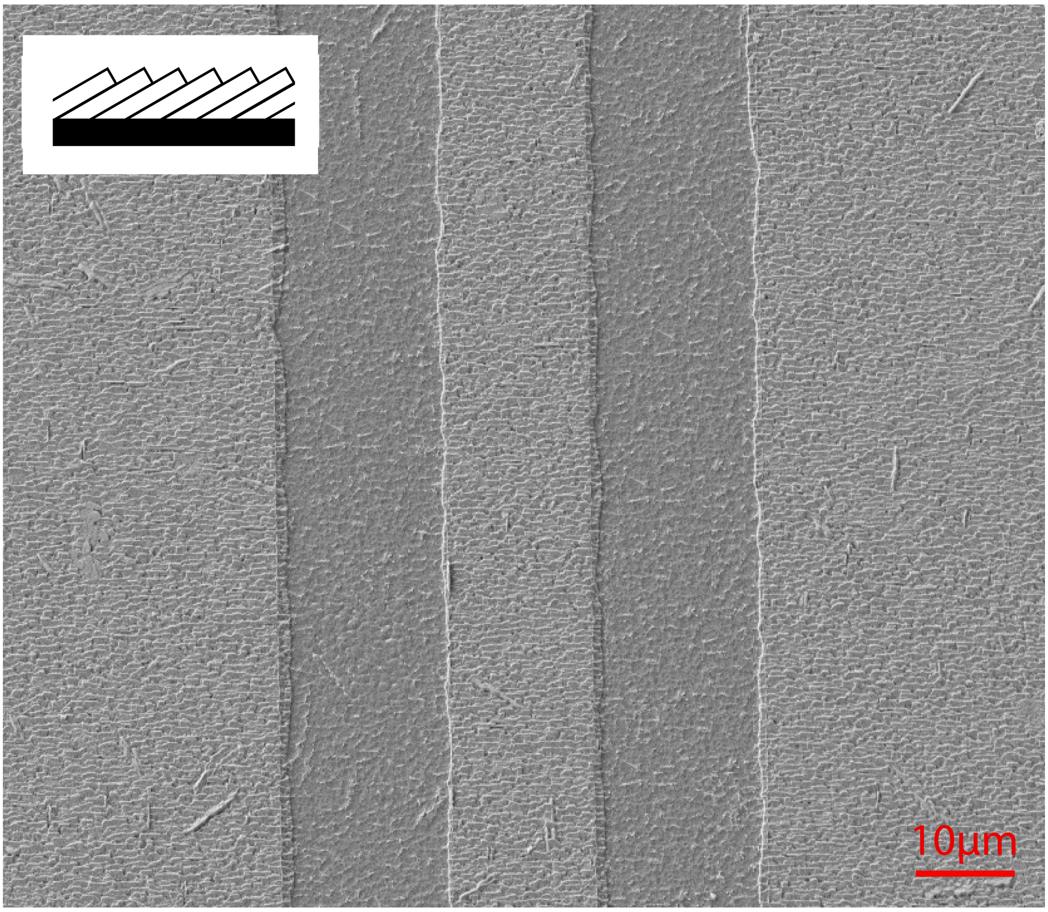

FIGURE 4.3: SEM image of a section of completed 10μm wide vicinal Josephson transmission line

4.1.4 Focused ion beam Milling

The Zeiss focused ion beam (FIB) system creates, focuses and accelerates a beam of high-energy gallium ions for high resolution milling of nanometre scale features. Using a FIB allows for milling of defined areas without the multiple wet chemical stages associated with other lithographic processes, such as electron beam lithography, but is limited to far smaller regions than those achievable through photolithography. The system has a stage with 5 axes of movement which allows for milling at a wide range of angles, which can allow for lateral cuts for c-axis device fabrication.

The Zeiss Crossbeam XB1540 system consists of 2 coincident beams offset by 54^0; a Zeiss 'Gemini' scanning electron microscope (SEM) and an Orsay Physics Canion 31 gallium focused ion beam (FIB) (Figure 4.4). This arrangement enables simultaneous high resolution imaging with the SEM down to nm-scale, alongside the milling and fabrication capabilities of the FIB.

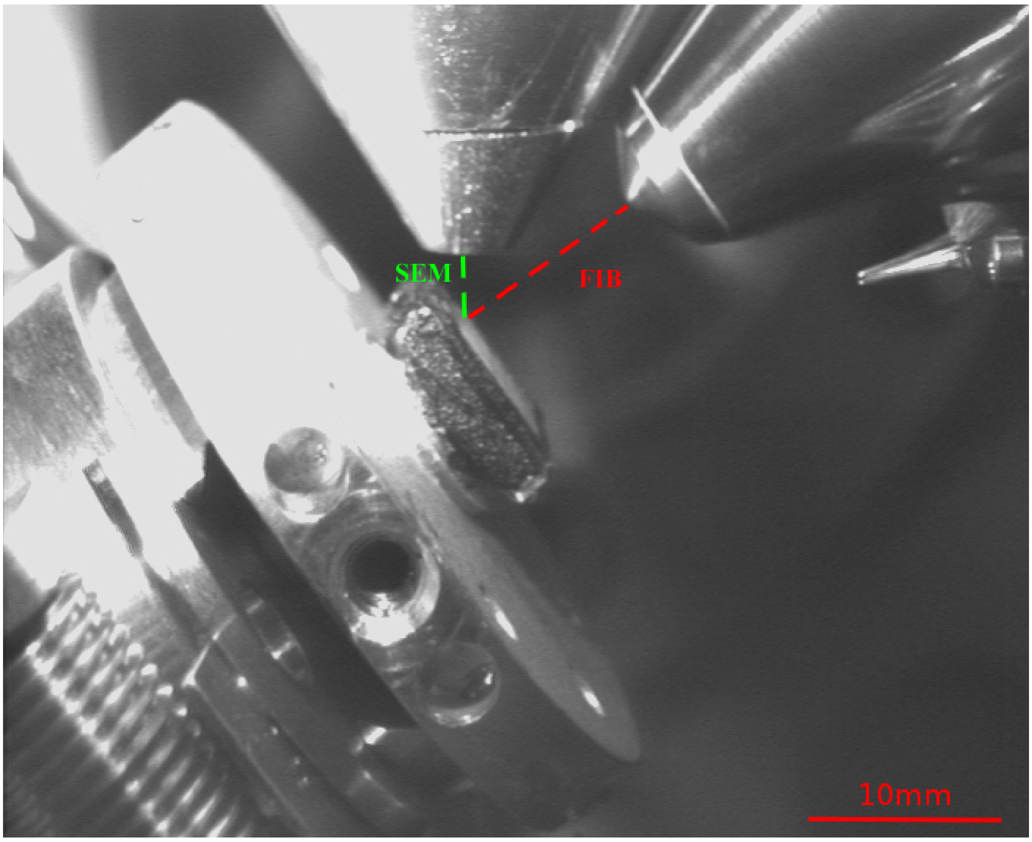

FIGURE 4.4: Zeiss Crossbeam XB1540 FIB chamber image showing a sample aligned at the coincident point of the gallium FIB and SEM, allowing simultaneous milling and imaging.

Before milling, samples are mounted onto a stage stub using conducting carbon tape, and the surface pads are grounded using carbon tape to reduce unwanted charging effects when imaging and milling. If ungrounded and the material to be milled is on an insulating substrate, the charging effect can cause significant distortion to the image as the imaging electrons and ions are strongly deflected from the surface. If necessary, a better contact can be made using electrodag silver paint, however this requires solvent cleaning for removal which can result in damage to small scale devices.

The beam current was varied depending on the size of the mill area, from 2nA for the larger regions in excess of 50μm^2, down to 100pA for mills of less than 1μm^2, with a constant beam voltage of 30kV. By setting the current and defining the area of the mill, the software calculates the time necessary to mill based upon the dosage required, or can be set to mill for a defined time. By using the crossbeam SEM to visually monitor when the mill had completed, it was calculated that it required a beam dosage of 2.2nC/μm^2 to completely mill through a 600nm thick Tl2212 film and reach the substrate. To account for thickness variation between samples, the mill dosage was increased by 10% to ensure mill completion.

Whilst milling, the FIB system can suffer from drift caused by sample charging or mechanical stage drift. For mills of smaller dimensions, this can be negligible and have no apparent effect, however larger mills can be affected by poor edge definition, extended mill time and local damage and ion implantation in regions not needing milling. Mechanical stage drift can be caused system hysteresis when adjusting the stage position, but the effect can be reduced by leaving time for the equipment to settle after sample alignment before proceeding with the milling stage. Careful mill design can also be used to reduce the amount of area necessary to remove and time required milling, lessening the significance of any drifting effect. As mentioned previously, the sample charging issue for both FIB and SEM can be reduced through proper grounding of the sample, however using electrodag silver paint can leave particulate residue on a sample which can cause further charging issues or damage to nanometer scale devices if not properly cleaned using solvent washes.

4.1.5 Measurement Dip Probe

Low temperature electrical measurements were made using a custom built helium dip probe (HDP) that was lowered into a dewar of liquid helium for characterisation down to 4.2 Kelvin. The probe was designed and constructed by Dr. Asan Kuzhakhmetov. The probe consists of a magnetically shielded sample holder that sits at the bottom of a shaft, up which the connecting wires travel from the sample holder to the BNC connectors at the head of the probe to allow for connections to biasing devices. Using the array of biasing wires travelling down to the base of the probe, it is possible to perform electrical DC measurements across multiple devices during the same cool down. The system allows for flexibility in biasing configurations and types of measurements to be performed including resistance as a function of temperature, R(T), microwave transport and current-voltage (IV) characteristics.

The probe consists of a magnetically shielded sample holder that sits at the bottom of a pole, and wires that travel from the holder to the array of room temperature BNC connectors at the top of the probe which allow for biasing of multiple devices simultaneously. By changing the height of the probe within the dewar, it is possible to control the temperature of the sample whilst performing electrical characterisation, which allows for R(T) measurements using the Lake Shore Ltd. Cernox temperature sensor[5].

Samples were mounted on custom detachable holders that allow for easily insertion and removal from the probe, and for bonding to be made without damaging the probe. The sample holder was then inserted into the matching socket at the end of the probe and covered with a mu-metal shield to isolate the sample from stray fields. The probe was then inserted into the neck of the dewar and attached, following which the probe was lowered into the liquid helium.

The 1cm^2 samples were mounted using electrodag silver paint on a 12mm x 12mm x 2mm copper spacer to prevent the sample breaking when being transferred from FIB

---

[5] https://www.lakeshore.com/products/cryogenic-temperature-sensors/cernox/models/pages/overview.aspx

fabrication to measurement system mountings, yet still allow for thermal and electrical conduction. This was then placed upon the measurement holder for four point measurements as shown in Figure 4.5. The 5cm^2 samples were fixed to the microwave sample holder using a resin glue.

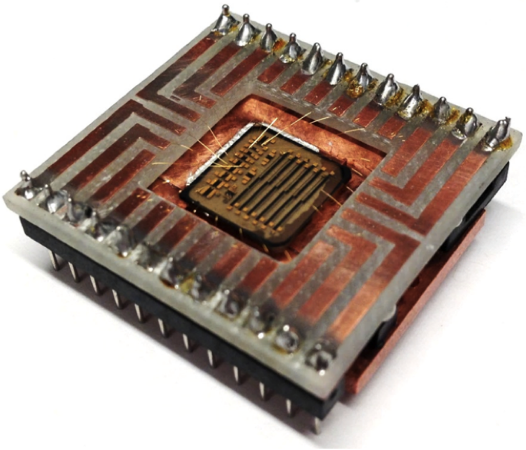

FIGURE 4.5: PCB and copper helium dip probe holder with sample wired up using a gold wirebonder. The sample size is 1cm^2

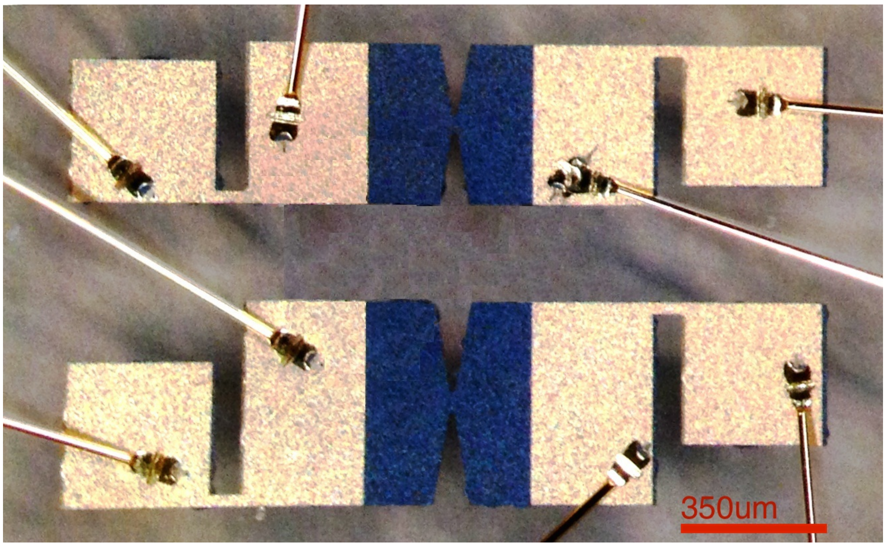

FIGURE 4.6: Optical microscope image of wired up test devices. The dark region is the uncovered vicinal TBCCO, and the light regions are the gold covered contact regions

The gold contact wires seen in Figures 4.5 and 4.6 are connecting the pads of the devices to be measured to the copper tracks on the dip probe holder. These are made using a KS 4573 Au Wedge bonder. Following the photolithography and before measuring devices, it is first necessary to check the connections on the sample. This is to identify any open

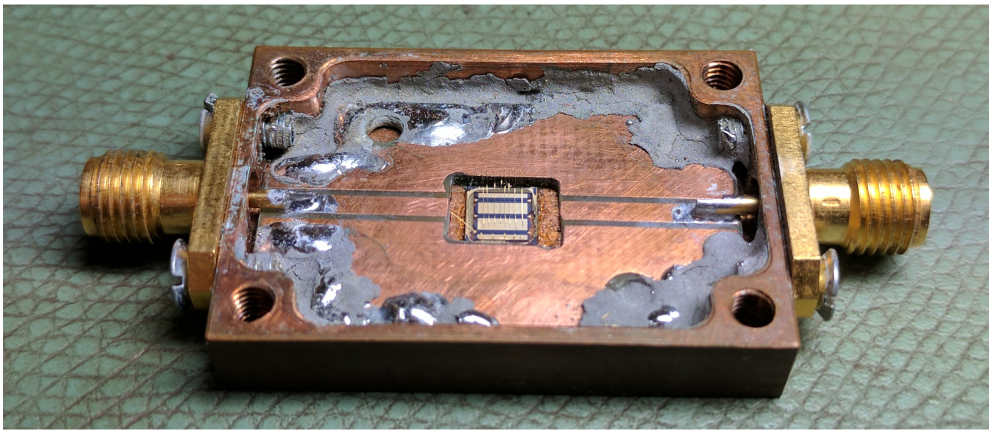

FIGURE 4.7: Photo of rf measurement sample holder with gold SMA rf connectors for input and output connections to the device. When measurements are being made, the top of the sample holder is sealed with a copper plate

circuits in the contact tracks, and to establish whether devices are able to be measured in 4, 3 or 2 point contact arrangements.

Figure 4.7 shows an image of the custom copper rf holder used for cryogenic measurements with liquid helium and the HDP. The sample holders were designed by Dr. Jonathan Burnett to provide standard 50Ω impedance to ground to be consistent with the rf measurement setup and reduce any reflective impedance discontinuities. Figure 4.8 shows a zoom of the wired rf device connected to the holder, the key features of which are false coloured in the image; wire bonds in red between the copper ground plate and gold coated superconducting ground plates on the sample, copper input and output connection tracks in green wired to the device by the single red wire bonds, and the central transmission line highlighted in blue.

4 point measurements, with 2 current source points and 2 separate voltage measuring points, provides the most accurate electrical characterisation of a device. By using the separate points for current and voltage, any contribution to the measurement from contact resistance is eliminated. With open circuits from imperfect sample fabrication, it was sometimes only possible to measure 2 or 3 point measurements, which include an additional contact resistance superimposed upon the characteristics of the device. This will be highlighted in the results where necessary. To current bias the sample, a Keithley

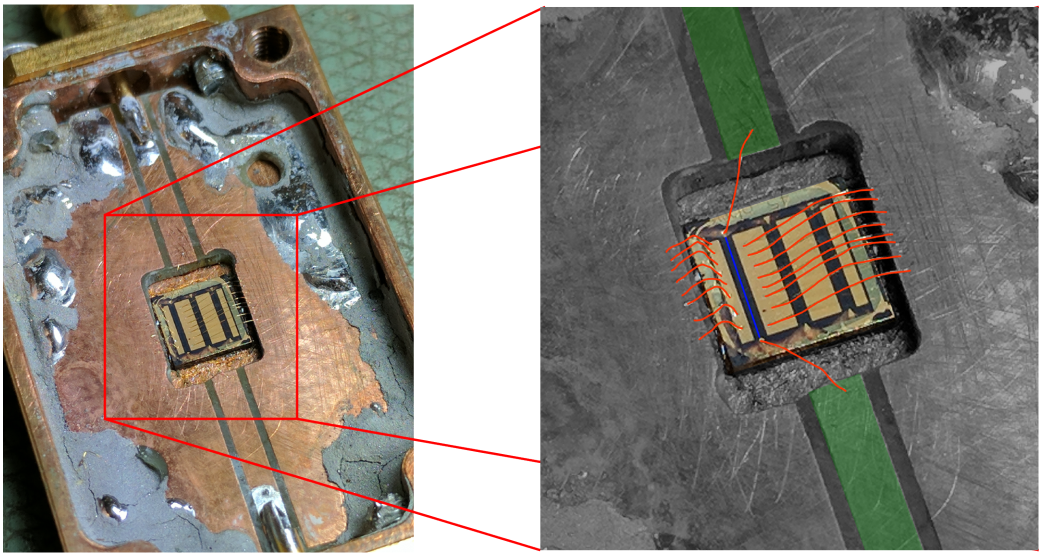

Figure 4.8: Zoom image of a wired Josephson transmission line device in the rf measurement holder. The expanded image shows the sample with key features false coloured: wire bonds in red, connection tracks in green, and the central transmission line highlighted in blue. The size of the sample is $5\mathrm{mm}^2$

2400 sourcemeter was used in conjunction with a Keithley multimeter, which allow for GPIB connection to a computer for interfacing with customed designed LabView software for bias control, measurement and recording of results.

When measuring the temperature-dependent resistance in the vicinal tracks, the current was biased through the junctions. This meant that it was difficult to make reliable measurements of the transition as the resistance values above T_c were approximately 10^6 Ω due to the large number of junctions in the length of the track. Because of such a large difference in resistance values before and after the transition, it was impossible to accurately configure the measurement setup to record accurate readings during the transition. This was due to the large change in time constant when sweeping the current for a differential resistance, or saturating the supply when supplying a fixed value. As such, the resistance during the transition was monitored and a qualititive comparison was made with the temperature to establish when the transition was occurring, or the R(T) measurements were made in the ab-plane of the device or contact lines if possible.

2 point microwave measurements were made on samples using the 50Ω coaxial SMA rf ports on the helium dip probe in conjunction with the measurement setup shown in

Figure 4.9. All rf signals were transmitted using 50Ω coaxial cables and SMA connectors, and DC signals using BNC connected coaxial cabling. The input and output connections to the sample and control paths to measurement setup from the PC are shown in Figure 4.9 as green and red respectively. The measurement control was provided by a PC system running custom Labview programs to interface with the GPIB connected devices for biasing and signal control. The system used to generate and monitor the rf properties of the devices was the Rhode and Schwartz ZNB8 Vector Network Analyser (VNA). The ZNB8 VNA allowed for sourcing and monitoring of signals between 9kHz and 8GHz. Although recommended to do so, no calibration was performed for the setup due to a lack of calibration equipment, however the equipment was calibrated when first acquired. It was decided that due to the nature of the phase shifting and pumping measurements being difference not absolute measurements, this wouldn't have a significant impact on the validity of the results. For pumping experiments described in more detail later, the signal output from the VNA was combined with other waveform generator pump signals using an rf mixer. The total rf input signal was combined with, and the output signal separated from the DC bias for the device using a pair of bias tees with the bandwidth from DC to 12GHz, which were then connected to the HDP through the SMA connectors and coaxial cables down the probe to the device under test. The rf cabling travelling down the hollow probe tube to the sample holder were designed with a bandwidth of DC to 40GHz. The bias tees are the limiting factor on the bandwidth of the system, being able to operate up to 12GHz. The DC bias and resistance measurements were made using a Keithley 2400 Current source and multimeter. Due to the temperature variability of the system, the Lakeshore Cernox temperature sensor was also connected through a monitoring GPIB system to be able to monitor the real time temperature at the base of the probe, placed next to the sample holder.

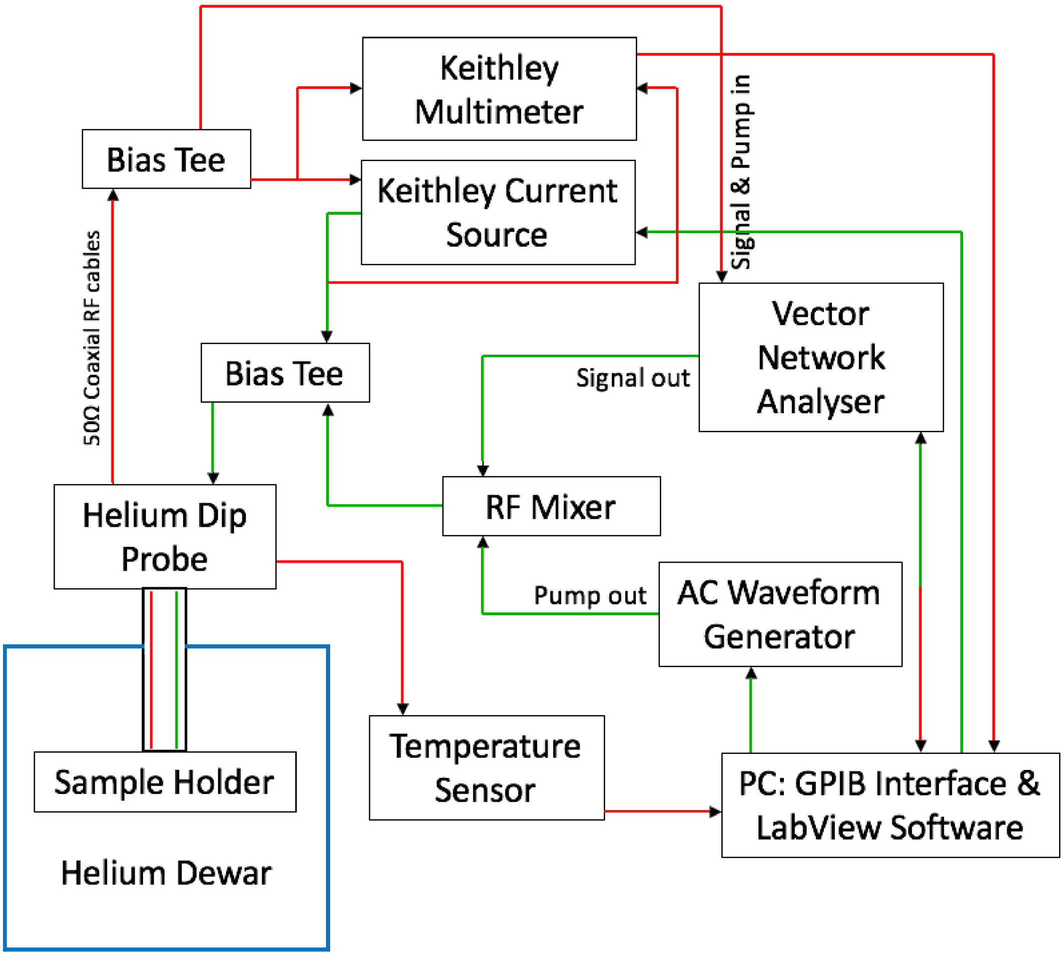

FIGURE 4.9: Microwave measurement setup flow diagram. Connections were made between the equipment using 50Ω coaxial cables with SMA connectors for rf signal and BNC for DC only. Input signal/control paths are shown as green and output/measurement paths are shown in red

Chapter 5

Intrinsic Josephson Microwave Phase Shifter

5.1 Introduction

This chapter presents the results from measurements made on vicinal Tl2212 devices investigating their suitability for use as a superconducting phase shifter. These measurements include testing the device superconductivity, current-voltage characteristics, phase behaviour and the investigation into the use of such devices as parametric amplifiers.

We saw in Chapter 2 that the phase shift of a signal passing through a Josephson junction is dependent on the current-bias as a result of the tunable Josephson inductance. Current-voltage measurements are presented for devices of different widths to determine the track dimensions suitable to achieve Josephson characteritics. The phase shift performance of the devices are then shown and compared with state of the art research from other phase shifters. Finally, the application of the phase shifter and non-linearity of the IJJ tracks is assessed for use as a parametric amplifier, however this area of research will require further work to fully understand and attain gain from such devices.

5.2 Superconductivity Measurement

Following the patterning and preparation of the samples using photolithography and argon milling, it was necessary to confirm that the Tl2212 was superconducting. An in-plane ab track 200μm in width and 3.5mm in length was fabricated using a 300nm Tl2212 film grown on a 0.5mm thick lanthanum aluminium (LAO) substrate. This track was 2-point current biased at 10μA and the DC voltage was measured as the temperature of the sample was reduced from room temperature to 4.2 Kelvin. The results of such a measurement are shown in Figure 5.1, highlighting the transition from 170 to 60 Kelvin, below which the resistance is effectively constant. We see above 120 K the metallic linear dependence of the resistance on temperature, followed by the transition into the superconducting state across a temperature range of 20 K. In this case, due to the two point nature of the measurement, there is a residual 800Ω contact resistance below the T_c of the superconductor.

Although this contact resistance has little bearing on the results of this transition experiment or the behaviour of the superconductor during the transition, it could present an issue for amplification devices by introducing power loss into the system. Another consequence from contact resistance for the phase measurements presented later in this chapter may be reduced sensitivity in the measurement from the biasing and metering equipment due to the increased impedance in the circuit. In an attempt to reduce the value of the contact resistance to the superconductor in the 2 point devices, the Au thermal evaporated contact pads for each device were made to be approximately 300nm in thickness to improve the adhesion to the rough vicinal surface, and where possible, multiple bonds were made to contact pads.

The critical temperature of this sample is 100K, defined as the temperature at which the resistance of the superconductor reaches zero. Previous work found the T_c of unpatterned Tl2212 to be in the range of 100-120K [87] [86]. Differences in transition width between devices and different samples may be attributed to minor changes in the doping and

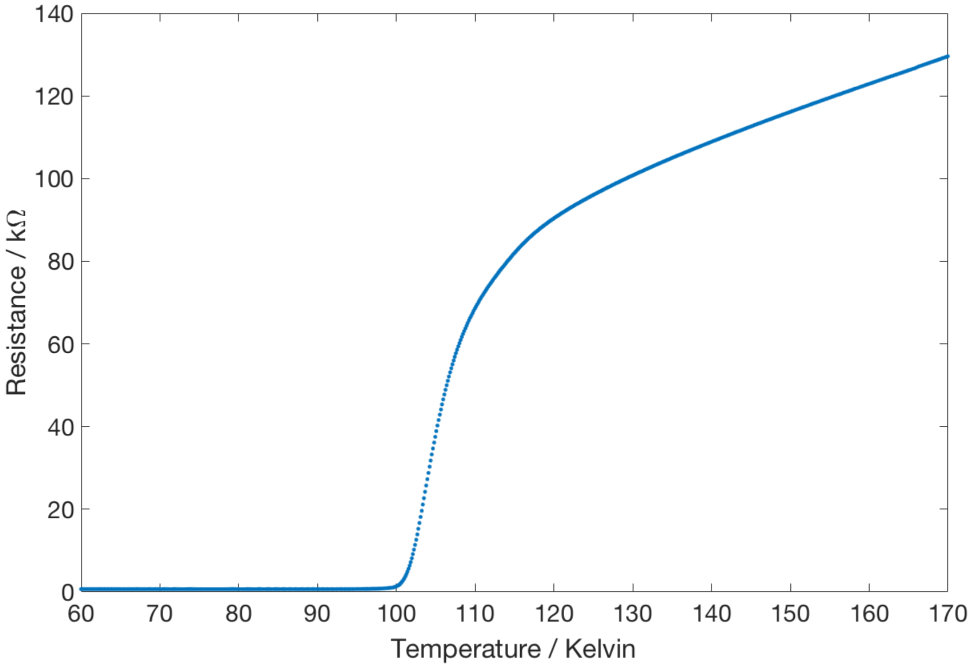

FIGURE 5.1: Resistance as a function of temperature for an in-plane 10μm wide, 300nm thick $Tl_2Ba_2CaCu_2O_8$ vicinal track, DC biased at 10μA. The T_c for the sample is 100 K, defined at the point the resistance of the superconductor reaches zero.

stoichiometry, or impurities introduced during the growth or patterning processes. However, such variations in T_c can be neglected as they have no effect on the current-voltage measurements being made at 4.2 Kelvin, significantly below the T_c of $Tl_2Ba_2CaCu_2O_8$.

The measurements presented in the rest of this chapter were made at 4.2K, the base temperature of liquid helium. This decision was made to operate the devices at a temperature well below the T_c of the material to remove any thermal fluctuation effects from the measurements, and to ensure accurate repeatability of the measurements. Measuring at temperatures higher than 4.2K in a helium dip probe can prove difficult to achieve temperature stability as the temperature varies dramatically over a small distance when raising or lowering the probe in the helium gas above the liquid helium.

Operation of the devices at higher temperatures would be more advantageous and broaden the possible uses for the phase shifter due to lower setup costs and lower cryogenic system complexity. Discussions raised later in the chapter mention the issue of rf heating of the devices resulting in non-ideal behaviour, and measurements made closer to T_c reduce the measurement window and increase the effect of the rf heating. Operating the devices at temperatures closer to T_c also increases the probability of quasiparticle thermal excitation, presenting as increased resistance on the IV characteristics. Another consequence is the broadending of the statistical distribution of I_c and I_r, as explained in Section 2.2.1.2, which could have a significant effect on the repeatability of the phase shifting measurements, as it will be shown later that the majority of the phase shift occurs as I approaches I_c. Once the low temperature characteristics are well established, future high temperature measurements should be investigated.

5.3 Current-Voltage Characteristics

Current-voltage measurements were made on devices of varying widths to investigate the effect on the IV characteristics as the width is reduced. Two-point current bias measurements were made on patterned the $Tl_2Ba_2CaCu_2O_8$ tracks at low temperature. The measurements were made at 4.2K, well below the T_c of the material, using the helium dip probe measurement setup as described in the previous chapter.

Figure 5.2 shows the current-voltage (IV) characteristics for a 200μm-wide microstrip track, fabricated on a 600nm thick 20^o misaligned vicinal sample with the current passing across the cuprate planes in the vicinal direction. The first feature to observe from the data in Figure 5.2 is the lack of a supercurrent branch at 0V, as would be expected when measuring a stack of superconducting intrinsic Josephson junctions. Instead, the data appears linear until approximately 0.2V due to the two-point biasing setup used in this measurement. In this instance, the linear contact resistance seen at low bias is 17.5Ω, which indicates a good contact for the method of wire bonding contact used for this measurement[1].

---

[1] In other cases, the contact resistance can be much higher, owing to the poor contact between the bond and the gold pad, or poor adhesion of the gold to the vicinal surface of the $Tl_2Ba_2CaCu_2O_8$.

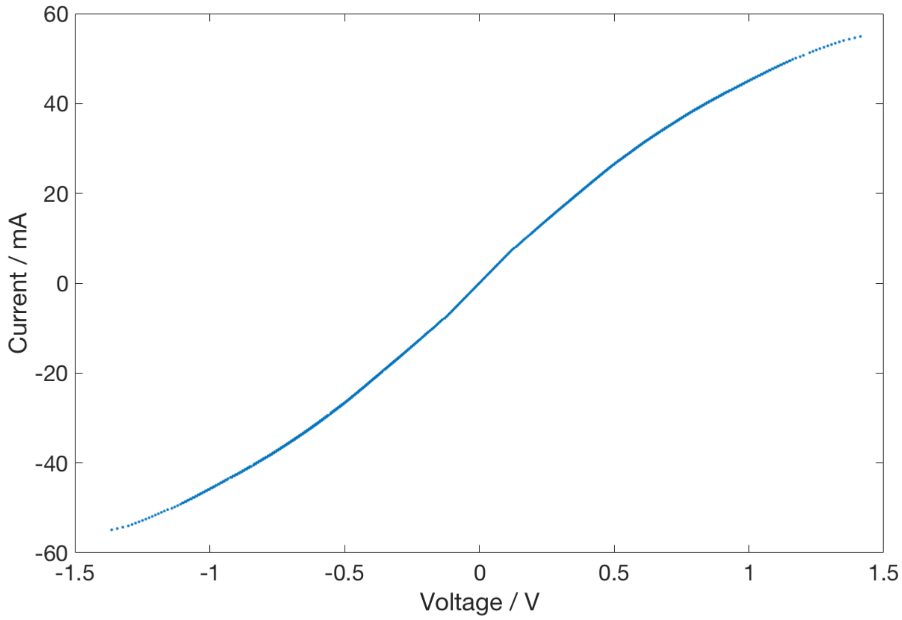

FIGURE 5.2: IV characteristics for a 200μm wide, 600nm thick $Tl_2Ba_2CaCu_2O_8$ track, measured at 4.2K. The switching event at 55mA has not been shown due to the measurement saturating the voltmeter.

In order to obtain the data shown in Figure 5.2, the current is linearly swept up from zero to 60μA, down to -60μA, and back to zero. The discontinuous switching event for the 200μm wide microstrip is not shown on the IV at 55mA, at which point the voltage discontinuously jumps and saturates the voltmeter. The current was then swept back down and the voltage returned from approximately 2V to 1.2V at 50mA, in what is known as retrapping, when all junctions in the normal state return to the superconducting state.

If we remove what is assumed to be entirely linear low bias contact resistance from the data, as shown in Figure 5.3, we see only the behaviour from the IJJ track. Here we observe characteristics corresponding to an overdamped stack of Josephson junctions, with a discontinuity at 7.5mA, beyond which the curve is continuous until the larger jump seen at 55mA. At currents greater than 7.5mA, the differential resistance increases up to 70Ω at the switching event. The lack of hysteresis and characteristics of the IV are very similar to that of data from a Au shunted stack of misaligned IJJs presented by Grib *et al.* [88]. This could indicate that associated with the large width of the stack

(200μm), there is a higher likelihood of cross plane shorts due to material defects and grain boundaries introduced during the growth process.

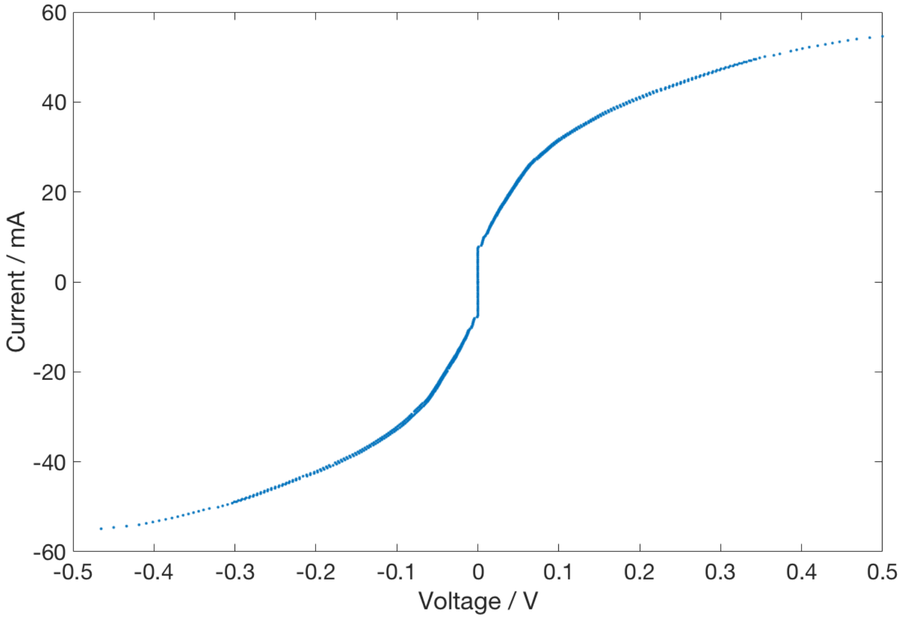

FIGURE 5.3: IV characteristics for a 200μm wide, 600nm thick $Tl_2Ba_2CaCu_2O_8$ track, measured at 4.2K with the 2 point contact resistance removed from the data.

Another cause may be the varying junction dimensions and the associated broad range of critical currents in the large length of track. This effect has also been seen in work by Zhang *et al.* [89] in c-axis films and Zhuo *et al.* [90] in misaligned films. Zhang attributed the increasing resistance on the supercurrent branch to thermal fluctuations and thermally assisted phase slippage, however Zhuo commented that their similar results from long IJJ tracks was more likely due to junctions of smaller sizes with lower critical currents becoming resistive. They stated that because of the large number of junctions in the track, these smaller normal state junctions could sum to produce significant voltages, as seen in the results in Figure 5.3.

The resistance also could be caused by the depinning and flow of flux vortices in the junction, resulting in an increasing DC resistance due to the motion of the vortices within the junctions. However, flux flow is commonly found in the presence of strong applied magnetic fields, which are not present in this case. Although the device was not influenced by any applied magnetic field, it has been found that with large enough currents passing through large dimension Josephson junctions[2], it is possible to insert flux vortices and induce flow within the junctions without external magnetic influence. This behaviour is called self-induced vortex flow [91]. In these previous experiments by Miyhara *et al.*, small channels were created in a superconducting high-T$_c$ track and current biased. The results showed the flux flow voltage whilst the device was still superconducting, as confirmed by a control current line. These characteristics corroborate the data shown in Figure 5.3, whereby we observe a supercurrent to a threshold current, beyond which there is a negative curvature resistance towards a switching event. It is hypothesised that the in-plane component of the DC current passing through the junctions is inducing a magnetic field within the track, coupling to the flux vortices resulting in a Lorentz force and flux motion, and consequently an increased DC resistance.

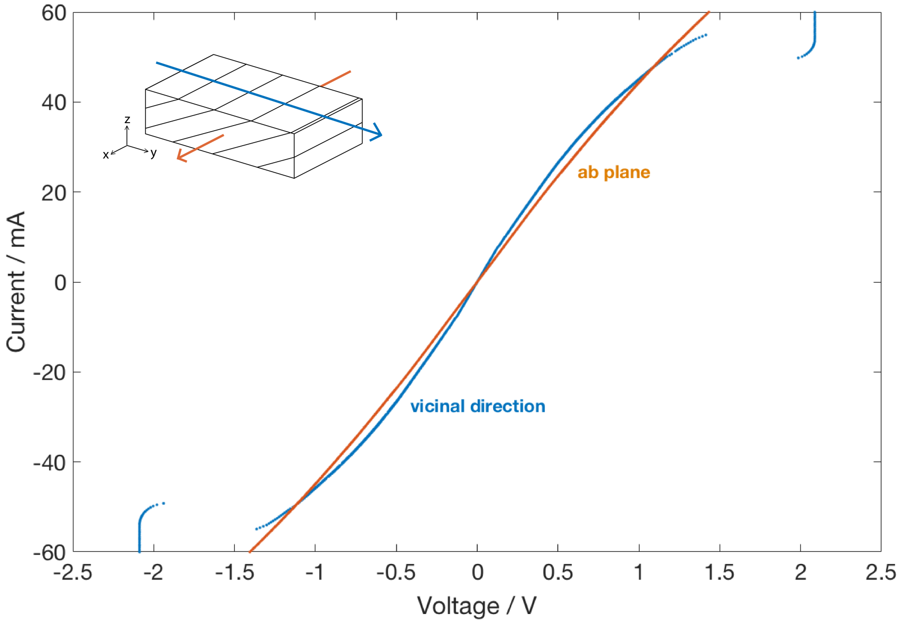

FIGURE 5.4: Comparison between the IV characteristics of the current passed in the in plane and the vicinal directions, measured at 4.2K. The inset image illustrates the direction of current through vicinal layering in the in-plane (orange) and vicinal (blue) directions.

We can see in Figure 5.4 a comparison of the vicinal and in-plane IV characteristics (difference shown illustated in inset diagram), both from 200μm wide microstrips. The

---

[2] Large junctions corresponds to dimensions much larger than the London penetration depth.

two-point contact resistance is comparable between the in-plane and vicinal devices, i.e. 22.3Ω and 17.6Ω respectively. From the data, the two main differences we observe between the two devices are the lack of any switching event and the linear resistance for the in-plane device. Because of the intrinsic anisotropy associated with HTSs, no switching event should be observed for the in-plane device in the same measurement range. For the same current range, there is also no flux-flow curvature seen on the in-plane device as the current bias is at such a small fraction of the critical current density and any insertion current. This difference in characteristics confirms the material anisotropy between the in-plane and c axes expected for a HTS cuprate superconductor.

From observing the detrimental flux-flow like behaviour and no intrinsic Josephson branching in the IV characteristics of the 200μm wide IJJ track, it was predicted that moving to smaller track widths will reduce I_c below the flux insertion current and enable us to fabricate junctions with more predictable behaviour based upon the governing Josephson equations with predictable IJJ characteristics.

To test this hypothesis, a 100μm wide, 6μm long track was fabricated from a 300nm thick Tl2212 thin film using photolithography. This device was then DC biased in a four-point arrangement using the helium dip probe at 4.2K. The results from this measurement can be seen in Figure 5.5. Unlike the measurement of the 200μm wide track in a two-point bias setup, we can see the superconducting branch of the track below 88mA, at which point we see a continuous change to a highly resistive state; above 88mA we observe a significant increase in voltage for a minimal increase in current, with no visible IJJ branching behaviour. The gaps in the data are due to the resolution of the measurement and the highly resistive normal state of the device. Other differences between the smaller tracks and the 200μm wide track are the absence of any switching event and no increase in resistance below the switching current. Zhou *et al*. [90] made comparisons between small and long arrays of IJJs and find a similar difference in behaviour which they attribute to the variation in junction dimensions and not flux flow. However the lack of branching and continuous nature of the IV curves in these results also indicate flux-flow like behaviour as presented by Chana [19] and Gaifullin [92].

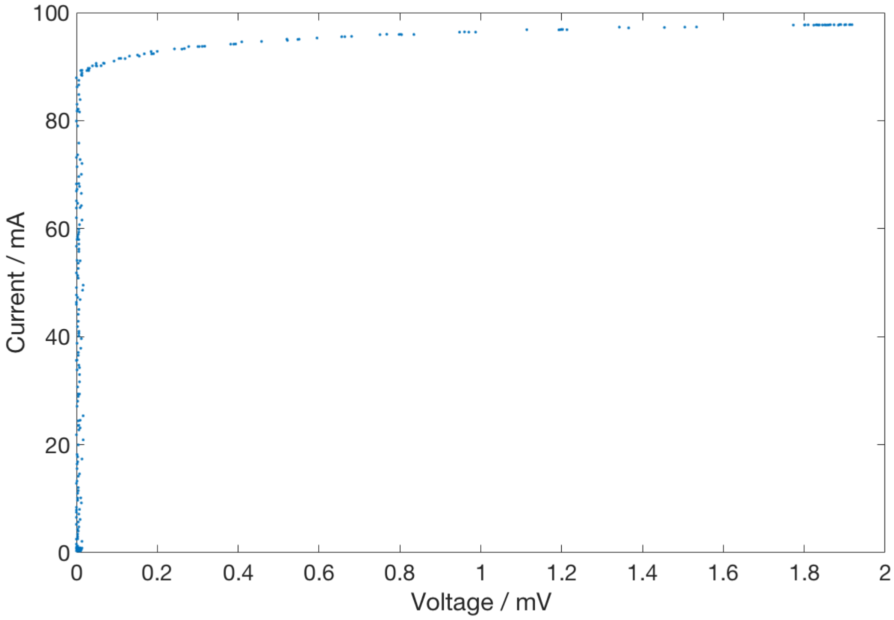

FIGURE 5.5: 4 point IV characteristics for 100μm wide, 300nm thick track measured at 4.2K. The switching current for the stack is 88mA. There is no Josephson branching seen with stacks of this width.

The FIB was then used to reduce the width of the track in stages from 100μm to 1μm, with IV measurements taken at each width. From these measurements, the switching current was extracted (defined as the point at which the voltage exceeds 20μV), and is plotted in Figure 5.6 below. From the data shown in Figure 5.6, we can separate two distinct regions of behaviour: a linear relationship between width and switching current from widths of 35μm and higher, and a non-linear relationship below widths of 10μm. The IV data from the larger width tracks all show the same characteristics as that shown in Figure 5.5: superconducting until a switching current, at which point the track becomes highly resistive with no branching features. If we assume the different behaviour is prodominantly due to self-induced flux flow, we can deduce that the flux insertion/activation current lies between 3.75 and 11 mA, corroborating the current of 7.5mA seen on the 200μm wide track, above which there is a flow voltage.

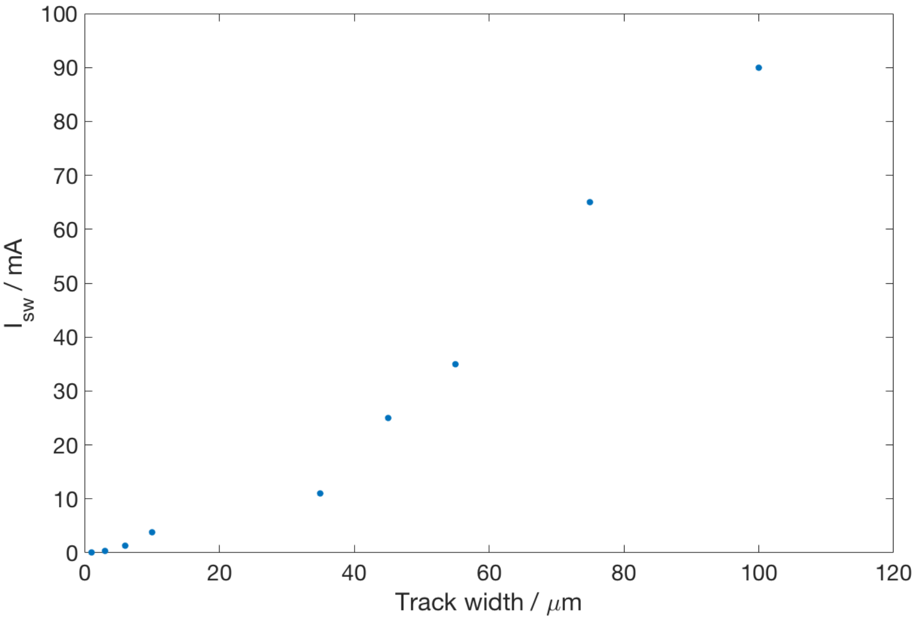

FIGURE 5.6: Switching current, I_{sw} versus track width for tracks from 100μm to 1μm. The same track was milled using Ga FIB to allow for direct comparison of IV characteristics to be made.

After establishing the approximate width threshold for the desired Josephson characteristics using smaller track lengths to allow for FIB fabrication, a longer 10μm wide, 3.5mm long track was fabricated using photolithography to confirm the behaviour was applicable to the larger length. Figure 5.7 shows the the vicinal IV data for the 10μm coplanar IJJ track fabricated on 300nm thick TBCCO film. We observe branching in the vicinal IV data, indicating the dominant Josephson behaviour and confirming the results seen in Figure 5.6. We do see some curvature as the current approaches the switching current of 2.17μA, however this is expected with the range of junction widths within the track containing over 700,000 IJJs.

5.4 Tunable Microwave Phase Shifter

This section of results focuses on using intrinsic Josephson junctions as tunable microwave phase shifters. By varying the DC bias through the IJJ track, it is possible to control the inductance of the junctions, subsequently affecting the phase of the transmitted signal.

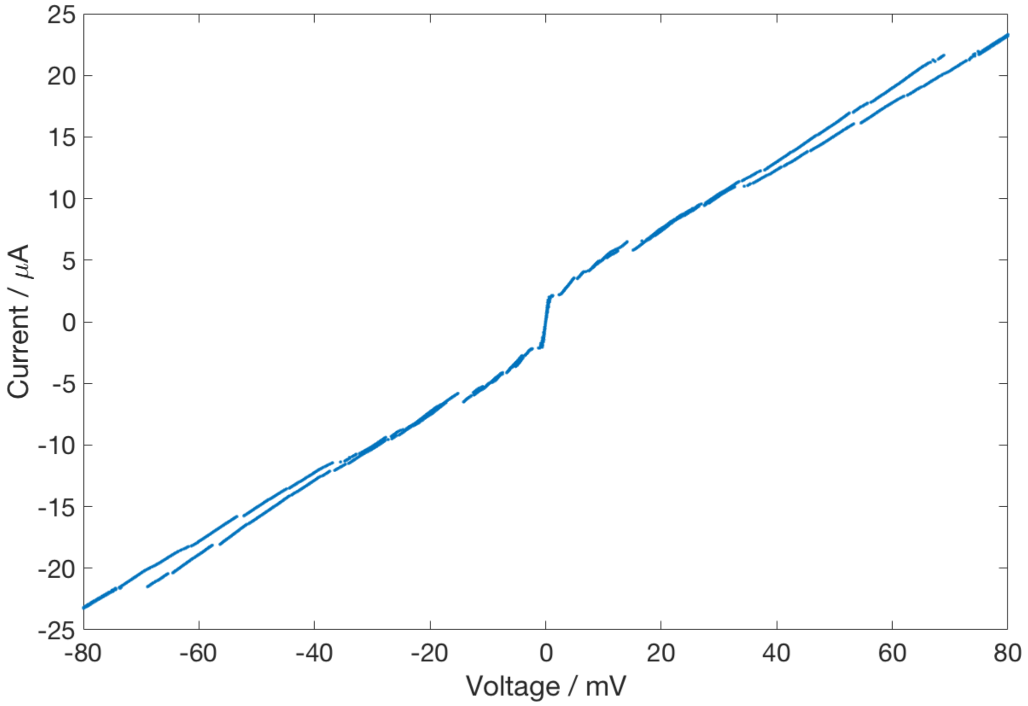

FIGURE 5.7: IV characteristics for a 10μm wide, 300nm thick track of IJJs measured at 4.2K. We can see from the data, as the track width is reduced to 10μm and below, Josephson branching begins to appear in the IV characteristics.

Previous research in this field using cuprate high-Tc superconductors has investigated the use of ferroelectric materials in conjunction with the superconductor to achieve bias controllable inductance and phase variation, however the work presented here aims to achieve the same results with simpler fabrication methods using only vicinal Tl2212 IJJ tracks.

The phase shift of microwave signals as a function of the applied DC bias was measured for Tl2212 tracks of varying widths. Figure 5.8 shows both the signal phase as a function of current alongside the voltage-current data for a 200μm-wide Tl2212 microstrip device measured at 4.2K. The microstrip was DC biased, with a 1GHz RF signal also transmitted through the track. As shown in the previous section, the IV characteristics have had the linear contact resistance removed from the data for clarity.

To obtain the data shown in Figure 5.8, the current was swept up from zero to 60mA, down to -60mA and back to zero. As discussed in the previous section, the device is

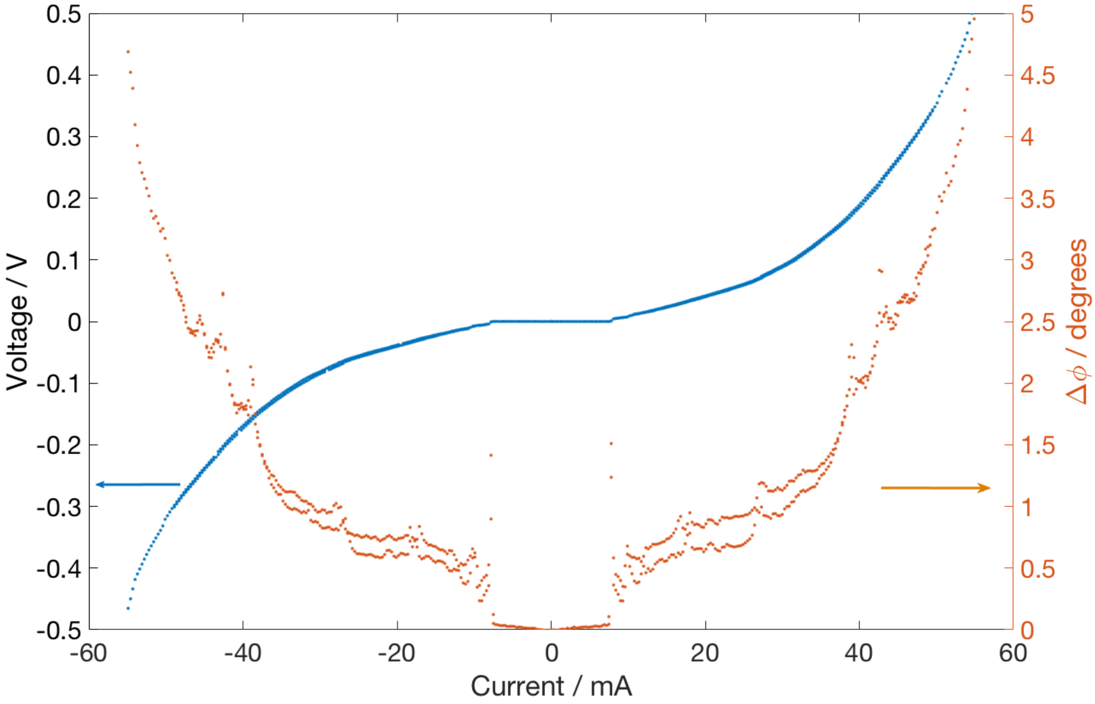

FIGURE 5.8: Phase (orange/right) and voltage (blue/left) against current data from 200μm wide, 600nm thick IJJ track measured at 4.2K. Both datasets are linear until the discontinuity at 7.5mA, at which point the phase data becomes more discontinuous, and the voltage across the track increases towards the switching event at 55mA.

superconducting until 7.5mA, at which point the resistance begins to increase due to self induced flux flow. The discontinuous switching event at 55mA is not shown in the IV data.

When we compare the IV features to the phase behaviour for this device, we can see features in both at the same current. Below the switching event at 7.5mA, the phase variation appears linear until the switching point, where there is a discontinuity in phase. From Equation 2.25 in Section 2.2.1.3, we expect there to be a quadratic variation of the phase with DC bias, however this is not seen with the 200μm-wide microstrip device below 7.5mA. However, looking at the full range of data below the switching event at 55mA, there appears to be an underlying quadratic trend to the signal phase as the current is increased towards I$_c$, indicating an increase in the junction inductance with the bias current, as expected from Equations 2.22 to 2.25 stated in Section 2.2.1.3.

Above 7.5mA, there are discontinuities in phase which could be attributed to collections of junctions being switched to the voltage state and causing a change in the signal. The repeatability of these features both when increasing and decreasing the current bias could further indicate the switching of the junctions as they enter the voltage state with increasing current, and return to being superconducting at the same value when decreasing the current. This behaviour seen in the phase current data shown in Figure 5.8 could be a result of the wide range of junction widths within the track, as discussed previously. The main cause of this is assumed to be the imperfect shadow masking fabrication process creating a track of non-uniform width, resulting in junctions of different dimensions. The variation in junction dimensions may also be due to defects and impurities, such as grain boundaries and voids, and cross plane shorts introduced during the growth stage of the material.

Another explanation for the signal phase dynamics shown could be self-induced flux flow within the junctions. As discussed with regards to the current-voltage characteristics, the 7.5mA discontinuous feature in the signal phase characteristics could be explained as the flux insertion or flow activation current, resulting in the changing phase above this point. These flowing fluxons result in a flow voltage which is visible on the IV characteristics as increasing resistance and movement away from the supercurrent branch. This behaviour is similar to that published by Miyahara [91] and Zhou[90], and points towards the junction track being superconducting, however the flow of the vortices results in a resistance and variance in the phase. The linearity of the phase below the switching event at 7.5mA may be a result of being in the low bias regime, and the predicted quadratic behaviour is interrupted by the flux activation and discontinuities.

Based on the IV measurements made on the tracks of different widths, it was thought that moving to smaller widths may prove advantageous to reducing the effect of width variations on the phase behaviour, and also decrease the effect of flux flow on the measurement. As we moved to smaller widths, the devices were fabricated using a more accurate photolithography mask, resulting in better defined track dimensions. By moving to smaller dimensions, it is also expected that there is to be less introduction of flux vortices into the junction as smaller currents being used remain below the flux insertion and activation currents.

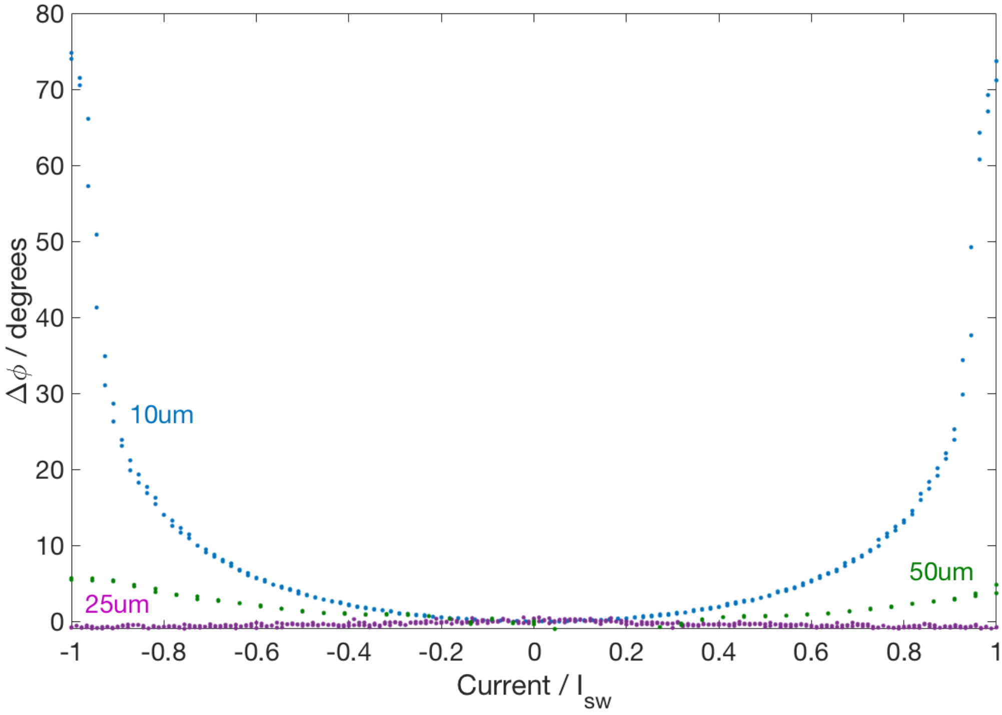

Figure 5.9: Signal phase against bias current for tracks of 3 different widths in 300nm thick TBCCO vicinal films: 50μm in green, 25μm in purple and 10μm in blue, measured at 4.2K. The current scale is normalised to the switching current for each track, and showing only the superconducting region below I_{sw}.

Figure 5.9 shows the data from 3 different coplanar design devices of different widths measured at 4.2K; 50μm in green, 25μm in purple and 10μm in blue. As with the 200μm wide microstrip track, the tracks were DC biased alongside a 1GHz -60dBm RF signal transmitted through the tracks. For comparison, Figure 5.9 shows the current scale normalised to show the variation of the signal phase below the switching current, I_{sw} for all three tracks. Both the 50μm and 25μm wide tracks show little phase change below I_{sw}: 6 and -1 degrees respectively. However, in contrast to this, the 10μm coplanar track shows a distinctly larger phase change of 75 degrees below the switching event seen at 2.17μA, which is also shown alongside the IV data in Figure 5.10. We see the continuous phase variation occurs below the switching event at 2.17μA, and above 2.17μA discontinuities in phase coincide with the switching and retrapping voltages. The other notable feature of the data from the 10μm wide track is the low bias quadratic trend. This quadratic behaviour is also seen in the 50μm wide characteristics, but results in a phase change of only 6 degrees, less than 10% of that seen from the 10μm wide junctions. It is thought that this may be due to a reduced number of equal sized junctions within the stack with the same switching current, I_{sw}. However, based upon the IV results presented in Section 5.3, the main cause is thought to be the presence of flux flow supressing the current path within the junctions and affecting the Josephson inductance, and consequently the phase variability. Measurements of devices with widths below 10μm were attempted, however these devices were not able to be successfully fabricated or measureable due to shorting, material defects and lack of superconductivity. Due to the successful fabrication of the 10μm wide IJJ transmission line phase shifter with quadratic behaviour matching the expected model explained later, this width remained the focus of the investigations and upcoming parametric amplification measurements. Based upon Equation 2.27 in Section 2.3.2, there is no junction width parameter included in the model, so it is expected that going to significantly smaller widths would not result in significantly larger phase shifts, but may improve the fundamental behaviour of the Josephson junctions within the material towards the ideal characteristics usually seen at smaller junction dimensions.

When measuring the IV characteristics of the 10μm wide IJJ transmission line, it was important to consider the signal power being transmitted. Figure 5.11 shows the IV measurements at 1GHz for 4 signal powers; -30dBm in blue, -40dBm in red, -50dBm in green and -60dBm in purple. As the signal power is increased from -60dBm to -30dBm, we see the resistance of the junction track increase from 180Ω to 2kΩ (some of which is the assumed constant contact resistance due to the 2 point nature of the measurement). There is also a suppression of the switching and hysteretic behaviour seen in the -60dBm data at 2.2μA, where the -30dBm data is purely linear. These results seen in the IV characteristics would indicate a suppression of the superconducting behaviour of

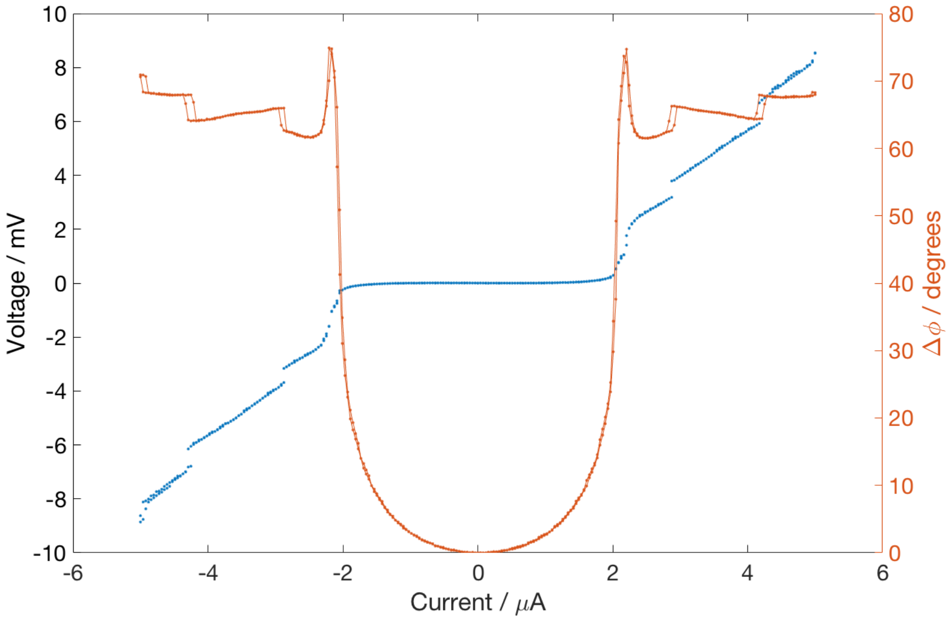

FIGURE 5.10: Phase (orange/right) and voltage (blue/left) against current for the 10μm wide IJJ track measured at 4.2K. The large quadratic phase variation of 75 degrees coincides with the linear superconducting region below 2.16μA seen in the voltage-current data.

transmission line, and is consistent with heating effects at high rf signal powers, driving the material normal and eliminating any Josephson effects. These results show that higher signal powers will be detrimental to the use of such a device as a IJJ transmission line phase shifter which requires the IJJs to be biased in the superconducting regime. Further measurements were therefore made at -60dBm signal power in an attempt to reduce any rf heating of the device which may cause suppression of the signal phase change through the device.

In order to confirm the quadratic low bias behaviour of the 10μm junctions, the change in signal phase was plotted as a function of the square of the bias current, as shown in Figure 5.12. The line in blue shows the linear regression fit to the low bias data regime below $1(\mu\mathrm{A})^2$, above which the results deviate from being linear with respect to current^2. The multiple values of $\Delta\phi$ at each value of current bias is a result of the method used to sweep the current.

Equation 5.1, derived in Section 2.2.1.3, shows us the quadratic relationship of the signal

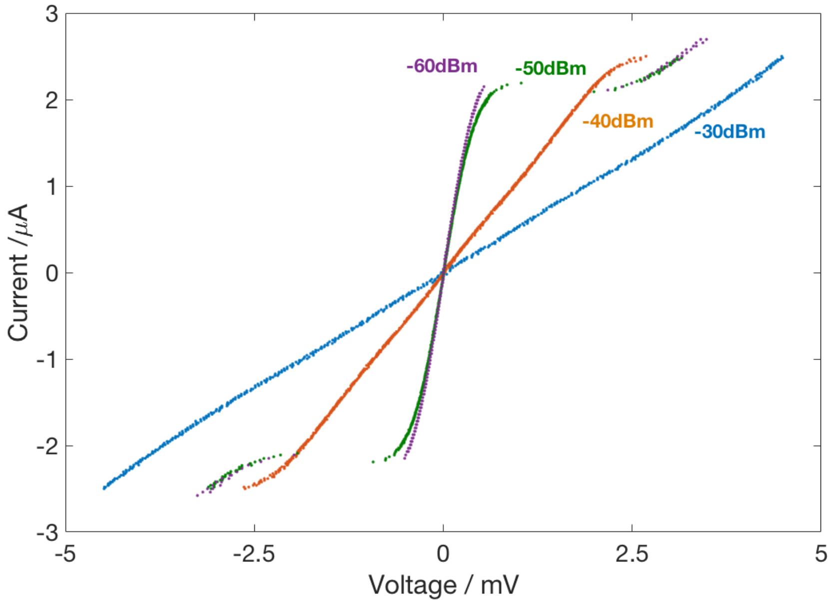

Figure 5.11: IV characteristics with 1GHz signal at 4 different powers; -30dBm in blue, -40dBm in red, -50dBm in green and -60dBm in purple

phase change per junction as a function of the Josephson inductance. This equation is based on the lumped element Josephson junction transmission line model for described in Section 2.2.1.3, whereby each junction can be described by an inductance and capacitance and related to the signal phase change through the junction, $\Delta\phi$. We extrapolate the phase per junction to the total phase change through the transmission line, $\Delta\phi_{total}$, by assuming phase locked uniform behaviour and introducing the term N for the number of junctions in the transmission line. By expanding the binomial term in the square root and taking the first two expansion terms, we obtain a linear relationship between the change in phase and the square of the bias current (Equation 5.2).

$$\Delta\phi_{total} = 2\pi N f\sqrt{L_J C_J} = 2\pi N f\sqrt{C}\sqrt{\frac{\Phi_0}{2\pi I_c}\left(1-\left(\frac{I}{I_c}\right)^2\right)^{-\frac{1}{2}}} \tag{5.1}$$

$$\Delta\phi_{total} = \frac{\pi}{2}Nf\frac{1}{{I_c}^2}\sqrt{\frac{C\Phi_0}{2\pi I_c}}I^2 + 2\pi N f\sqrt{\frac{C\Phi_0}{2\pi I_c}} \tag{5.2}$$

By comparing Equation 5.2 with the linear fit to the low bias data shown in Figure 5.12,

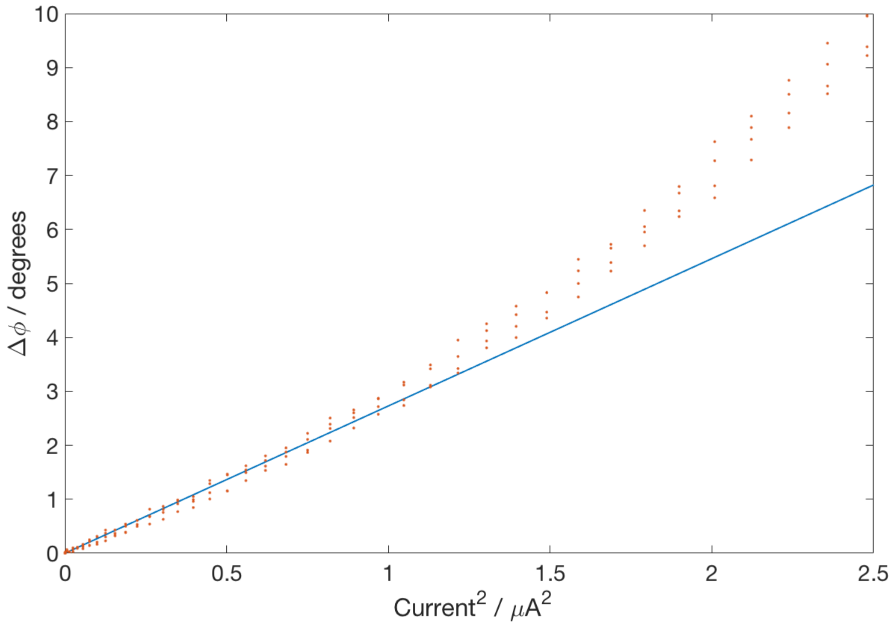

FIGURE 5.12: Change in -60dBm 1GHz signal phase through the IJJ transmission line, $\Delta\phi$, against the bias current squared, I^2 (orange). The linear fit is to the low bias data below $1(\mu A)^2$

we can rearrange Equation 5.2 and extract a value of N = 604,000 junctions, assuming a value of 1aF for the capacitance to ground per junction [3]. Taking this value of N and reinputting it back into the original equation for $\Delta\phi_{total}$ (Equation 5.1), we obtain the full quadratic fit to the full dataset below I_c, as shown in Figure 5.13.

From Figure 5.13, we can see there is very good agreement between the fit from the derived Equation 5.1 and the experimental data. The simulation predicts a phase shift of over 140 degrees as I increases above $0.98I_c$, but this value is not seen in the data. An explanation for why this value is not reached may be due to the variation of I_c at temperatures above 0K, where I_c is more accurately referred to as I_{sw}, and the actual value is governed by a statistical distribution. This has been discussed in detail by Saleem in his doctoral thesis [18]. As previously shown in the IV data, there may still be some flux flow in the 10μm-wide vicinal track as the current approaches I_{sw}, and it is for this reason that the full phase range may not be achievable. By reducing the width of the

---

[3] Material parameters and track dimensions were entered into online coplanar waveguide calculator to calculate approximate capacitance to ground per junction - http://wcalc.sourceforge.net/cgi-bin/coplanar.cgi

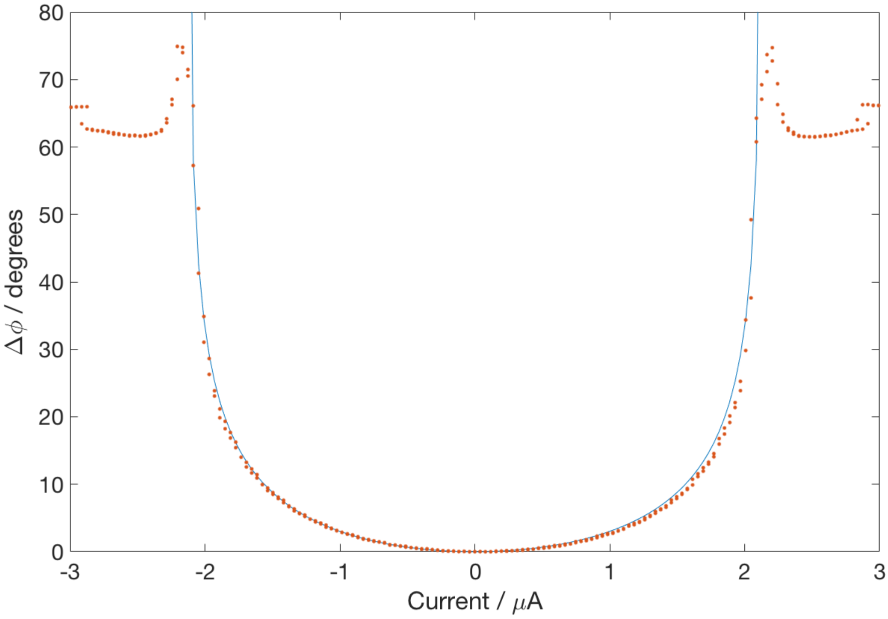

FIGURE 5.13: $\Delta\phi$ as a function of the bias current for the 10μm wide IJJ track, measured at 4.2K. A linear regression fit to the low bias data is shown in blue. We can see that the data begins to deviate from the linear fit above 1μA^2. Multiple data points are seen in for the same current due to the technique used for sweeping the bias current.

IJJ track further, this should eliminate the flux effect and allow for greater phase change to be achieved for the same length of track.

Other signal frequencies were also measured, however the signal at 1GHz received the largest phase shift through the transmission line. Figure 5.14 shows the comparison of the signal phase change, $\Delta\phi$, for -60dBm 1GHz (blue) and 2GHz (orange) signals transmitted through the same 10μm wide IJJ transmission line. From Figure 5.14, we can observe that the phase shift of the 2GHz signal is less than 1GHz, however both display quadratic phase characteristics below I$_{sw}$ for the transmission line. If the IJJ transmission line is governed solely by the ideal Equation 5.2 across all frequencies, there should be the potential for greater signal phase shift as the signal frequency increases, however this does not appear to be supported by the results shown in Figure 5.14. By looking at the S21 transmission data for the IJJ transmission line, I believe it is possible to see why this may not be the case.

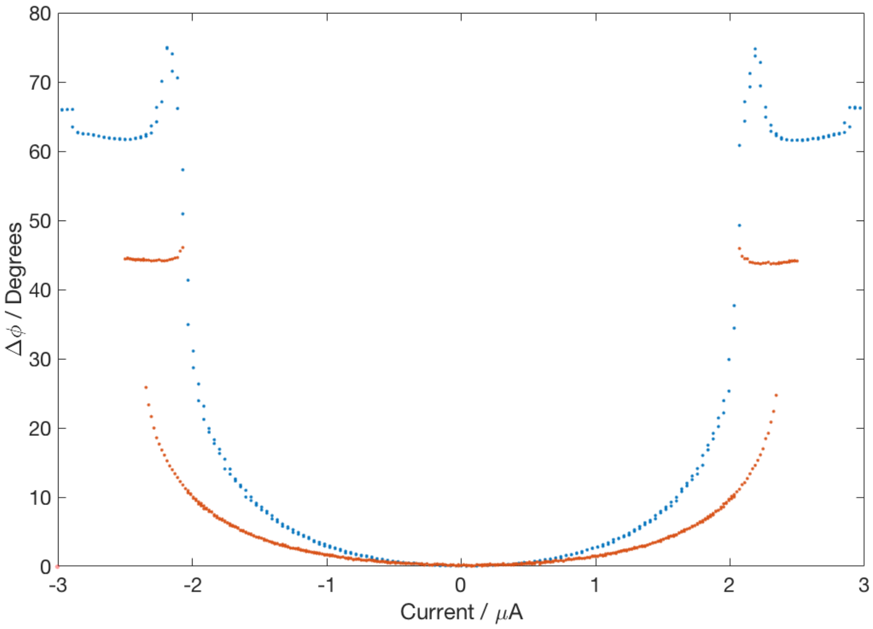

Figure 5.14: Signal phase change, $\Delta\phi$, as a function of bias current for 10μm wide IJJ transmission line measured at 4.2K, with -60dBm 1GHz signal shown in blue and -60dBm 2GHz signal shown in red.

Figure 5.15 shows the S21 transmission results for the 10μm wide IJJ transmission line. We can see that there are a number of resonant features in the S21 transmission characteristics from 2GHz upwards which may be affecting the phase behaviour of the IJJ track. These resonant frequencies are well away from any Josephson frequencies, however they are thought to be a result of geometric resonances from the sample design. By using the long dimension of the track, 3.5mm, in conjunction with the resonant frequencies around 3GHz, produces a phase velocity of approximately 0.06c, where c is the speed of light. This value is in close agreement to that stated by Eom *et al.* of 0.1c [84]. Further sample and holder design will be required to remove these resonances to be able to increase the frequency range of the phase shifting device. By reducing the length of the IJJ transmission line, it may be possible to increase the frequency of any resonances caused by the track length, however this is at the loss of the number of junctions contributing to the phase shift. One way to counter this issue may be to introduce a meander design to the transmission line, which may reduce the number of resonant features in the frequency range under test, and may also allow for a greater density of junctions to be achieved for the sample size restrictions.

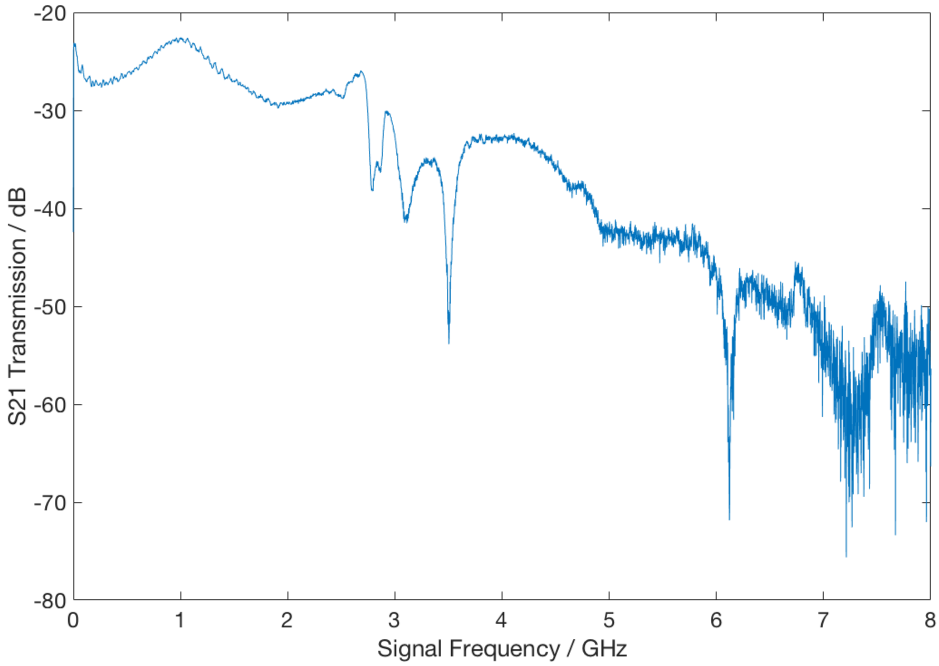

FIGURE 5.15: S21 transmission for 10μm wide IJJ transmission line measured at 4.2K. As the signal frequency increases above 5GHz, there is a dramatic increase in noise of the measurement.

75 degrees of signal phase tunability is comparable or better than that seen from other HTS phase shifters which commonly rely on more complicated biasing circuitry and applied magnetic fields, as discussed earlier in Section 3.2. Normalising the phase change for 3.5mm length of 10μm wide IJJ track to unit length gives a value of approximately 21,430 degrees of phase change per metre, or 119π radians per metre of track length. Jackson *et al.* [79] used YBCO to fabricate a distributed Josephson inductance phase shifter using 1000 SQUIDs, but was only able to achieve 20 degrees of phase change with external field biasing from such a large number of devices. Eom *et al.* [84] exploit the kinetic inductance of a spiral NbTiN coplanar waveguide delay line 0.8m in length and achieve 470 degrees of signal phase variation, or 590 degrees per metre. To achieve the same level of phase variation as Eom *et al.*, a 22mm long IJJ track would be required in comparison to 0.8m, saving a significant amount of space alongside reducing fabrication and design complexity.

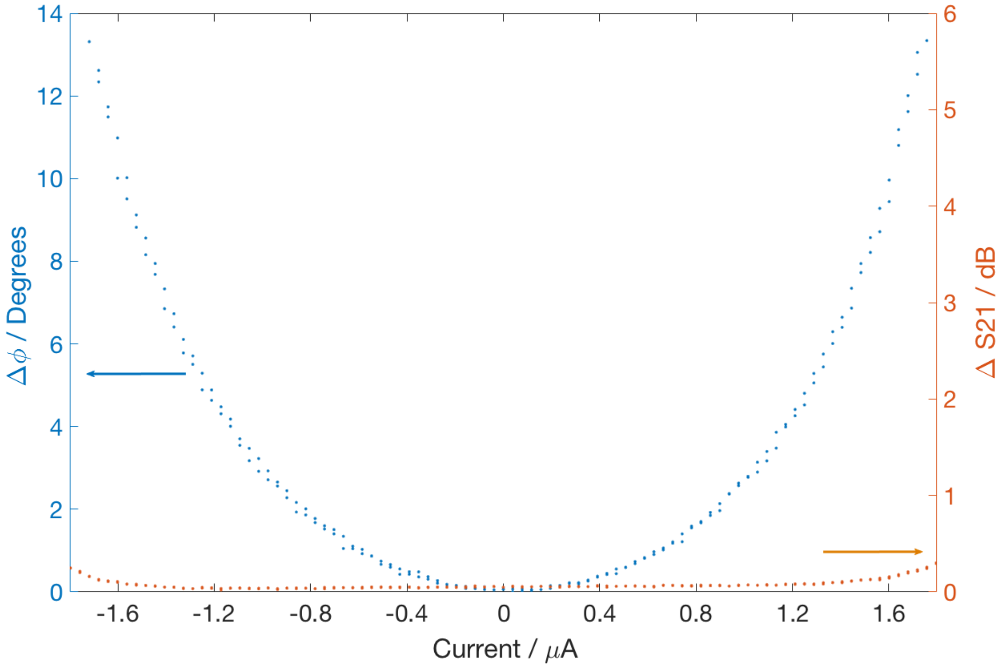

FIGURE 5.16: Change in 1GHz -60dBm signal phase $\Delta\phi$, against the bias current I (blue/left), shown with the change in S21 transmission through the IJJ transmission line (orange/right)

When designing a phase shifter, an important factor to consider is insertion loss. Figure 5.16 shows the phase and transmission against current for the 10μm-wide vicinal track. There is no change in S21 up to $\pm 1.2\mu$A, with a corresponding phase change of just over 4 degrees. It is clear to see from Figure 5.13 that the majority of the phase shift occurs in a small range close to I_{sw}, with little phase change in the low bias regime. This highlights the need to operate the device at temperatures away from the T_c of the material to avoid the statistical broadening of I_{sw} as T tends towards T_c, which would result in inconsistency of I_{sw}. Unlike other devices that previously have reported loss when DC biasing to obtain the phase shift, what we see from the data is a positive increase in S21 transmission as we increase the bias towards I_{sw}. In the data shown in Figure 5.17, we can see an increase of approximately 5 dB from -22.28 to -17.17 dB as the bias current approaches I_{sw}. Comparing the IV data with the S21 transmission, it appears that the reduction of insertion loss of S21 coincides with the IV measurement starting to become non-linear and moving away from being superconducting. Figure 5.18

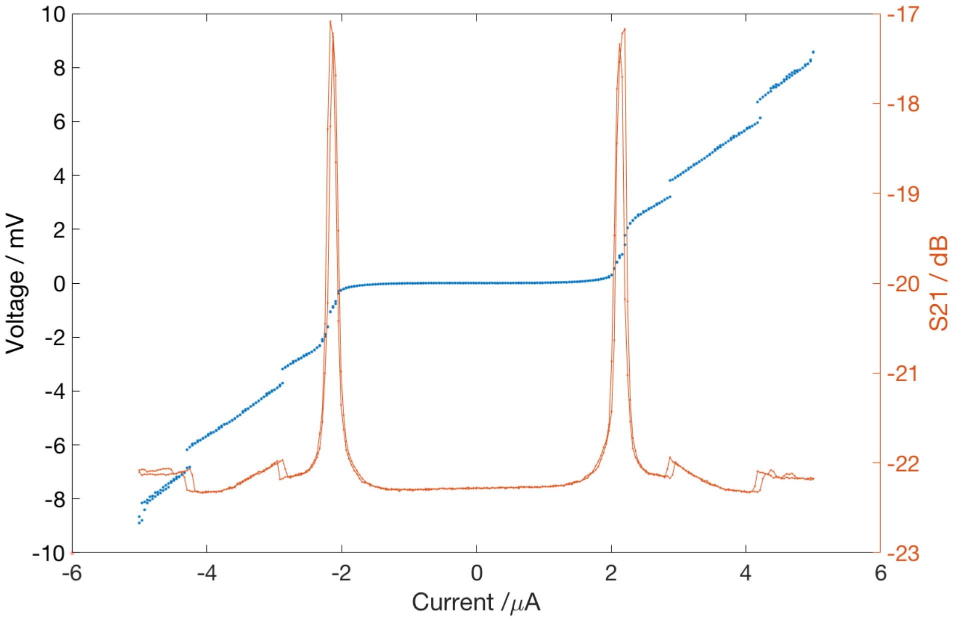

FIGURE 5.17: Voltage (blue/left) and S21 (orange/right) as a function of DC bias current for the 10μm wide IJJ track, measured at 4.2K. The line in the orange data is shown as a guide. There is a large positive increase in S21 as the bias current approaches I_{sw} at 2.16μA.

shows the change in S21 transmission with respect to the phase change, $\Delta\phi$. From the graph, we can see that there is little change in transmission up to 10 degrees of signal phase change, above which we see an increasing quadtratic trend to 75 degrees, at which point the track ceased superconducting. Future work investigating these devices will hopefully be able to extend the region of low S21 variation beyond the 10 degrees shown in Figure 5.18. Comparing these results to those discussed in Section 3.1, there are no phase shift designs without integrated FETs that are able to achieve insertion gain, or a reduction in insertion loss with increasing phase, as seen with this device.

These results show great potential for the use of a vicinal Tl2212 track as a superconducting phase shifter. With the reduction of insertion loss with biasing, and over 20 degrees of phase change per mm length of track, this device could provide a useful balance of phase variation to physical space required in an experimental setup where cryogenic probe space is at a premium.

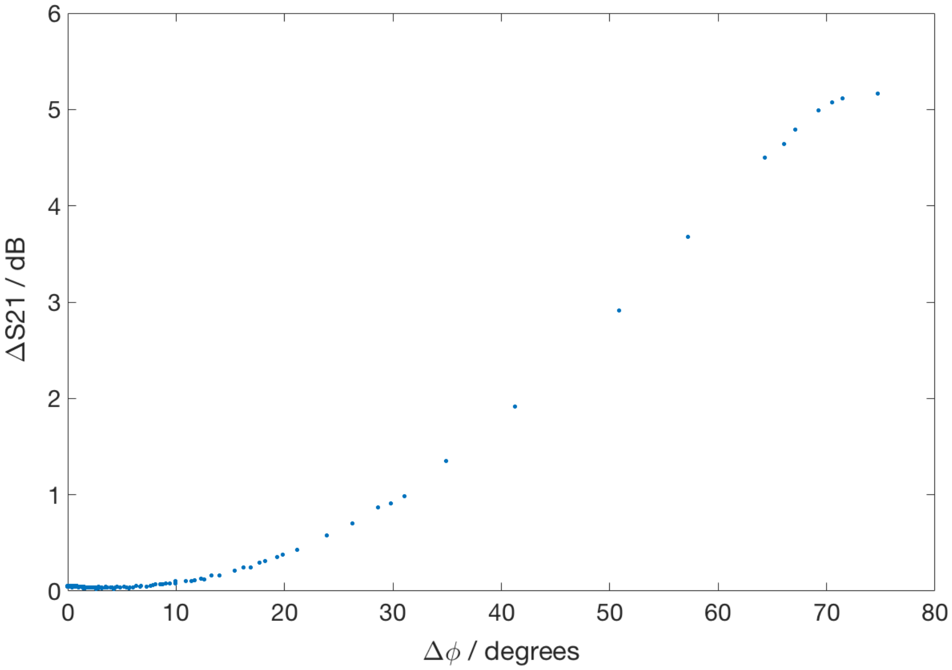

Figure 5.18: ΔS21 as a function of $\Delta\phi$ for the 10μm wide IJJ track, measured at 4.2K.

5.5 Parametric Amplification Measurements

5.5.1 Introduction

Parametric amplification is based on the four wave mixing (FWM) principle that is commonly seen in optics [93], whereby a non-linear material will cause the interaction of multiple input signals and create additional idler signals at frequencies according to the sum and difference of the seperate inputs. Any signal already at the frequencies created by the non-linear interaction will undergo parametric amplification if in phase. When there are only 2 input frequencies, a signal and a pump tone, the non-linear interaction is termed degenerate FWM, as the equations governing the frequency mixing simplify to the following:

$$\omega_{signal} + \omega_{idler} = 2\omega_{pump} \tag{5.3}$$

A travelling wave parametric amplifier (TWPA) was first proposed in 1958 by Cullen [94], whereby a lossless transmission line with distrubuted inductance and capacitance will support an exponentially growing current wave based on the principle of degenerate FWM. Eom *et al.* [84] and White *et al.* [95], based upon the FWM coupled mode equations describing optic systems, went on to further show that in a superconducting (dispersionless) transmission line with $\omega_s \approx \omega_p$, the signal gain G_s is given by:

$$G_s = 1 + (\Delta\phi)^2 \tag{5.4}$$

where $\Delta\phi$ is the phase shift of the pump frequency. This quadratic dependance of the gain on the pump phase shift, and consequently the length of the transmission line, shows the potential application of developing a superconducting phase shifter for use as a TWPA.

O'Brien *et al.* [96] further developed the theoretical principles behind TWPAs by introducing resonant phase matching. Four wave mixing requires no phase matching with a weak pump, however moving to a strong pump tone produces phase mismatch caused by the pump affecting the phase velocities through the materal and limiting the signal gain. By introducing a resonant LC element to the transmission line, they show it is possible to compensate for the strong pump effects. By tuning to frequencies near the resonant feature in the dispersion relationship produced by the LC element, this eliminates the phase mismatch and allows exponential gain to be achieved.

Based on the degenerate FWM principles and the promising phase shift results seen in the previous section, multi-tone pumping measurements were made on the 10μm wide Tl2212 track to investigate any potential parametric amplification produced by the device.

5.5.2 Measurement Results

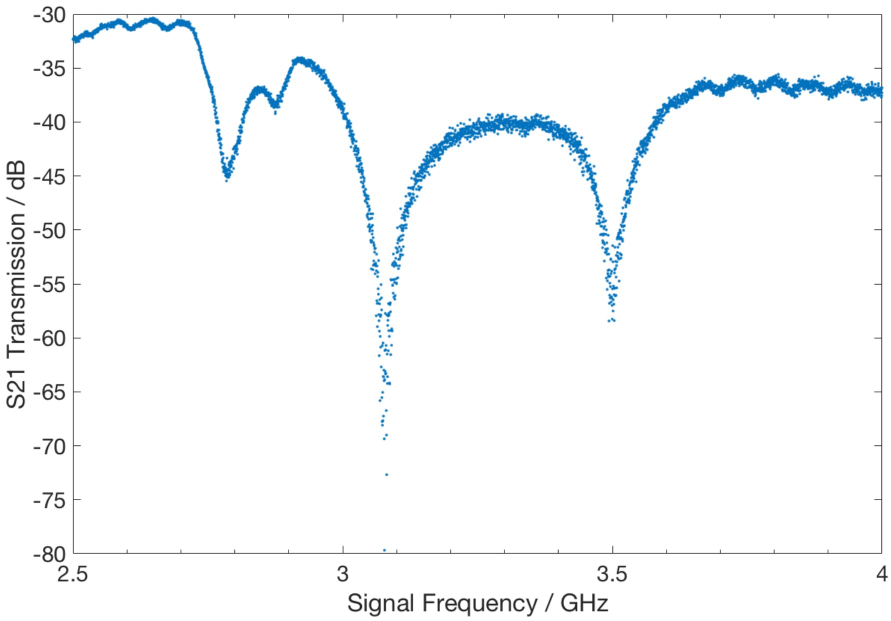

FIGURE 5.19: S21 transmission at frequencies from 2.5 to 4GHz, measured through a 10μm wide vicinal Tl2212 track at 4.2K using the helium dip probe alongside a VNA to source and analyse the signal. There are 3 main resonances in the data at 2.785GHz, 3.077GHz and 3.494GHz.

The 10μm wide, 3.5mm long, 300nm thick, vicinal Tl2212 coplanar track was measured at 4.2K using the helium dip probe and the multi-tone measurement setup, as outlined in Section 4.1.5. Transmission as a function of frequency was measured first, using the

VNA to sweep the signal frequency and monitor the S21 transmission. A result of such a measurement is shown in Figure 5.19.

The graph shows the signal sourced at a power of -40dBm, swept from 2.5GHz to 4GHz, between which are the most notable resonant features in the observable frequency range up to 8GHz, at 2.785GHz, 3.077GHz and 3.494GHz. As stated in Section 5.4, it is thought that these resonant features are a result of a standing wave mode on the long dimension of the track, 3.5mm, which when calculated with the frequencies around 3GHz, produce a phase velocity of approximately 0.06c, where c is the speed of light; a value in close agreement to that stated by Eom *et al.* of 0.1c [84], which they state is due to the large kinetic inductance of the superconductor.

A signal generator was then used to source and sweep a pump frequency tone which was then mixed with the VNA generated signal frequency and transmitted through the coplanar IJJ transmission line. The frequency and power of the pump tone were both varied, in a range from 1 to 4GHz at powers from -70 to -5 dBm. It is important to note that there is no DC bias through the track during the pumping experiments. Figure 5.20 shows the S21 data between 2.5 and 4GHz with a 2GHz -20dBm pump (in orange), superimposed over the data measured with no pump (in blue).

We can see that the pump causes a clear change in the S21 transmission around the resonant peaks, with a region of reduced loss around 3.1GHz where the transmission at 3.077GHz moves from -79dB to -37dB, with the reduction of loss extending from 2.9 to 3.3GHz. It was initially thought that this region of reduced loss, or gain, is directly caused by some interaction between the pump signal and the material in accordance with the FWM effect described earlier in the section. By subtracting the 'no pump' data from the 'pumped' data, we can plot the reduction in loss, or gain, as a result of the pump signal, and is shown in Figure 5.21.

Looking at the data shown in Figure 5.21, we see a sharp lorentzian gain profile centred around 3.077GHz that appears to be solely dependent on the shape of the resonance seen

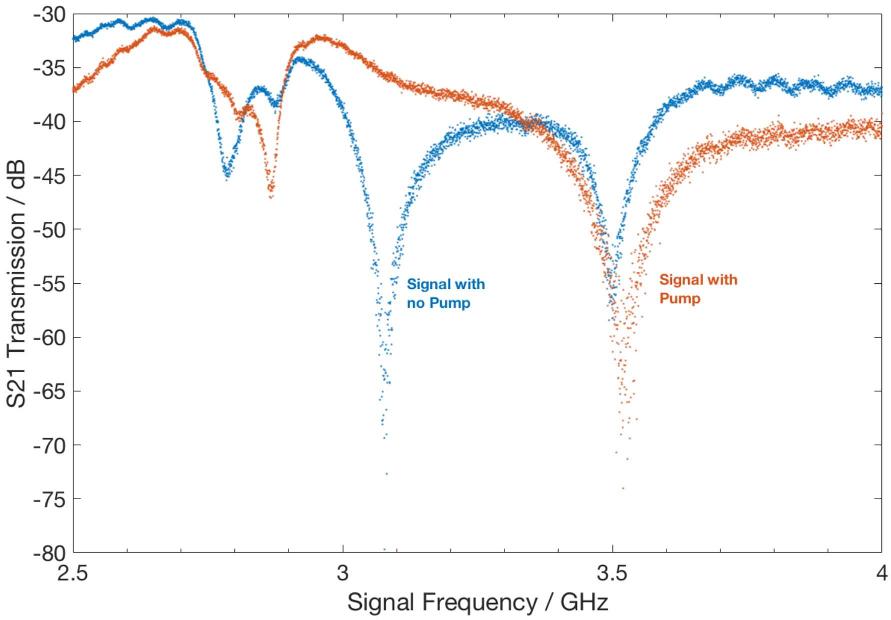

Figure 5.20: S21 transmission at signal frequencies from 2.5 to 4GHz with no pump (blue) and with a -20dBm 2GHz pump tone (orange). The presence of a pump appears to stimulate amplification of the signal being transmitted through the Tl2212 transmission line.

in Figure 5.20. There is a peak gain of 30dB and a short bandwidth of only 10MHz, extracted from the least square lorentzian fit shown in red, which although seems to be a positive result, it is however over a small bandwidth. When comparing the gain results to those presented by O'Brien *et al.* [96], Eom *et al.* [84] and White *et al.* [95], they show peak gains of up to 20dB over a broad bandwidth of up to 6GHz, which is in stark contrast to the results shown in Figure 5.21. The gain profiles presented by these groups also are independant of any S21 resonances, which again appears not to be the case with the data measured from this device.

In order to further investigate the relationship between the pump tone and the gain at the 3.077GHz resonant feature, the dependence of the gain on the pump frequency was measured. Figure 5.22 shows the peak signal gain at 3.077GHz (extracted from the lorentzian fit as shown in Figure 5.21) as a function of the pump tone frequency at -20dBm, being swept between 1 and 4GHz. From the data, the peak gain at the 3.077GHz resonant peak prodominatly shows independance to the pump frequency. This

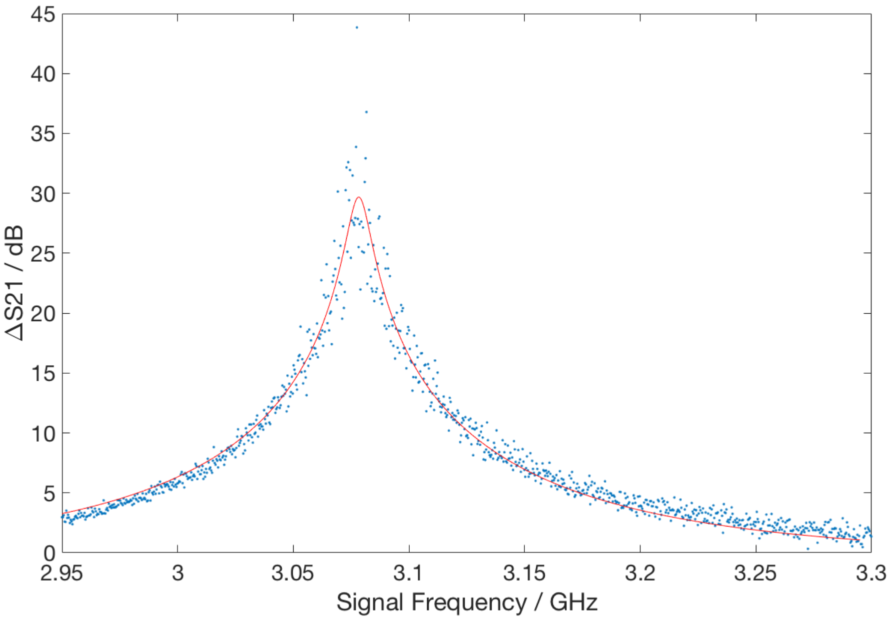

Figure 5.21: ΔS21 at signal frequencies where gain is observed, between 2.95 and 3.3GHz. The data is obtained by subtracting the measurement with no pump from the data with the pump tone. The red line shows a least square lorentzian fit to the data to better extract the peak gain, bandwidth and central frequency.

result is not consistent with FWM, whereby the gain profile is centred around the pump frequency, as shown by the O'Brien, Eom and White groups [84, 95, 96]. This result is further evidence that the origin of the gain is not parametric amplification.

Although being pump frequency independent and appearing not to be caused by parametric amplification, the gain profile shown in Figure 5.21 has a dependence on the pump power. Figure 5.23 shows the pump power dependence of the signal gain at the 3.077GHz resonant feature.

We can see as the pump tone power increases above -50dBm, there is an increase in the gain at 3.077GHz up to approximately 30dB at the peak. As the pump power increases, the expectation was that the AC pump signal would increase in amplitude until exceeding I_{sw}, at which point the superconductivity of the coplanar track would break down, and there would be a reduction in gain. This was not seen in the results up to pump powers of -5dBm, which translates to input powers of 0.3mW. At 50Ω line impedance, this converts to a pump current of 2.5mA. Considering the track switching current was

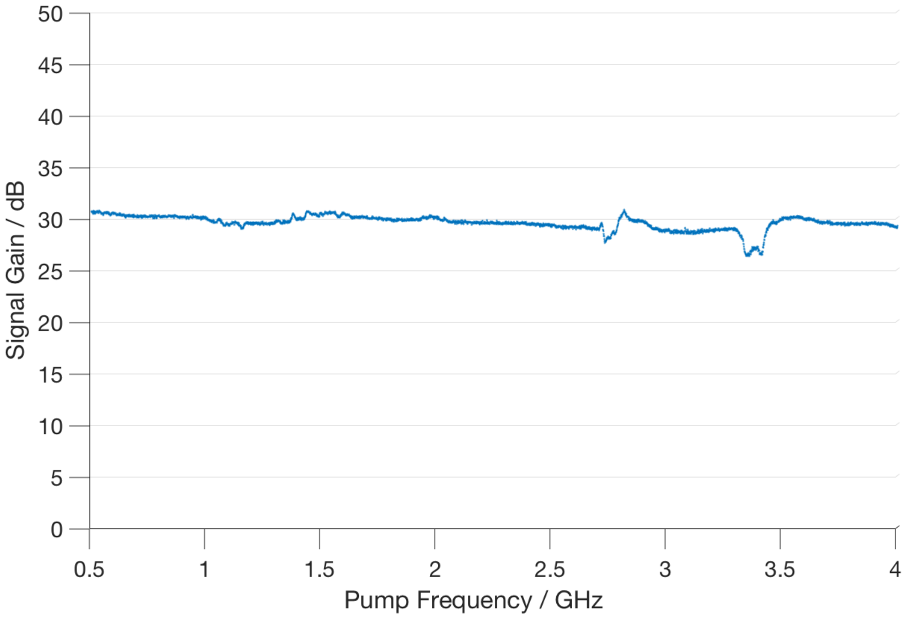

FIGURE 5.22: Pump tone frequency dependence of the signal gain at 3.077GHz, measured at 4.2K.

approximately 2.1μA, the expectation was that a pump power of this magnitude would have sent the track normal and destroyed the superconductivity. Figure 5.11 in Section 5.4 shows that as the rf power of the transmitted signal increased from -60dBm to -30dBm, we see a loss of superconductivity and a return to the normal state of linear resistive characteristics. This would indicate that as the pump power is increased above -50dBm, the IJJ transmission line is being driven normal due to rf heating and the signal gain cannot be attributed to superconducting behaviour, or degenerative FWM as described by Eom and White.

To better understand the behaviour of the S21 transmission, the temperature dependence was measured to try and ascertain whether the resonant peaks around 3.1GHz were related to the superconductivity of the material. Figure 5.24 shows the comparison between the 3.1GHz resonant feature at 4.2K (blue), and the S21 transmission at the same frequency at 115K (red), above the T$_c$ of the Tl2212, with no pumping. Plotted on the same graph is the S21 transmission with a 0dBm 2.5GHz pump tone (green). The shift in the resonant frequency from 3.077GHz to 3.103GHz was a consequence

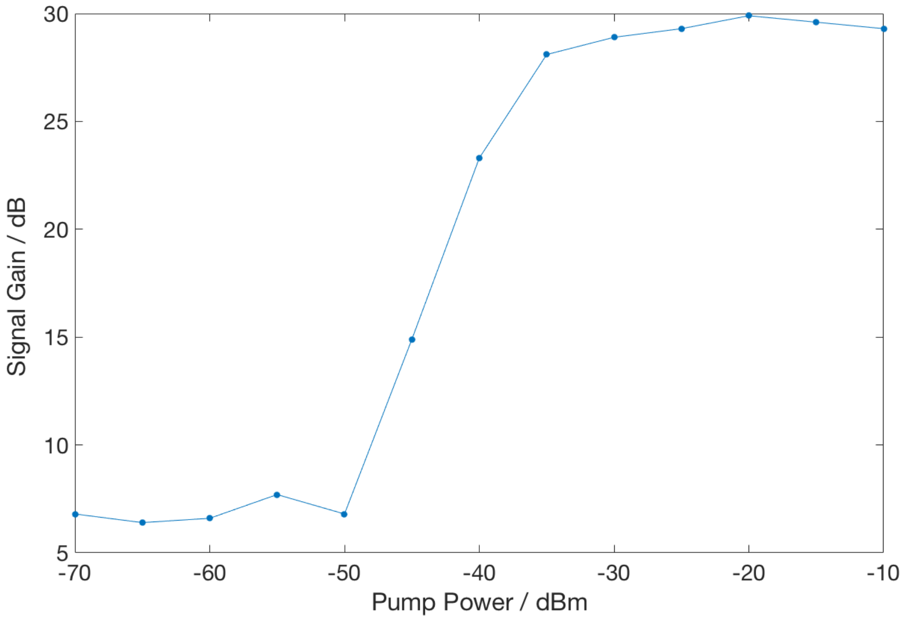

FIGURE 5.23: Pump power dependence of the signal gain at 3.077GHz, measured at 4.2K.

of measuring the device a month apart from the previous measurements. We see that as the temperature of the sample is increased with no pumping, there is a reduction in the S21 transmission loss, going from -62dB at the resonant dip at 4.2K to -34dB at the same frequency above the T$_c$ of the Tl2212. When we compare the pumped transmission line data in green to the non pumped, both measured at 4.2K, we also see the same reduction of loss in S21 transmission. It is clear from the comparison of this data shown in Figure 5.24 that the apparent pumped gain seen in the low temperature measurements was actually the suppression of the material superconductivity, by which the S21 transmission returns to the lower loss normal state of the material above the T$_c$, through heating, or J$_c$, through a large signal current. The pumped transmission line results confirm this hypothesis as the S21 transmission tends towards the behaviour of the material in the normal state above the transition temperature.

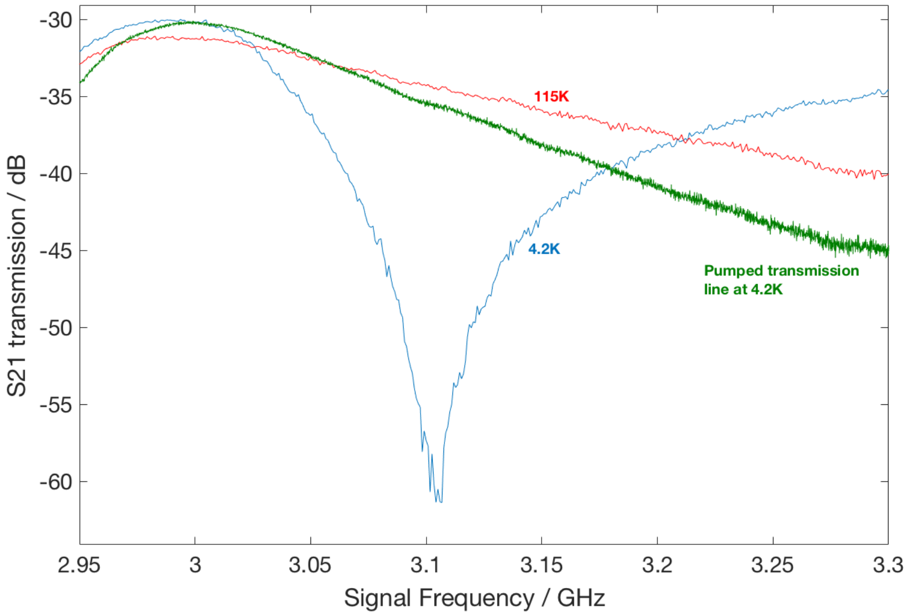

FIGURE 5.24: Comparison between S21 transmission at 4.2K (blue), 115K (red) and the pumped transmission line at 4.2K (green) in the region of the resonance at 3.1GHz. The pump power and frequency were 0dBm and 2.5GHz.

Chapter 6

Conclusions

The work presented in this thesis was performed to investigate the use of IJJs as a superconducting phase shifter, with potential for further use as a parametric amplifier.

IJJ tracks were fabricated in vicinal Tl2212 HTS films to highlight the ease of design and fabrication in comparison to other techniques used to bias and produce phase shifting devices. These tracks were then measured at low temperature and the dependence of the IV characteristics on the width of the tracks was found to show that smaller track widths provided better Josephson characteristics and suffered from less flux flow behaviour.

Once optimal track widths were established, the RF transmission behaviour of these tracks were measured. The bias current dependence of the phase followed the same trend identified by the IV measurements, with the smaller track width of 10μm showing a quadtratic relationship between the phase and current. The phase relationship was in very good agreement with the simulated results based on the equations derived from the fundamental Josephson equations in conjunction with transmission line theory. This shows with simple design and fabrication techniques that IJJs have the potential to produce large amounts of phase shift whilst only requiring a small amount of space; a premium in cryogenic systems. Comparisons were drawn between this research and other existing designs which found that the phase shift of 20 degrees per mm was orders of magnitude larger and required significantly less input power than recent work using different fabrication techniques. This is thought to be due to the beneficial high density atomic layering found within cuprate HTSs. Future work in this research field should focus on investigating larger lengths of IJJ tracks to utilise greater numbers of junctions to produce greater phase shift. It is thought that smaller track widths will not provide significantly more phase shift, but may improve the Josephson behaviour of the HTS. Moving from straight tracks to meandering designs should allow for more efficient use of space without compromising the beneficial phase tunability, and also help eliminate detrimental resonant features in the transmission characteristics.

Following the tunable phase measurements, it was thought that the large phase shift could be utilised in a travelling wave parametric amplifier. Measurements were performed to investigate any possible amplification created by the IJJ tracks due to a parametric effect caused by the non-linear kinetic inductance. The results from these pumping measurements found that there was a region of gain in the S21 transmission characteristics that was coupled to a resonant feature thought to be caused by a standing wave mode in the length of the IJJ track. The gain that was seen during the pumping experiments was independent of pump frequency, in contradiction with the principles of parametric amplification. The gain did however have a dependence on the pump tone power, which unusually appeared not to reduce the gain as expected as a result of switching the superconductor into the normal state. When investigating the temperature dependence of the resonant feature, it became apparent that the resonance appeared only below the T_c of the superconductor, and the normal state of the superconductor showed less insertion loss than when superconducting.

Further research is required to identify the necessary device design to optimise behaviour of the IJJ track for use as a parametric amplifier, however the postive phase tunability shows potential for this application in the future. Integrating resonant phase matching into the design, alongside increasing the phase shift by lengthening the track should both help progress the research towards this goal.

References

1. Josephson, B. Non-linear conduction in superconductors. *Physics Letters* **1,** 251–253 (1962).
2. Field, B. F., Finnegan, T. F. & Toots, J. Volt Maintenance at NBS via 2e/h: A New Definition of the NBS Volt. *Metrologia* **9,** 155–166 (1973).
3. Jaklevic, R. C., Lambe, J., Silver, A. H. & Mercereau, J. E. Quantum Interference Effects in Josephson Tunneling. *Physical Review Letters* **12,** 159 (1964).
4. Kleiner, R., Steinmeyer, F., Kunkel, G. & Muller, P. Intrinsic Josephson Effects in $Bi_2Sr_2CaCu_2O_8$ Single Crystals. *Physical Review Letters* **68,** 2394–2397 (1992).
5. Tinkham, M. *Introduction to Superconductivity* Second Edition. ISBN: 0070648786 (McGraw-Hill, Inc., 1996).
6. Poole, C. P., Farach, H. A., Creswick, R. J. & Prozorov, R. *Superconductivity* ISBN: 9780120887613 (Academic Press, 2007).
7. Waldram, J. R. *Superconductivity of Metals and Cuprates* ISBN: 0852743351 (Institute of Physics Publishing, 1996).
8. Sheahen, T. P. *Introduction to High-Temperature Superconductivity* ISBN: 0306447932 (Kluwer Academic Publishers, 2002).

9. H. K. Onnes. Further experiments with liquid helium D - On the change of the electrical resistance of pure metals at very low temperatures, etc The disappearance of the resistance of mercury. *Proceedings of the Koninklijke Akademie Van Wetenschappen Te Amsterdam* **14,** 113–115 (1911).
10. Bardeen, J., Cooper, L. & Schrieffer, J. R. Microscopic Theory of Superconductivity. *Physical Review* **106,** 162 (1957).
11. Pippard, A. B. An experimental and theoretical study of the relation between magnetic field and current in a superconductor. *Procedures of the Royal Society London* **A216,** 547 (1953).
12. Bardeen, J., Cooper, L. & Schrieffer, J. R. Theory of Superconductivity. *Physical Review* **108,** 1175–1204 (1957).
13. Cooper, L. N. Bound Electron Pairs in a Degenerate Fermi Gas. *Phys. Rev.* **104,** 1189 (1956).
14. Meissner, W. & Ochsenfeld, R. Ein neuer Effekt bei Eintritt der Supraleitfahigkeit. *Naturwissenschaften* **21,** 787–788 (1933).
15. Schilling, A., Cantoni, M., Guo, J. D. & Ott, H. R. Superconductivity above 130 K in the Hg-Ba-Ca-Cu-O system. *Nature* **363,** 56–58 (1993).
16. Kirtley, J. R. *et al.* Symmetry of the order parameter in the high-Tc superconductor $YBa_2Cu_3O_7 - delta$. *Nature* **373,** 225–228 (1995).
17. Anderson, P. W. & Rowell, J. M. Probable Observation of the Josephson Superconducting Tunneling Effect. *Physical Review Letters* **10,** 203 (1963).
18. Saleem, S. *Dynamical behaviour of Intrinsic Josephson junctions* Ph.D Thesis (2009). ISBN: 3848431254.
19. Chana, O. *Intrinsic Josephson effects in Superconducting thin films* Ph.D Thesis (King's College London, 2001).

20. Barone, A. & Pagano, S. Weakly coupled high Tc superconductors - An overview. *Journal of Superconductivity* **7,** 375–380 (1994).

21. Dimos, D., Chaudhari, P., Mannhart, J. & LeGoues, F. K. Orientation Dependence of Grain-Boundary Critical Currents in YBCO Bicrystals. *Physical Review Letters* **61,** 219 (1988).

22. Daly, K. P. *et al.* Substrate step edge $YBa_2Cu_3O_7$ rf SQUIDs. *Applied Physics Letters* **58,** 543 (1991).

23. Gao, J. *et al.* Characteristics of advanced $YBa_2Cu_3O_x/PrBa_2Cu_3O_x/YBa_2Cu_3O_x$ edge type junctions. *Applied Physics Letters* **59,** 2754 (1991).

24. Siegel, M. *et al.* Fabrication and Properties of High-Tc YBCO Josephson Junction and SQUID With Variable Thickness Bridges by Focused Ion Beam. *IEEE Transactions on Applied Superconductivity* **21,** 375–378 (2011).

25. Wu, C.-H. *et al.* Investigation of YBCO step-edge Josephson junctions. *IEEE Transactions on Applied Superconductivity* **3,** 2369–2372 (1993).

26. Lee, K. Josephson effects in $\mathrm{YBa_2Cu_3O}_y$ grain boundary junctions on (100)MgO bicrystal substrates. *Applied Physics Letters* **66,** 769 (1998).

27. Holstein, W. L., Parisi, L. A., Wiiker, C. & Flippen, R. B. $\mathrm{TI_2Ba_2CaCu_2O_8}$ films with very low microwave surface resistance up to 95 K. *Applied Physics Letters* **60,** 2014 (1992).

28. Subramanian, M. A. *et al.* Crystal structure of the high-temperature superconductor $\mathrm{TI_2Ba_2CaCu_2O_8}$. *Nature* **332,** 420–422 (1988).

29. Kang, J. H., Gray, K. E., Kampwirth, R. T. & Day, D. W. Large anisotropy in the upper critical field of sputtered thin films of superconducting Tl-Ba-Ca-Cu-O. *Applied Physics Letters* **53,** 2560 (1988).

30. Paranthaman, M., Duan, H. & Hermann, A. *Thallium-Based High-Temperature Superconductors* ISBN: 9780824791148 (CRC Press, 1993).

31. Johansson, L. G. *et al.* Preparation and properties of $TI_2Ba_2CaCu_2O_8$ thin films. *Journal of Superconductivity* **7,** 767–771 (1994).

32. Westerheim, A. C., Anderson, A. C. & Oates, D. E. Relation between electrical properties and microstructure of $YBa_2Cu_3O_{7-x}$ thin films deposited by single target off axis sputtering. *Journal of Applied Physics* **75,** 393 (1994).

33. A.Rahman, Rahaman, Z. & Samsuddoha, N. A Review on Cuprate Based Superconducting Materials Including Characteristics and Applications. *American Journal of Applied Physics and Applications* **3,** 39–56 (2015).

34. Varshney, D., Singh, R. K. & Shah, S. Coherence Lengths and Magnetic Penetration Depths in $YBa_2Cu_30_7$ and $YBa_2Cu_40_8$ Superconductors. *Journal of Superconductivity* **9,** 6 (1996).

35. Cronemeyer, D. C. *et al.* On the anisotropy of critical current density in YBaCuO crystals. *Proceedings of the ICTPS '90 International Conference on Transport Properties of Superconductors,* 11 (1990).

36. Wang, Z. H. *et al.* Self-emission from intrinsic Josephson junction arrays in misaligned $Tl_2Ba_2CaCu_2O_{8+\delta}$ thin films at 78 K. *Superconductor Science and Technology* **24,** 075008 (2011).

37. Chana, O. S. *et al.* Josephson effects in misaligned Tl-2212 films. *Physica C* **326-327,** 104–110 (1999).

38. Wang, P. *et al.* Radiation from Intrinsic Josephson Junctions in Misaligned $Tl_2Ba_2CaCu_2O_8$ Thin Films. *Journal of Superconductivity and Novel Magnetism* **25,** 1427–1430 (2012).

39. Grib, A. *et al.* The Resonant Interaction of Intrinsic Josephson Junctions With Standing Waves. *IEEE Transactions on Applied Superconductivity* **24,** 1800205 (2014).

40. Gross, R. *et al.* Physics and Technology of High Temperature Superconducting Josephson Junctions. *IEEE Transactions on Applied Superconductivity* **7,** 2929–2935 (1997).

41. Cirillo, M. & Lloyd, F. L. Phase lock of a long Josephson junction to an external microwave source. *Journal of Applied Physics* **61,** 2581 (1987).

42. Palmer, D. W. & Mercereau, J. E. Coherent effects in large arrays of superconducting bridges. *Applied Physics Letters* **25,** 467 (1974).

43. Galin, M. A. *et al.* Synchronization of Large Josephson-Junction Arrays by Traveling Electromagnetic Waves. *Physical Review Applied* **9,** 054032 (2018).

44. Barbara, P., Cawthorne, A. B., Shitov, S. V. & Lobb, C. J. Stimulated Emission and Amplification in Josephson Junction Arrays. *Physical Review Letters* **82,** 1963–1966 (1999).

45. Benz, S. P. & Booi, P. A. A. High-Frequency Oscillators Using Phase-Locked Arrays of Josephson Junctions. *IEEE Transactions on Ultrasonics, Ferroelectrics and Frequency Control* **42,** 964–966 (1995).

46. Holst, T., Hansen, J. B., Grunbech-Jensen, N. & Blackburn, J. A. Phase-locked Josephson soliton oscillators. *IEEE Transactions on Magnetics* **27,** 2704–2707 (1991).

47. Gray, K. *et al.* Emission of Terahertz Waves from Stacks ofIntrinsic Josephson Junctions. *IEEE Transactions on Applied Superconductivity* **19,** 886–890 (2009).

48. Cirillo, M., Rotoli, G., Mueller, F., Niemeyer, J. & Poepel, R. Phase-locking Josephson junctions arrays. *Journal of Applied Physics* **90,** 3570 (2001).

49. Benz, S. P. & Burroughs, C. J. Two-dimensional arrays of Josephson junctions as voltage-tunable oscillators. *Superconductor Science and Technology* **4,** 561–567 (1991).

50. Popel, R. The Josephson Effect and Voltage Standards. *Metrologia* **29,** 153–174 (1992).

51. Harbaugh, J. K. & Stroud, D. Model for a Josephson junction array coupled to a resonant cavity. *Physical Review B* **61,** 14765 (2000).

52. Krasnov, V. M. Coherent flux-flow emission from stacked Josephson junctions: Nonlocal radiative boundary conditions and the role of geometrical resonances. *Physical Review B* **82,** 134524 (2010).

53. Ozyuzer, L. *et al.* Terahertz wave emission from intrinsic Josephson junctions in high-Tc superconductors. *Superconductor Science and Technology* **22,** 114009 (2009).

54. Holst, T., Hansen, J. B., Grшnbech-Jensen, N. & Blackburn, J. A. Microwave Wideband Tunable Oscillators using Coherent Arrays of Josephson Junctions. *IEEE Transactions on Magnetics* **Mag-17,** 99–102 (1981).

55. Jain, A. K., Likharev, K. K., Lukens, J. E. & Sauvageau, J. E. Mutual Phase-Locking in Josephson Junction Arrays. *Physics Reports* **109,** 309–426 (1984).

56. Kurin, V. V., Vdovicheva, N. K. & Shereshevskii, I. A. Josephson Travelling Wave Antennas. *Radiophysics and Quantum Electronics* **59,** 922–936 (2017).

57. Jain, A. K., Likharev, K. K., Lukens, J. E. & Sauvageau, J. E. Low-frequency behaviour of coupled Josephson junctions near phase locking. *Applied Physics Letters* **41,** 566 (1982).

58. Weber, M., Cho, J., Flavin, J., Herd, J. & Vai, M. Multi-function Phased Array Radar for U.S. Civil-Sector Surveillance Needs. *Federal Aviation Administration Air Force Contract Report.* `https://ams.confex.com/ams/pdfpapers/96905.pdf`.

59. Stark, L. Microwave Theory of Phased-Array Antennas - A Review. *Proceedings of the IEEE* **62,** 1661–1701 (1974).

60. Sun, P. *et al.* X-band 5-bit MMIC phase shifter with GaN HEMT technology. *Solid-State Electronics* **136,** 18–23 (2017).

61. Hiyashi, H. & Muraguchi, M. An MMIC Active Phase Shifter Using a Variable Resonant Circuit. *IEEE Transactions on Microwave Theory and Techniques* **47,** 2021–2026 (1999).

62. Wang, M. *et al.* A 6-bit 38 GHz SiGe BiCMOS phase shifter for 5G phased array communications. *IEICE Electronics Express* **14,** 1–10 (2017).

63. Zheng, Q. *et al.* Design and Performance of a Wideband Ka-Band 5-b MMIC Phase Shifter. *IEEE Microwave and Wireless Components Letters* **27,** 482–484 (2017).

64. Poon, A. & Taghivand, M. Supporting and Enabling Circuits for Antenna Arrays in Wireless Communications. *Proceedings of the IEEE* **100,** 2207–2218 (2012).

65. Nagra, A. & York, R. Distributed Analog Phase Shifters with Low Insertion Loss. *IEEE Transactions on Microwave Theory and Techniques* **47,** 1705–1711 (1999).

66. Ellinger, F., Jackel, H. & Bachtold, W. Varactor-Loaded Transmission-Line Phase Shifter at C-Band Using Lumped Elements. *IEEE Transactions on Microwave Theory and Techniques* **51,** 1135–1140 (2003).

67. Upshur, J. & Geller, B. Low-loss 360 degree X-Band Analog Phase Shifter. *IEEE Microwave Symposium Digest,* 487–490 (1990).

68. Henoch, B. & Tamm, P. A 360 degree Reflection-Type Diode Phase Modulator. *IEEE Transactions on Microwave Theory and Techniques* **Correspondence,** 103–105 (1971).

69. Ellinger, F., Vogt, R. & Bachtold, W. Ultracompact Reflective-Type Phase Shifter MMIC at C-Band With 360 degree Phase-Control Range for Smart Antenna Combining. *IEEE Journal of Solid-State Circuits* **37,** 481–486 (2002).

70. Grajal, J., Gismero, J., Mahfoudi, M. & Petz, F. A 1.4/2.7-GHz Analog MMIC Vector Modulator for a Crossbar Beamforming Network. *IEEE Transactions on Microwave Theory and Techniques* **45,** 1705–1714 (1997).

71. Ellinger, F., Vogt, R. & Bachtold, W. Calibratable Adaptive Antenna Combiner at 5.2 GHz with High Yield for Laptop Interface Card. *IEEE Transactions on Microwave Theory and Techniques* **48,** 2714–2720 (2000).

72. Dionne, G., Oates, D. & Temme, D. Low-Loss Microwave Ferrite Phase Shifters with Superconducting Circuits. *IEEE Microwave Symposium Digest,* 101–103 (1994).

73. Balashov, D. *et al.* Passive Phase Shifter for Superconducting Josephson Circuits. *IEEE Transactions on Applied Superconductivity* **17,** 142–145 (2007).

74. Bordier, G. *et al.* Superconducting Coplanar Switch and Phase Shifter for CMB Applications. *Journal of Low Temperature Physics* **185,** 547–552 (2016).

75. Yeo, K. & Lancaster, M. High Temperature Superconducting Ferrite Phase Shifter with New Latching Structure. *IEEE Transactions on Applied Superconductivity* **185,** 430–433 (2001).

76. Kwak, M. *et al.* Microwave Properties of Tunable Phase Shifter Using Superconductor/Ferroelectric Thin Films. *Integrated Ferroelectrics* **77,** 79–85 (2005).

77. Keuls, F. W. V. *et al.* $YBa_2Cu_3O_7, Au/SrTiO_3/LaAlO_3$ thin film conductor/ferroelectric coupled microstripline phase shifters for phased array applications. *Applied Physics Lettters* **71,** 3075–3077 (1997).

78. Cai, S. Z. & Chen, D. Y. High-Tc Superconducting Microwave Phase Shifter. *International Journal of Infrared and Millimeter Waves* **15,** 439–449 (1994).

79. Jackson, C., Kobayashi, J., Guillory, E., Pettiette-Hall, C. & Burch, J. Monolithic HTS Microwave Phase Shifter and Other Devices. *Journal of Superconductivity* **5,** 417–422 (1992).

80. Takemoto-Kobayashi, J., Jackson, C., Guillory, E., Pettiette-Hall, C. & Burch, J. Monolithic High-Tc Superconducting Phase Shifter at 10 GHz. *IEEE Transactions on Microwave Theory and Techniques* **40,** 2339–2344 (1992).

81. Durand, D. *et al.* The Distributed Josephson Inductance Phase Shifter. *IEEE Transactions on Applied Superconductivity* **2,** 33–38 (1992).

82. Perold, W. J. The Effect of Mutual Coupling Between RF Squid's in Distributed Josephson Inductance Phase Shifters. *IEEE Transactions on Applied Superconductivity* **4,** 179–181 (1994).

83. Kokkoniemi, R. *et al.* Flux-tunable phase shifter for microwaves. *Nature Scientific Reports* **7,** 1–6 (2017).

84. Eom, B., Day, P., LeDuc, H. & Zmuidzinas, J. A wideband, low-noise superconducting amplifier with high dynamic range. *Nature Physics* **8,** 632–627 (2012).

85. Zhang, L., Peng, W., You, L. X. & Wang, Z. Superconducting properties and chemical composition of NbTiN thin films with different thickness. *Applied Physics Letters* **107,** 122603 (2015).

86. Speller, S. C. Thallium based high temperature superconductors for microwave device applications. *Materials Science and Technology* **19,** 269–282 (2003).

87. Kang, J. H., Kampwirth, R. T. & Gray, K. E. Superconducting properties of magnetron sputtered high Tc thin films containing oxide compounds of yttrium, bismuth, or thallium. *IEEE Transactions on Magnetics* **25,** 2226–2229 (2 1989).

88. Grib, A., Shukrinov, Y., Schmidl, F. & Seidel, P. Experimental and theoretical investigation on high-Tc superconducting intrinsic Josephson junctions. *Journal Of Physics:Conference Series - International Conference on Theoretical Physics* **248,** 1–8 (2010).

89. Zhang, G. *et al.* The study of c-axis IV characteristics of Tl2212 thin film. *Physica C* **388-389,** 755–756 (2003).

90. Zhou, T. G. *et al.* IV Characteristic and Josephson inductance of ultra-long intrinsic Josephson junction arrays. *Physica C* **444,** 81–85 (2006).

91. Miyahara, K., Kubo, S. & Suzuki, M. Vortex flow characteristics of high-Tc flux flow transistors. *Journal of Applied Physics* **75,** 404–407 (1994).

92. Gaifullin, M. B., Latyshev, Y., Yamashita, T. & Matsuda, Y. Shapiro step response in $Bi_2Sr_2CaCu_2O_{8-d}$ in parallel and tilted magnetic field. *Physica C* **392-396,** 319–322 (2003).

93. Armstrong, J. A., Bloembergen, N., Ducuing, J. & Pershan, P. S. Interactions between Light Waves in a Nonlinear Dielectric. *Physical Review* **127,** 1918–1939 (1962).

94. Cullen, A. L. A Travelling-Wave Parametric Amplifier. *Nature* **181,** 332 (1958).

95. White, T. C. *et al.* Traveling wave parametric amplifier with Josephson junctions using minimal resonator phase matching. *Applied Physics Letters* **106** (2015).

96. O'Brien, K., Macklin, C., Siddiqi, I. & Zhang, X. Resonantly phase-matched Josephson junction traveling wave parametric amplifier. *Physical Review Letters* **113** (2014).